Acoustic Manipulation of Macroscopic Objects

Mohamed Abdalla Ghanem

A dissertation

submitted in partial fulfillment of the

requirements for the degree of

Doctor of Philosophy

University of Washington

2018

Reading Committee:

Michael R. Bailey, Ph.D., Chair

Adam D. Maxwell, Ph.D.

Oleg A. Sapozhnikov, D.Sc.

Program Authorized to Offer Degree:

Aeronautics and Astronautics

University of Washington

Abstract

Acoustic Manipulation of Macroscopic Objects

Mohamed Abdalla Ghanem

Chair of the Supervisory Committee:
Michael R Bailey
Department of Mechanical Engineering

Acoustic waves can apply radiation forces to trap and levitate objects. Most recently, three-dimensional acoustic traps have been created using single-sided multi-element arrays. Almost all the work accomplished in this field is concerned with the trapping of light objects in air or microscopic objects in liquids. The purpose of this work is to investigate acoustic manipulation of macroscopic objects such as kidney stones specifically for non-invasive medical treatments. Toward this end, a 1.5 MHz 256-element focused ultrasound array was used. A characterization of the array output was performed to equalize the complex vibrational output of each element and produce uniform vortex beams. Vortex beams were generated and compared to simulation of the fields from an idealized array. Measurements show improvement of beam symmetry up to 9%. The lateral trapping strength of different acoustic beams was measured to examine their

ability to trap and manipulate large dense objects. This was the first effort to quantify the lateral forces on large objects and compare them to theoretical predictions. Vortex beams and two other beam shapes having a toroidal pressure field in the focal plane were used to measure the lateral trapping strength. Spherical targets of various sizes were placed in the acoustic traps and held in the focal plane of the array by a frame mounted to the array. The array-frame setup was rotated until the bead fell out of the acoustic trap. Good agreement between measurements and theory was achieved. Lateral acoustic trapping and steering of large targets was demonstrated along two-dimensional path against a flat surface in water. Three-dimensional traps with the aid of gravitational pull were synthesized and millimeter-sized glass spheres were levitated and manipulated in water above a tissue mimicking phantom. The stability of the acoustic off-axis steered traps was shown to be most stable for a ratio of bead to beam width less than unity. Finally, a 3-mm spherical glass bead, a kidney stone mimicking target, was successfully manipulated and steered in three-dimensional path inside a live pig with ultrasound imaging.

TABLE OF CONTENTS

LIST OF FIGURES

LIST OF TABLES

ACKNOWLEDGEMENTS

I would like to thank my advisors Prof. Michael R Bailey, Prof. Adam Maxwell and Prof. Oleg Sapozhnikov and my committee members Prof. Jim Hermanson and Prof. Anthony Waas for giving me support and guidance, and being extremely generous with their time. I also appreciate Prof. Vera Khokhlova for her contribution in guiding the research, Dr. Wayne Kreider and Bryan Cunitz for assisting in experimental setup, and Akshay Randad, Brian MacConaghy, Chris Hunter and Barbrina Dunmire for their assistance. I thank all my colleagues at the Center for Industrial and Medical Ultrasound (CIMU). I am grateful that I have had many mentors, teachers or coaches in my life who have contributed to my academic and personal growth.

Lastly, I am grateful for the love and support of my family and fiancée.

DEDICATION

This work is dedicated to my mother.

Ch 1:INTRODUCTION

A sound wave can apply radiation pressure [1]–[3] on objects. The radiation pressure results in radiation forces that are a result of the change of the momentum flux around an object. An object placed in an acoustic field will cause the incident wave to be scattered. The incident and scattered acoustic field around the object change the momentum flux due to changes in the direction of the wave resulting in acoustic radiation force. The acoustic radiation force resulting from plane waves [1], [3], [4] and spherical waves [5]–[7] on spherical objects [8] has been well studied. The resulting radiation forces have been used to form acoustic traps to surround and control objects in air [9], [10] and water [11]. In most trapping applications, the acoustic sources used for trapping surrounded the object from more than one side. A common setup includes single-axis trapping [12]–[14] in which the positioning of a single sound source with a reflector opposite to it to creates a standing wave, so a particle placed in the location of zero pressure or pressure nodes of such field and surrounded by high pressure amplitude will be trapped. The location of the particles could be changed along the propagation axis of the source by changing the wavelength which changes the location of the pressure nodes. More sophisticated traps are created using a multi-element array flat source with a reflector to move particles in-plane by introducing phasing between the different array elements to change the location of the trapping pressure node [9], [15]. Multi-element array flat array is a sound source that consists of multiple smaller sources that can be triggered with a time delay between them (phasing) to create specific pressure distributions. A more complex three-dimensional trap was created by surrounding the object with a multi-element array flat sources from more than one side [16], where the elements are directed to different spatial locations to move the pressure nodes in three dimensions.

Single-sided trapping, which uses a sound source from one side only without a reflector, has been accomplished [10], [11], [17], [18] through the use of multi-element arrays. The phasing of the transducers in an array is varied to create different beam shapes traps, such as, vortex [11], [19], [20] and bottle traps [10], [21], which are explained in detail in chapter two and three. These acoustic traps have areas of null pressure similar to the pressure nodes of standing waves where the particle is surrounded by a high-pressure field and trapped in the null pressure regions. Most of the single-sided acoustic traps accomplished are for Rayleigh particles (i.e. diameter is much smaller than the wavelength) where the scattering monopole and dipole terms are the dominant terms of the scattered field and the resulting force [22]. For small particles the forces are convergent on the particle, since it is smaller than the wavelength the particle is trapped in a potential well created by surrounding pressure wavefronts and the forces are calculated as the gradient of the potential of the field [22]. However; particles larger than the wavelength are not mainly affected by the gradient forces between the wavefronts, and the higher order scattering multipole terms [23], [24] are necessary to resolve the scattered field from which the radiation forces are resolved. Most recently the trapping of large light objects has been accomplished. In air, a large polystyrene sphere was trapped using three transducers to levitate the sphere in the standing wave created between the sources and the sphere itself [25]. Multi-element arrays were used to trap in pressure nulls of vortex beams light polystyrene spheres on the order of the wavelength in air [26]. Alternatively, the negative acoustic radiation forces was measured on a triangular shaped hollow prism in water [27]. The triangular shaped prism had sides much larger than the wavelength that act as flat reflective surfaces resulting in forward scattering (away from the source), so that for the conservation of the momentum flux around the prism to hold radiation forces are produced toward the source. However, no work has been done toward the goal of manipulating large dense

objects in water. As previously mentioned, the acoustic forces are not convergent on large objects which makes it more difficult to have stable trapping. Also, non-uniformity of trapping beams on large objects can result in ejection of the target. Thus, toward this goal, I use a focused multi-element array that has been characterized to produce uniform two-dimensional beam shapes and can produce high pressure in a confined focal region where large dense objects are stably trapped and manipulated in three-dimensional space *in vitro* and *in vivo*.

Here, the work presented is toward the development of acoustic tweezers to trap and manipulate large dense objects in water generally, and for non-invasive kidney stone management specifically. For lack of a better term we use the term acoustic tweezers. Others have used the term "tractor beams," but unlike other tweezers, here, we use a single source to trap and manipulate large dense objects in 3D space (in water) by electronically steering our acoustic beam. Ultrasound offers a viable option for non-invasive kidney stone treatments[28]–[30]. Recently, ultrasonic propulsion has been successfully used to expel small passable kidney stones [31]–[33]. The development of acoustic tweezers will further enable the controlled manipulation and non-invasive management of kidney stones. Kidney stones are generally larger than the wavelength of therapeutic ultrasound. As previously mentioned, large objects require the synthesis of designed beam shapes with null pressure regions to create acoustic traps. In this work a highly focused multi-element array was used to produce high acoustic field intensity of trapping beam shapes in specific spatial regions in order to create acoustic traps for large dense objects and acoustically manipulate them in water. Water is an ideal medium since it has similar acoustic properties to biological tissue, in which the acoustic manipulation was tested, and can support higher amplitude pressure waves than air as required for dense particles. In this work, acoustic traps produced by a single sound source (acoustic tweezers) were used to successfully trap and manipulate a kidney

stone mimicking target along a specified path inside the bladder of a live pig with ultrasound imaging. The acoustic manipulation of macroscopic objects presented here lays the groundwork for a multitude of applications of the acoustic tweezers. Such technology can be used for non-invasive medical treatment of blood clots, removal of foreign objects or targeted drug delivery. Other applications include manufacturing, containerless transport, and contactless biological and chemical experiments.

This dissertation presents the research performed to achieve the acoustic manipulation of macroscopic objects specifically in water. The research is explained over three chapters that start from describing the acoustic source; then, calculating and measuring the acoustic radiation force; finally, the three-dimensional manipulation of macroscopic objects *in vitro* and *in vivo*. Chapter two describes the details of the single-sided acoustic ultrasound source which consists of 256-element array. In chapter two a complete, electrical and acoustic, characterization of the array was carried out enabling the equalization of the complex velocity vibration of all array elements resulting in uniform two-dimensional beam shapes used in the manipulation of various targets. Furthermore, the characterization of the complex velocity vibration profile was localized to each element and used in the synthesis of any desired beam shape and the simulation of the acoustic field produced by the array and used in the simulation of consequent work.

Consequently, chapter three quantifies the lateral strength of the acoustic radiation force and compares it with the theoretical model. The investigated beams were synthesized using the array characterization of chapter two. The measurements of the trapping strength of the acoustic beams were compared with the acoustic radiation force theoretical model of Ref [34], which calculates the force on an elastic sphere of any size in an arbitrary location of the acoustic field. The measurement of the various synthesized beams, such as, vortex beams and two radially-varying

phase beams was performed and compared to theory. Important results of chapter three were the good agreement between measurements and theoretical model of the radiation forces and relation between the ratio of the target to the beam size to the trapping force, which laid the ground work for the stable levitation and manipulation of objects in three-dimensional space.

In chapter four, stable acoustic traps with three-dimensional manipulating using electronic steering of large heavy objects are presented. First, simulation of three-dimensional traps with the aid of gravity was performed to study the variable space and optimize the traps used for large heavy spherical objects. Similar to the results of chapter three, the relationship between target sizes and beam shapes was found for the stability of off-axis steering and traps. Spherical targets of various sizes and materials were successfully trapped and manipulated *in vitro* and for the first time *in vivo*. The mechanical and electronic steering of spherical glass bead inside a live pig bladder was demonstrated under safe power levels and was monitored non-invasively by ultrasound imaging.

Lastly, chapter five summarizes the work and findings leading to the successful manipulation of large objects using acoustic tweezers. Future work and areas of studies to improve and push this science forward are presented. Potential work includes the ability to produce negative axial acoustic forces for pulling, the use of acoustic radiation torque to rotate, hold or detach objects, and the contribution of nonlinear wave propagation on the resulting acoustic force. Furthermore, chapter four includes a discussion of the limitations of the array used in this work and proposed developments for advancing the technology. Some developments include the use of real-time scanning methods such as time-reversal to maintain the strength of the acoustic trap along the desired manipulation path and coupling with a dynamic imaging technique to continuously locate and track the object's motion. Thus, leading to a comprehensive system of acoustic tweezers able

to control large objects in three dimensions for a wide range of applications, such as, non-invasive medical treatment, container less transport, laboratory applications and manufacturing techniques.

Ch 2: CHARACTERIZATION AND COMPENSATION OF VIBRATIONAL NON-UNIFORMITY FOR A PHASED ARRAY

2.1 INTRODUCTION

Multi-element focused ultrasound phased arrays have been used in therapeutic applications to treat large volumes by electronic steering to the focus, to target multiple simultaneous foci, and to correct aberration caused by inhomogeneous tissue pathways. There is an increasing interest in using arrays to generate more complex beam shapes and corresponding acoustic radiation force patterns for noncontact manipulation of particles [9], [35], [10]. One emerging application for this effect is noninvasive repositioning of urinary stones to facilitate stone clearance [32], [33], [31]. Vortex beams are characterized by null pressure in the center and a toroidal-like acoustic beam shape [36], [37], [38]. Such beams offer the possibility of pulling [39], [40], [41] pushing [39], [19], or trapping an object [10], [20]. In the idealized case, a continuous axisymmetric transducer can generate a vortex beam if the phase varies linearly with the polar angle around the transducer's acoustic axis with a maximum phase delay of $2\pi M$ radians. Here M is an integer number known as the topological charge, which controls the wavefront helicity and the overall toroidal width.

In this effort, we seek to reproduce such beams using a phased array transducer. Although such an implementation involves inherent challenges related to finite element sizes, phased arrays do provide the appealing potential to electronically steer beams and any trapped objects in 3D space. To realize the generation of vortex beams with a phased array transducer, the first step is to characterize its output in order to account for non-uniform behavior of each element. Successful characterization and compensation of non-uniformity will provide a basis for future efforts to

synthesize specific beam shapes to trap and manipulate objects such as urinary stones by means of acoustic radiation force.

The simplest method to characterize a focused array involves element-by-element measurements for which the hydrophone is placed in the geometric focus of the array and each element is excited individually to measure amplitude and phase differences among the elements [42], [43]. Several studies have utilized this method to apply phase corrections to yield a high focal intensity in the presence of a scatterer [44], [45], [46] and to test focal steering capabilities [43], [47], [48]. Time reversal [49], [50], [8] is another method which uses the reflection of acoustic signals generated, and often received, by each element from a focal target. It has been used to correct for phase aberration as well as non-uniform attenuation introduced by propagation through heterogeneous media [51], [52]. In a third method, element-by-element measurements were taken at multiple locations in the field. This has been used to determine array excitation vectors using a pseudo-inverse method [44], to maximize focal intensity and to produce multiple foci [53], [54], [55]. In the current paper, a method is developed to determine the required individual adjustments to the vibratory amplitude and phase of each element of the array as needed to generate accurate and uniform complex 2-dimensional beam shapes.

Acoustic holography and element-by-element method are used here to quantify the complex output of every element. In acoustic holography, a 2D scan of the field produced by excitation of the entire array is measured and used as a boundary condition to reconstruct the field at the transducer surface or anywhere in 3D space [56], [57]. Holographic back-propagation of vortex beams was introduced in Ref [36]. The evolution of an unfocused vortex beam along the propagation axis was examined. Holography captures effects caused by cross-talk and eliminates the variability between elements when driven sequentially due to the transient response of the

power supply. It has been shown that power sources alone can introduce phase differences between elements that reduce focal intensities by 20-30% [45], and such effects are missed with an element-by-element approach. Compared to holography, element-by-element methods have a limited ability to quantify the vibrations of each element. In particular, such approaches typically require an assumption that each element vibrates uniformly over some prescribed aperture. With this assumption, a pressure measurement at a single point in the far-field can be readily related to the element's vibration magnitude. However, this approach cannot account for non-uniform vibrations within each element or effective element sizes that differ from assumed values. Because each element's effective aperture influences its directivity, the synthesis of complex 2D fields will be hindered by such assumptions. Moreover, element-by-element approaches are inherently incapable of capturing the effects of crosstalk among elements and amplifier channels.

The purpose of this study was to characterize a 1.5 MHz 256-element transducer array, compensate for differences in phase and amplitude between the array elements, and demonstrate an improvement in the array performance in the generation of uniform vortex beams. First, the transducer was matched electrically to a Verasonics Data Acquisition system (VDAS) for efficient power transfer. Then element-by-element and holography measurements were acquired to quantify each element's output. As a part of the holography approach, a method was developed to identify the performance characteristics of each element. Compensation strategies based on both measurement approaches were implemented to equalize the phase and amplitude across all elements. The performance of these compensation strategies was tested by evaluating the uniformity of vortex beams.

2.2 METHODS

The transducer characterized in this study is a piezocomposite array manufactured by Imasonic, SAS (Voray sur l'Ognon, France) [58]. The array is geometrically focused with a spherical radius of curvature of 120 mm. The mechanical aperture is 160 mm; the active acoustic aperture is 147 mm, including a central opening of 40 mm in diameter (Figure 2.1). The 256 piezocomposite elements are arranged in 16 spirals with each spiral having 16 elements. The diameter of each element is 7 mm with inter-element gaps of 0.5 mm. The face of the transducer is acoustically matched to water at a nominal frequency of 1.5 MHz to yield a 1.2–1.8 MHz working frequency range and a manufacturer-reported efficiency in excess of 63%.

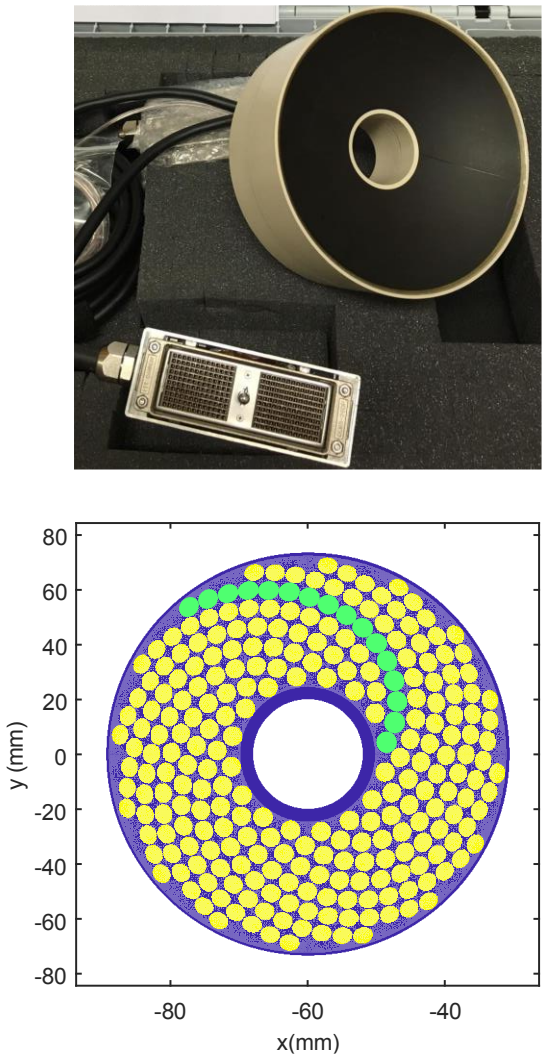

Figure 2.1: Top) a photograph of the array. Bottom) 2D layout of the array. The array has 16 spirals with 16 elements in each spiral for a total of 256 elements. Each element has a nominal diameter of 7 mm with inter-element gaps of 0.5 mm. Central opening is 40 mm and active acoustic aperture is 147 mm (© 2018 IEEE).

2.2.1 *Electrical measurements*

The transducer was driven electrically using a Verasonics Data Acquisition System (V-1, Verasonics, LTD., Kirkland, WA), a research ultrasound engine with a 1200-W external power source (QPX600DP, Aim-TTI, Cambridgeshire, UK). The array was electrically tuned using a series inductor for each element to eliminate the imaginary component of the impedance and thus to optimize the driving efficiency at 1.5 MHz. The inductors were mounted on two printed circuit

boards. Ferrite-core shielded inductors were used to reduce the electrical crosstalk between the channels. Crosstalk was measured by triggering a single element and monitoring the voltage output of an adjacent element on the circuit board. The maximum voltage on all the monitored adjacent elements was measured to be 0.08% of the voltage signal on the excited element on each circuit board, which was insignificant.

All elements were tuned with the same inductance. The impedance after matching was measured using an impedance analyzer (Antenna Analyzer AIM-4170D, Array solutions Sunnyvale, TX) and compared with values before matching (Table 2.1). Ideally, the inductors network should be lossless; however, an increase in the average real impedance of 22% was measured, which translated to 18% power losses in the inductors. However, a comparison before and after tuning shows that the electrical power delivered is 7 times the power delivered without the electrical tuning. A small nonzero imaginary component remained on most elements (Table 2.1) as the inductors were chosen in discrete values only, and the inductances were measured to be slightly smaller than their nominal value at high frequencies. The total electrical power delivered to the transducer (W_{tot}) was calculated using the following equation:

$$W_{tot} = \sum_{j=1}^{256} W_j = \sum_{j=1}^{256} \frac{|V_j|^2}{2} Re\left(\frac{1}{Z_j}\right) \tag{2.1}$$

where Z_j is the complex electrical impedance in Ohms and V_j is the voltage on element j measured after matching of each element. In Table 2.1, the negative imaginary impedance indicates that the reactive component is capacitive.

Table 2.1: Average impedance (Ohms) of array elements before and after tuning with circuit boards (© 2018 IEEE).

Impedance	Re(Z) (Ohms)	Im(Z) (Ohms)
Before	59.1 ± 3.8	-207.9 ± 3.2
After	72.2 ± 4.9	-13 ± 6.6

2.2.2 *Acoustical measurements*

A total of four experiments were performed in the study at the transducer operating frequency of 1.5 MHz: 1) element-by-element measurements for acoustic characterization of the array and equalization of the element outputs and 2) holography measurements for a comparable acoustic characterization; 3) radiation force balance (RFB) measurements [59] to independently quantify the power output of the array; and 4) two-dimensional hydrophone scans to measure the uniformity of the vortex beam shapes before and after compensation. All experiments were performed in a tank of degassed and deionized water. Except for RFB experiments, all measurements utilized a capsule hydrophone (HGL-0200 with AH-2020 preamplifier, Onda Corporation, Sunnyvale, CA). Per the manufacturer's calibration, the integrated hydrophone sensitivity at 1.5 MHz was 416 mV/MPa. Hydrophone directivity at 1.5 MHz was measured separately and used to provide corrections for improved accuracy. Hydrophone location was controlled using 3D positioner systems based on stepper motors and linear slides with resolutions less than 10 μm per step (Velmex Inc, Bloomfield, NY). A function generator (Model 3500B, Keysight Technologies, Inc., Englewood, CO) was used to trigger the VDAS and synchronize data acquisition on an oscilloscope or digitizer. For the holography scan, hydrophone signals were recorded using a 14-bit digitizer board (Razor 14, Gage by DynamicSignals LLC, Lockport IL); for other experiments, hydrophone measurements were recorded using a digital oscilloscope (Model 3034A, Agilent Technologies Inc, Santa Clara, CA).

The angular sensitivity response of the hydrophone was measured up to an angle of 40^{o} in an open water bath in the far field of a 1.5 MHz flat piezoelectric source with 1.6 cm diameter. The response was measured along four different azimuthal angles by rotating the hydrophone around its axis and repeating the measurements twice for each angle. The average of these measurements

at each angle was then taken to produce the angular response curve shown in Figure 2.2. Based on the small variation, the curve is assumed axisymmetric. The acoustic characterization section of this paper reports the various acoustic output and efficiency measurements after compensation for the hydrophone's angular response while a comparison to the values before compensation are reported in discussion.

Losses due to absorption of the fundamental frequency (1.5 MHz) were ignored in the analysis, since they were negligible (0.054 dB over the longest propagation distance to the acoustic focus of 120 mm). Nonlinear propagation effects were neglected in all acoustic measurements. Focal measurements were performed at low voltage levels while holography and radiation force balance measurements were performed prefocally. The level of the second harmonic pressure was less than 7% in all measurements, yielding an intensity level less than 0.5%, which is below the nonlinear intensity threshold criterion of 10% in standards [60].

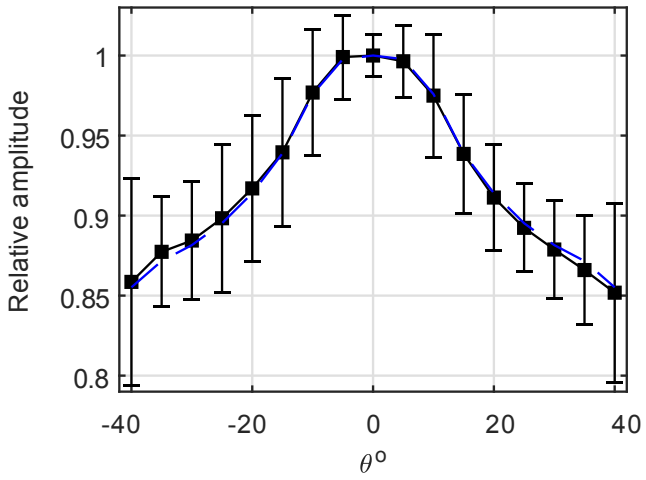

Figure 2.2: Angular response up to 40º of the HGL – 0200 Onda capsule hydrophone (sensing element diameter 200 μm). Solid black curve represents experimental data with error bars of 8 angular sweeps; each sweep is performed twice along a different azimuthal angle. Dashed blue line represents the average of the left and right halves of the experimental data, based on a symmetric response assumption (© 2018 IEEE).

2.2.2.1 Element-by-element in the far-field measurements

In the element-by-element measurements, the hydrophone was placed at the acoustic focus of the phased array, which is in the far-field of all elements (Figure 2.3). The focus of the array was determined as the location where the hydrophone recorded the maximum pressure amplitude while all elements were driven at the same voltage level and without applying any phase delays. Each element was then driven independently at 1.5 MHz with a 128-cycle burst. The waveform was recorded, and the amplitude and phase were calculated using a discrete Fourier transform (DFT) over the steady state portion of the waveform. The CW boundary condition (pressure) at each element surface was then estimated by assuming each element can be modeled as a flat, circular piston source with uniform normal velocity, $v_0 = P_0/\rho c$. In the far-field approximation,

$$P_o = P_R \frac{R\lambda}{\pi a^2} \tag{2.2}$$

$$W = P_R^2 \frac{R^2\lambda^2}{2\rho c\pi a^2} \tag{2.3}$$

where P_0 is the effective surface pressure amplitude, P_R is the pressure amplitude measured at the focus after applying relevant correction for directivity. Considering that the hydrophone was aligned with the array axis, the angle of incidence was determined as the angle between the array axis and the vector defined by the location of an element of interest relative to the hydrophone. Then, the corresponding relative amplitude of the directional response was used to apply a correction. R is the focal distance, a is the nominal radius of each element, W is the acoustic power of the (piston) array element, c is the speed of sound in water, ρ is the density, and λ is the ultrasound wavelength. Based on the measurements for each element, the total acoustic power output and the overall transducer efficiency were calculated.

2.2.2.2 Acoustic holography

In the holography scan, all elements were driven simultaneously with a 128-cycle burst. Hydrophone signals were acquired at each location over a 2D plane oriented approximately perpendicular to the acoustic axis. The scan was performed with the center of the scan region located 40 mm proximal to the transducer relative to the acoustic focus (Figure 2.3). The scan comprised an 88 × 88 mm grid with a step size of 0.5 mm. From the recorded hydrophone signals, the CW hologram was defined by analyzing a time window lasting for 15 acoustic cycles with a delay time of 111.17 μs after triggering, and calculating pressure amplitude and phase of the windowed signal using DFT. The time window was chosen based on a VDAS delay of 2.17 μs before actual waveform generation, a delay for acoustic propagation from each element to each point within the scan plane, and a transient ring-up time for the array to reach a steady state. Using the angular spectrum calculated from the raw holography measurements, we compensated for the hydrophone directivity and then calculated the power traversing the scan plane [61] using the following relations:

$$S(k_x, k_y) = \iint P(x,y)\, e^{-ik_x x - ik_y y}\, dxdy \tag{2.4}$$

$$\tilde{S}(k_x, k_y) = \frac{S(k_x, k_y)}{D(\theta(k_x, k_y))} \tag{2.5}$$

$$W = \frac{1}{8\pi^2 \rho c} \iint_{k_x^2 + k_y^2 \le k^2} \sqrt{1 - \frac{k_x^2 + k_y^2}{k^2}} \left|\tilde{S}(k_x, k_y)\right|^2 dk_x dk_y \tag{2.6}$$

where $S(k_x,k_y)$ is the measured angular spectrum of the beam, k_x and k_y are the wave vector components in x and y, $P(x,y)$ is measured complex amplitude of the pressure field, $D(\theta)$ is the directivity, and θ is related to $k_x$and k_y by $\sin\theta = \frac{\sqrt{{k_x}^2 + {k_y}^2}}{k}$. After compensation for the angular response of the hydrophone, the inverse Fourier transform was used to recover the true complex

pressure amplitude distribution from the recovered angular spectrum using the following expression:

$$\tilde{P}(x,y) = \frac{1}{4\pi^2} \iint \tilde{S}(k_x, k_y)\, e^{ik_x x + ik_y y}\, dk_x k_y \tag{2.7}$$

When considering holography measurements and the physical transducer, there are two relevant coordinate systems: one aligned with the transducer and the corresponding beam's *z*-axis, and another aligned with the axes of the hydrophone positioner (*x*, *y*, *z*). The acoustic beam *z*-axis is not generally coincident with the hydrophone *z*-axis [57], but the misalignment can be corrected by projecting the field to different transverse planes in the positioner coordinates and identifying movement of the beam axis relative to these coordinates. After quantifying the misalignment in this way, a transformation basis between the positioner and transducer coordinates was defined, and the measured hologram was interpreted accordingly. For simplicity, in all subsequent figures presented in the manuscript, all coordinates (*x*, *y*) shown are either describing hydrophone axes if shown in a focal plane, or array axes if shown on the array surface.

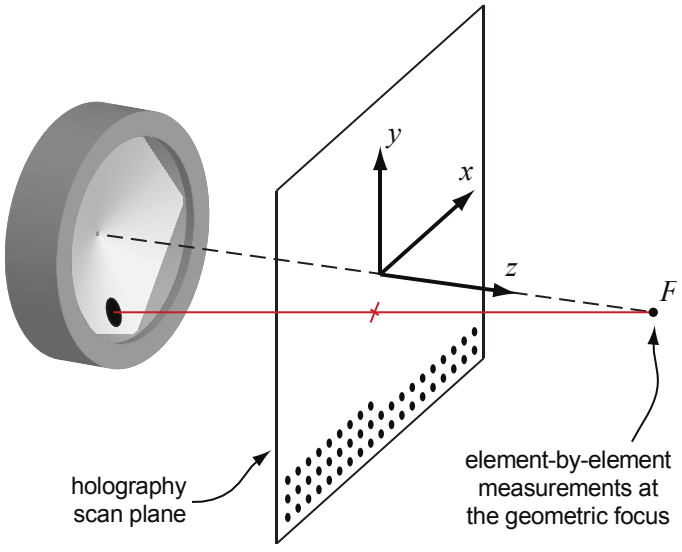

Figure 2.3: Diagram of the experimental setup. The acoustic focus (F) at which element-by-element hydrophone measurements were taken was determined as a maximum of pressure amplitude when all elements were triggered simultaneously. The holography scan plane with an area of 88 × 88 mm was 40 mm prefocally. The hydrophone recorded the waveform at 0.5 mm

increments for a total of 31,329 points. Sample points shown as dots are at larger increments for illustration (© 2018 IEEE).

After the alignment of coordinates, the pressure field recovered from the inverse transform was used to back-project the field to a spherical surface that corresponded to the physical surface of the transducer using the Rayleigh integral [57]. From reconstructed normal velocities of the transducer surface, the preliminary boundaries of individual elements were identified based on the maximum of the gradient of velocity amplitude along the transducer surface. Afterwards, the surface normal velocity profile was manually inspected to remove spurious pixels connecting adjacent elements. The pixels inside each boundary were then used to define the corresponding element's center location as the centroid of these pixels. Final element boundaries were drawn around each of these calculated locations as 7 mm diameter circles to agree with reported manufacturer specifications. The information inside each element's boundary was collected to calculate its acoustic output as follows:

$$A_j = \frac{1}{N}\sum_{i=1}^{N} A_{ij} \tag{2.8}$$

where A_j is the complex amplitude either of normal velocity or pressure per element j, and N is the number of pixels with their centroid inside an element. The power emitted by the element j is $W_j = \frac{1}{2}\sum_{i=1}^{N} \mathrm{Re}\left(P_{ij}^{*} U_{ij}\right) \cdot da_i$, where, da_i is the projection of the square surface area of pixel i onto the spherical array surface, and P_{ij} and U_{ij} are the complex amplitudes of pressure and normal velocity, respectively.

2.2.2.3 Radiation force balance measurements

Radiation force balance measurements were carried out using a flat 10-cm-diameter absorber brush [62] suspended from a precision scale (Entris623i-1S, Sartorius, Göttingen Germany) and

placed 1 cm proximal to the acoustic focus. A 50-μm thick Mylar membrane was placed between the transducer and the absorber to minimize acoustic streaming [63], and the transducer was operated at a 1% duty cycle to minimize heating of the absorber [64]. Based on ray acoustics theory [65], the following correction factor was multiplied by the acoustic power to correct for the geometry of a focused source with a central hole:

$$C.F. = 2/(\cos\alpha_1 + \cos\alpha_2), \tag{2.9}$$

where α_1 and α_2 are the angles which correspond to half apertures of the central opening and the outer edge of the array.

2.2.2.4 Equalizing outputs of the array elements (uniformity)

Equalizing the element outputs includes phase corrections to have all elements firing in phase and amplitude equalization. In order to find the phase delays among the elements for the element-by-element measurements, the recorded signal of each element was used to calculate the relative phase delay between the elements. For the holography scan, the phase delays among elements were found using the phase values from the complex normal velocity of each element given by Eq.(2.8). Phase delay corrections were then applied to the VDAS for both measurements.

Then a VDAS apodization scheme was used to equalize the element amplitude outputs by controlling the voltage delivered to each element. The VDAS takes an apodization factor as input and uses pulse-width modulation to control the number of 'on' and 'off' clock cycles in a transmit event to set the voltage amplitude on a specific channel. In order to measure the relative electrical output vs the apodization factor applied in the VDAS script, the voltage was measured on a single element for apodization factors ranging from 0 to 1 in increments of 0.1, where 0 denotes being fully off and 1 denotes being fully on. To obtain the required driving voltage for each element from both characterization methods, the reciprocals of effective normal velocity amplitudes from

element-by-element measurements and the reciprocals of surface normal velocity amplitudes from holography were found and normalized relative to the largest value of each method separately. The normalized reciprocals were used as scaling factors to control the voltage output delivered to each element, such that the lowest element was scaled by unity and the rest by a factor less than 1. Then the scaling factors were used to back solve and determine the required apodization factors applied in the VDAS script to control the voltage delivered to the elements and ultimately equalizing the amplitude outputs.

2.2.2.5 Generation of vortex beams

Vortex beams with topological charges, M = 0 (focused), 1, and 4, were generated after applying amplitude and phase corrections, in order to test the effectiveness of the characterization methods for achieving uniformity of the beams. We ran the VDAS script with the relevant apodization factor for each element to equalize amplitudes. In addition to equalizing phase delays, further phase delays were imposed to synthesize different vortex beams. The phase delay imposed on each element was calculated based on its nominal location (x_i, y_i). For a given M, the total phase delay around the array aperture increases from 0 to $2\pi M$, and the phase on element i is given by:

$$M \times \arctan\left({}^{y_i}/_{x_i}\right) \tag{2.10}$$

Two-dimensional hydrophone scans of multiple vortex beam shapes in the focal plane were measured before and after the application of equalization corrections. Pressure amplitude and phase were calculated from waveforms recorded at each spatial location in the scan, as described for the holography scan. The intensity calculated from measurements were then compared to simulated intensity to evaluate the performance of the characterization methods. Simulations used the Rayleigh integral to calculate pressure fields that would be generated by an idealized

representation of the array – uniformly vibrating elements were assumed, with element locations and sizes matching manufacturer specifications.

2.3 RESULTS

2.3.1 *Element-by-element in the far-field measurements*

Using the recorded pressure waveform for each element, the effective pressure amplitude and phase at the element's surface were found and then used to calculate the radiated acoustic power from Eqs.(2.11) and (2.12). For all elements, the total acoustic power was calculated to be 91.4 W. The applied electrical power was 136.4 W yielding an efficiency of 65.5%, which falls within the specifications provided by the manufacturer.

2.3.2 *Holography*

The holography results are presented to show the alignment of the axes, the element locations and borders, the effect of the directivity on the surface normal velocity vibration profile, and finally the acoustic power output and efficiency calculations.

2.3.2.1 Holography axes alignment

Before using the measured hologram to reconstruct vibrations on the transducer's surface, corrections were performed for misalignment between the hydrophone and transducer coordinates. The uncertainty in the alignment of the acoustic beam axis with the *z*-axis of the 3D positioner was found by forward projecting to the focal plane away from the array. The focus appeared to be located at (0.15, -0.25) mm rather than at (0, 0). Using this offset from the origin over the propagating distance (δz = 40.0 mm), the misalignment angle between the axes was found to be 0.42^{o}. After correcting for the angular misalignment and back-projecting to the array surface, a

more uniform phase distribution was obtained (Figure 2.4). This misalignment only affects the surface phase distribution and has no visible effect on the amplitude.

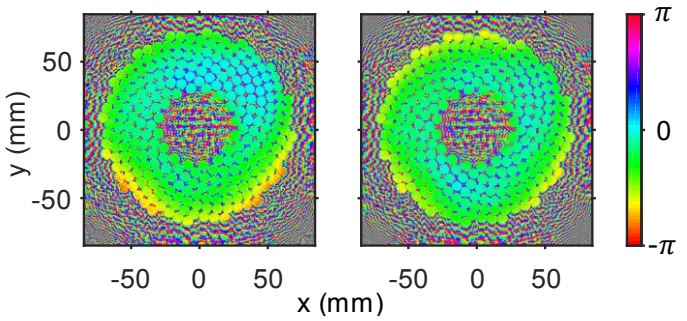

Figure 2.4: Phase distribution (radians) back-projected onto the transducer surface before (left) and after (right) correcting for the misalignment of the array and holography coordinates. Before correction, the slight misalignment is observed as a non-uniform phase distribution varying from top to bottom on the array surface (© 2018 IEEE).

2.3.3 *Element locations and sphericity*

Element locations identified from reconstructed vibrations at the transducer surface were compared to the nominal locations provided by the manufacturer. To perform this comparison, we note that the orientation of array elements around the beam axis was not controlled relative to any absolute coordinate system. Accordingly, the holographically reconstructed element positions were rotated around the beam axis for initial alignment relative to the manufacturer-specified coordinates. Then an iterative algorithm was executed to optimize alignment by minimizing the sum of the absolute differences between nominal and reconstructed element locations. The minimization search was carried out by first rotating the holographically reconstructed array pattern in the *xy*-plane about the *z*-axis. Second, this pattern was shifted in the *xy*-plane while conserving the radius of curvature of the surface where the vibration velocity pattern was reconstructed. These two steps were repeated iteratively using an angular search with a step size of 0.001^{o} from -5^{o} to 5^{o} and a translational search with a step size of 0.001 mm from -2 mm to 2 mm. The optimal alignment found in this way yielded an average distance between nominal and

reconstructed locations of 0.107 mm with a standard deviation of 0.055 mm. Additionally, the diameter of each reconstructed element was found to be 6.99 mm with a standard deviation of 0.2 mm, which agrees with the nominal elements 'diameter of 7 mm.

From this alignment comparison, an interesting characteristic of the transducer's acoustic surface was identified. In particular, it appears that the transducer was made from two physically separate halves that were joined together in the manufacturing process. The line representing that split in the transducer surface was captured by the holography results illustrated in Figure 2.5, which shows the surface normal velocity profile after directivity compensation along with the identified element boundaries shown in white.

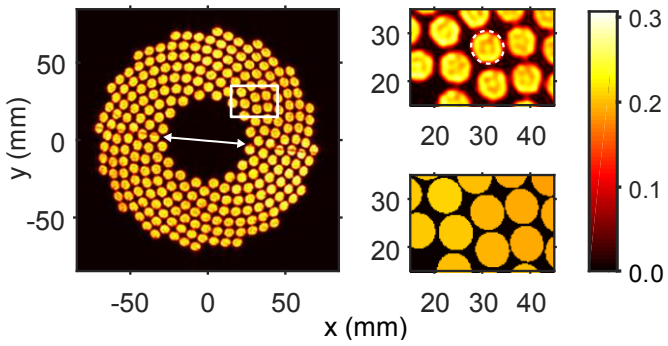

Figure 2.5: Left) Transducer's surface normal velocity amplitude profile, |U| (m/s), obtained with compensation for the hydrophone directivity. The arrow marks the line along the hemispherical surface splitting the transducer surface in two halves due to the manufacturing process. Right) Close-up of the elements in the upper right corner of the array; top) showing the surface normal velocity amplitude profile, |U| (m/s), with an example of the calculated boundaries of the elements shown as a dashed contour on a single element, and bottom) showing the averaged and localized surface normal velocity amplitude, |U| (m/s), per element after post-processing of the holography results. Note that the reconstructed surface normal velocity (top) is not uniform within each element which may be explained not only by some true heterogeneity of the source vibration, but by the omission of evanescent wave components in the far-field holography reconstruction used (© 2018 IEEE).

2.3.3.1 Acoustic output and efficiency calculations

The normal velocity output and acoustic power per element were calculated from Eq.(2.8). The acoustic power from the measured hologram in the scan plane was 308.9 W. After performing back projection to the transducer surface and localizing the output per each element, the sum of the acoustic power from all elements was 301.0 W. Although no absorption losses were included in backpropagation, the difference of 2.53% of the total power was from including only radiation from inside the 7 mm element boundaries.

In Figure 2.2, it is shown that the angular response was measured up to 40 degrees; however, the maximum angle the hydrophone reached with the transducer in the holographic scan was 50 degrees. The sensitivity past 40^o was assumed to be linearly decreasing down to a value at 90^o equal to 8% of the value at 40^o. The linear curve is defined to be a lower bound to the theoretical sensitivity value specified by the manufacturer and given by the expression for a radiating source in free space in Ref [66]. For verification purposes, we compared the power values gained from using the linear curve – a lower bound – against an assumed constant sensitivity curve beyond 40^o – an upper bound – as the most conservative limit. The acoustic power was measured to be 306.3W and 308.9W for constant and linear directivity curves, respectively, which is an increase of less than 1%. The electrical power was calculated to be 463.2W, which resulted in efficiency values between 66.1% and 66.7%, depending on which directivity curve was used. This estimation beyond 40^o was not required for the element-by-element, since the hydrophone was placed in the focus, making a maximum angle with the outermost transducer elements less than half the focal angle of 37^o.

Element-by-element measurements were performed at 55% of the driving voltage of holography, yielding an electrical power of 136.4W. Holography required higher voltage levels to obtain a good signal-to-noise ratio, since the hydrophone was placed 40 mm prefocally (averaging

would have prolonged the scan time considerably). Moreover, making element-by-element measurements at the drive level used for holography was not performed in order to avoid exposing the hydrophone to high pressures at the focus.

2.3.4 *Radiation force balance measurements*

A radiation force balance was employed to provide an independent measure of acoustic power. To eliminate potential inconsistencies introduced by the driving electronics, the input electrical power was measured and used to normalize these acoustic power measurements in terms of overall transducer efficiency. The acoustic power measured at the voltage level of the holography scan was 315.8W. The average efficiency calculated from radiation force balance measurements at different voltage input levels was 68.3%, while the efficiency calculated from the holography scan (66%), element-by-element measurements (65.5%) and manufacturer's reported efficiency (>63%). The reported efficiency by the manufacturer was calculated using 32 central elements only rather than the whole array. However, our measurements indicate that the outer elements have efficiencies similar to the inner 32 elements.

2.3.5 *Equalizing the output of the array elements*

The VDAS apodization factor vs the voltage output amplitude was measured (Figure 2.6). Since the VDAS apodization factor (A_p) indicates full power when equal to unity and off when zero, it would be theoretically expected for the resulting amplitude of the output to follow a sinusoidal curve, $\sin\left(\frac{\pi}{2}A_p\right)$, where A_p is the apodization factor varying from zero to unity. However, measurement of the voltage amplitude output vs the various apodization factors showed deviation from this curve that could be a result of multiple sinusoidal summation, and thus the

curve was approximated by a 5th degree polynomial using a least-squares fit. The polynomial curve was used to calculate the desired apodization factor to equalize all elements' amplitude outputs based on the element-by-element and holography results (Figure 2.5). Phase corrections based on both methods were applied to have zero relative phase delay between all elements. The pulse width

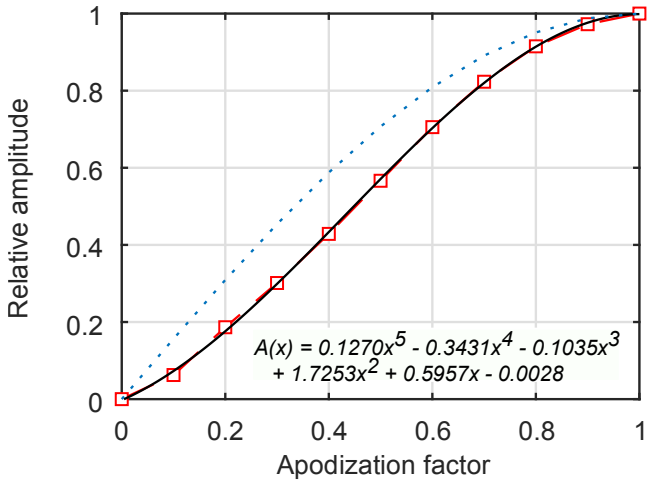

Figure 2.6: Apodization factor vs relative amplitude output of the VDAS for an extended burst for all elements firing simultaneously. The dashed red curve represents the measurement results and their 5th degree polynomial fit (solid black line); both compared with the pulse width modulation scheme assuming a sinusoidal curve (dotted blue line). The 5th degree polynomial fit is displayed with restriction of having a value of zero at zero and unity at one (© 2018 IEEE).

modulation scheme in the VDAS is constrained since it is only possible to specify an integer number of 'on' cycles in a half transmit clock. This constraint on temporal resolution limits the resolution with which each element's amplitude can be controlled. Figure 2.7 shows the desired relative amplitude value (solid black line) vs the VDAS output (dashed red line). As can be seen, the discretization of output levels for some elements causes a non-ideal equalization of the array.

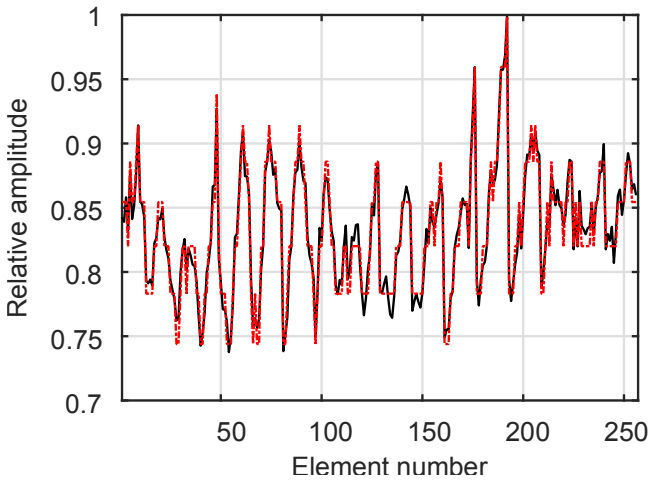

Figure 2.7: Effect of VDAS rounding to whole integers in defining the number of "on-clock" cycles in the apodization scheme. VDAS rounds up or down to the nearest integer to define the number of "on-clock" cycles in the apodization scheme, which limits control of the resolution of the desired output as it underestimates or overestimates the needed amplitude. The VDAS output (solid black line) is shown to deviate from the desired output (dashed red line) (© 2018 IEEE).

2.3.6 *Generation of vortex beams*

Two-dimensional scans were performed in the focal plane of beams with multiple topological charges (M = 0, 1, and 4) as generated with and without equalization of element outputs. From such measurements, the performance of equalization based on each characterization method was quantified by comparison with idealized simulations. A performance metric was calculated based on error in the intensity distribution relative to the corresponding simulation as follows:

$$E = \frac{\iint |I(x,y) - I_s(x,y)| dx\, dy}{\iint I_s(x,y)\, dx\, dy},$$

where I_s the 2D intensity distribution from simulation and I is the 2D intensity distribution – normalized with respect to the total power in I_s – from before or after equalization as obtained by either element-by-element or holography.

Figure 2.8 shows normalized intensity distributions corresponding to measurements in the scan plane and corresponding simulation results. All the vortex beam shapes scanned had the same input electrical power; however, the acoustic energy captured in the section of the scan plane

shown in Figure 2.8 varied slightly with the apodization factors from each method. Therefore, all intensity scans in Figure 2.8 were normalized to the acoustic power in the scan plane of the simulation results to calculate the relative error. Table 2.2 presents errors associated with array

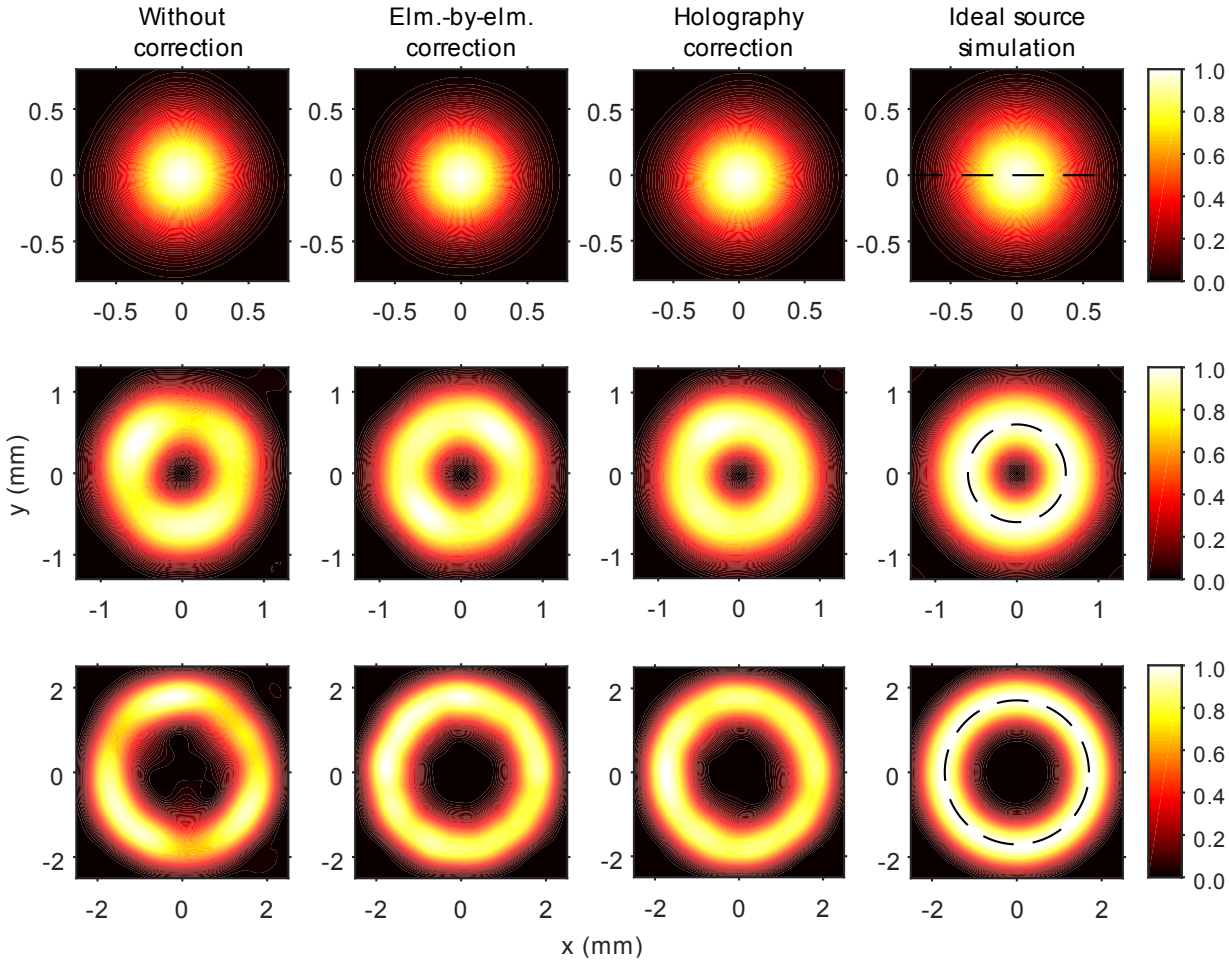

Figure 2.8: Normalized 2D intensity distribution to its maximum value in the focal plane for different M values: top row) M = 0, middle) M = 1, and bottom) M = 4, for (from left to right) measurements before and after apodization using element-by-element measurements and holography results, and simulation. The corrections improve the uniformity of the focal rings and final experimental results look more like the simulation. The dashed line in the left column shows the line along which the sectional and circumferential cuts were taken for use in Figure 2.9 (© 2018 IEEE).

non-uniformity as calculated from the intensity distributions in Figure 2.8. Figure 2.8 and Table 2.2 show that both element-by-element measurements and holography attain improved uniformity for higher values of topological charge *M*. Values for *M* = 0 show that element-by-element

equalization performs worse than no equalization– 15.3% vs 10.1%, while holography equalization provides minimal improvement. However, Figure 2.8 illustrates that both equalization methods yield more circular intensity distributions with the element-by-element method providing the narrowest focal region. Overall, holography outperforms element-by-element measurements and reduces intensity non-uniformity by a factor of about 2 relative to the case with no equalization.

Table 2.2: Non-uniformity of intensity of acoustic beam shapes before and after equalization (© 2018 IEEE).

Topological charge (M)	Before equalization	Element-by-element equalization	Holography equalization
0	10.1%	15.3%	9.0%
1	10.8%	9.1%	5.3%
4	13.3%	7.8%	7.4%

Sectional cuts along the x-axis for $M = 0$, and circumferential cuts at the radial distance with the maximum intensity values for $M = 1$ and 4 from the simulation were also examined for comparison of the performance of the different equalization methods (Figure 2.9). In a fashion similar to Table 2.2, the residual relative percent error is plotted in Figure 2.9 along the dashed black lines shown in the right-hand column of Figure 2.8.

Both equalization schemes improved the intensity distribution for most cases (Figure 2.8 and Figure 2.9). For $M = 0$ in Figure 2.9, the peak intensity obtained using both equalization methods (black and red dashed line) is higher relative to the simulated data ($y = 0$) because it has a wider distribution of intensity than the measured cases, while the power in all beams is the same. Circumferential cuts for $M = 1$ and 4 show the overall improvement in uniformity between the spatial distribution. For instance, at $M = 1$ from the holography method, the residual error is in general less than that from far-field measurements with the error oscillating between 0 and -5%

except a large peak of 10% at $\theta = 125^{o}$. Similarly, for $M = 4$ holography exceeds element-by-element measurements, only under-performing on the interval from $\theta = 160^{o}$ to 195^{o} and 0^{o} to 50^{o}. Interestingly, a close inspection of Figure 2.9 shows the effect of the equalization scheme on the extrema of the non-equalized case. It is noticeable that uniformity is improved as spatial extrema are flattened. However, there are areas where a maximum or a minimum was overcompensated for, such as at $\theta = 285^{o}$ for $M = 1$, or $\theta = 150^{o}$ for $M = 4$. Similar to the 2D intensity plots of Figure 2.8 and the error percent calculated in Table 2.2 , the radial cuts of Figure 2.9 display more regions of high non-uniformity distribution from simulation are present in the equalization results of the element-by-element than the holography method.

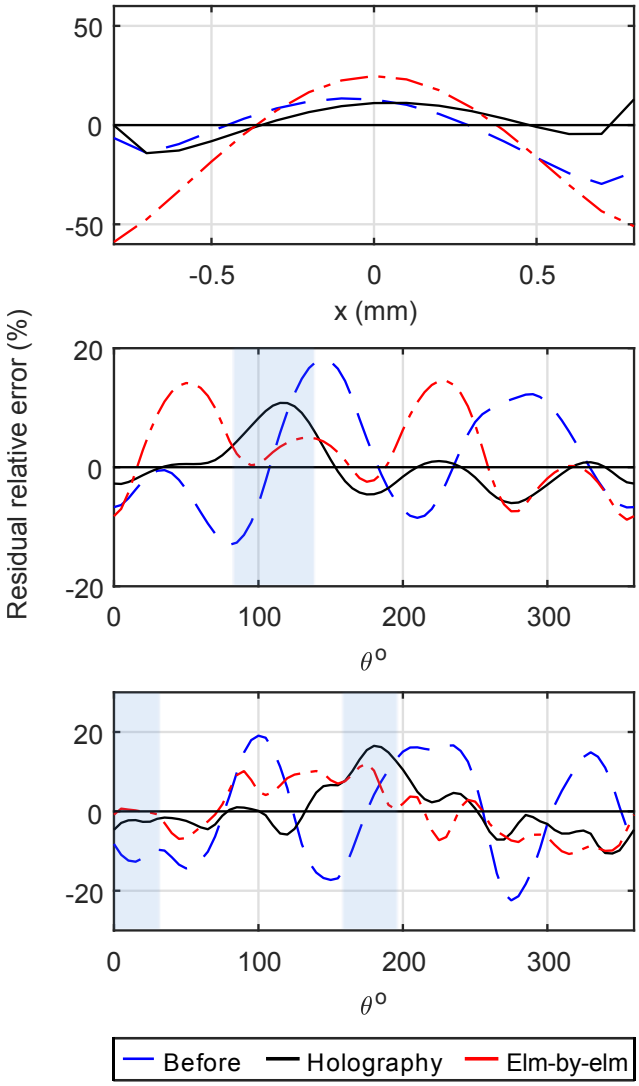

Figure 2.9: Sectional and circumferential cuts of residual relative error (%) to the simulation of an ideal array output for M = 0 (top), M = 1 (middle), and M = 4 (bottom). Sectional cut is taken along the x-axis for M = 0 (top) and circumferential cuts are taken at the radius with the maximum intensity value for M = 1 and 4 (middle and bottom, respectively). Shaded areas for M = 1 and 4 highlight the sections where holography under-performs element-by-element measurements (© 2018 IEEE).

The phase distribution of the various vortex beam shapes was measured to quantify the uniformity of the source before corrections. The distribution was plotted before and after applying corrections. The phase distribution before corrections (second column of Figure 2.10) shows slight variations along the radial direction inside the main circular boundary. Additionally, at $M = 4$, non-

ideal phase distribution is observed. Such results are the consequence of small disturbances in the field introduced by the non-ideality of the source. For instance, due to manufacturing errors and tolerances, the array deviates from an ideal spherical surface. Such deviations introduce small perturbations in the acoustic field which lead to instabilities in the low amplitude regions of vortex beams with $M>1$, as has been shown in optics [67], [68], [69]. Furthermore, for elements intended to have the same phase, a maximum time delay of 3 nanoseconds was measured before applying phase corrections. Such a small value indicates that the transducer's elements are well within phase of each other and the jitter in phase between them is negligible.

Table 2.3: Comparison of error norm of simulation of intensity of acoustic beam shapes from holography results with either amplitude equalization or phase corrections (© 2018 IEEE).

Topological charge (M)	Before equalization	Amplitude equalization only	Phase corrections only
0	10.4%	9.6%	6.3%
1	10.8%	9.9%	4.2%
4	15.3%	14.5%	4.4%

To find the contribution of the amplitude equalization and phase corrections to the uniformity, the results of elements' output obtained from holography were used to simulate the beam shapes applying no corrections, amplitude equalization only, or phase corrections only. The three simulation cases were compared to simulation with ideal phase and amplitude, and the error in the intensity distribution was quantified, and the results are presented in Table 2.3. First, the simulation results before equalization from Table 2.3 agree with the measurements of the fields before equalization in Table 2.2. Also, Table 2.3 illustrates that the contribution of the non-equal element amplitude outputs has the largest error contribution of 6.3% at $M = 0$, then it steadies at larger M values to around 4%. Conversely, the phase error contribution increases with larger M, since at higher M the increment change in phase delay between elements to produce a specific vortex beam approaches the inherent phase errors of the array elements.

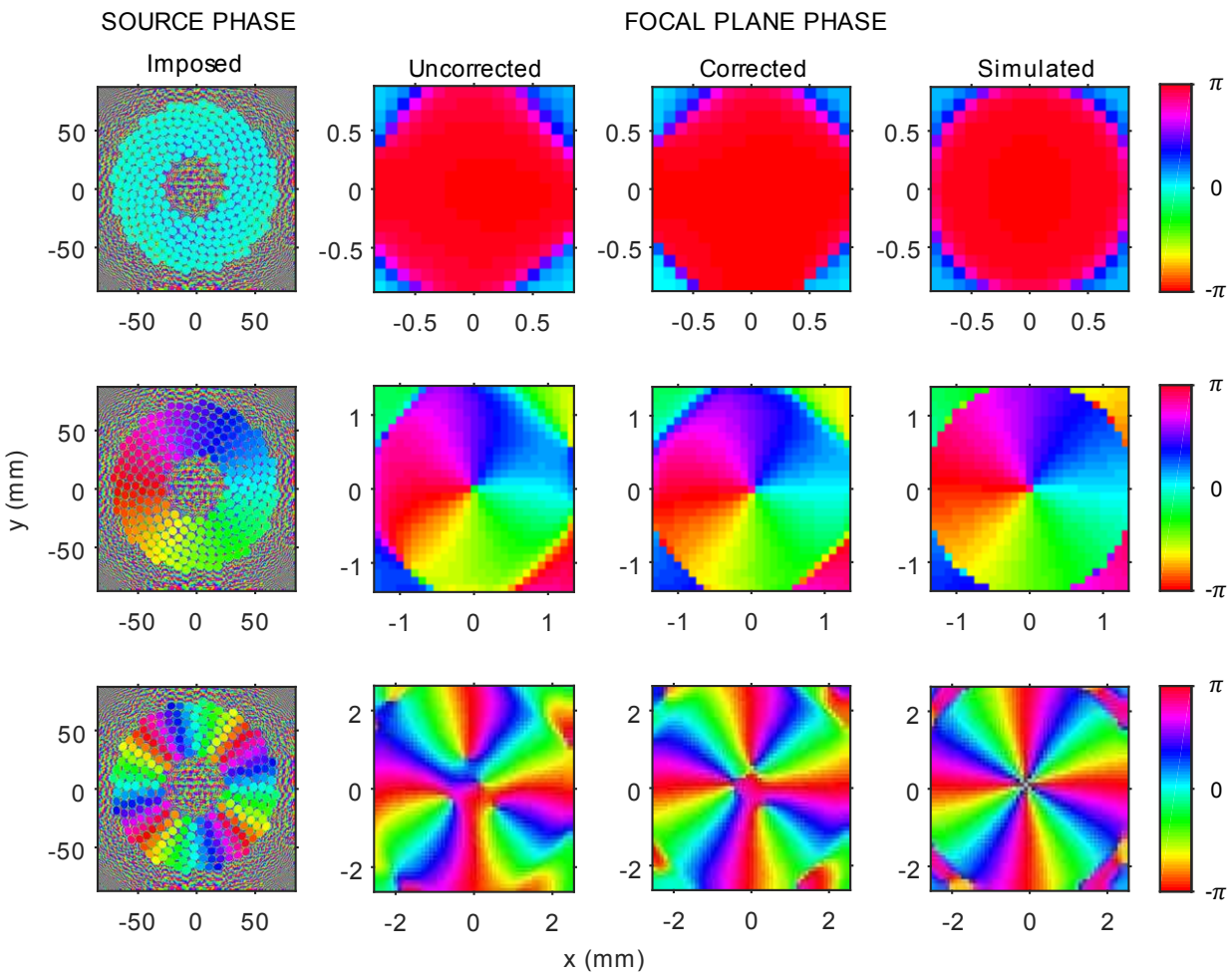

Figure 2.10: Phase distribution of vortex beams (radians). Left to right) imposed phase distribution on the array's discrete elements, measured phase distribution at the focal plane before and after applying phase corrections, and simulation for (top to bottom) M = 0, 1, and 4. Before applying phase corrections, there are slight variations in the phase distribution along the radial direction. The smooth phase transition indicates that the array behaves as a continuous acoustic source (© 2018 IEEE).

2.4 Discussion

In this study, a HIFU transducer was characterized using two well-known methods, holography and element-by-element measurements. Both approaches were used to estimate the complex pressure and normal velocity of each element, including both amplitude and phase. These characterization measurements were then used to modify how each element was driven in order to

equalize element outputs. The performance of equalization based on both holography and element-by-element measurements was evaluated by generating vortex beams and comparing the resulting intensity distributions with simulations representing an idealized array.

Measurements of vortex beams show that equalization of element outputs improved beam uniformity for all shapes, except for the focused case of element-by-element even though it produced more circular intensity distribution than before. While comparison of phase distributions suggests excellent uniformity across all array elements, some nonuniformities in measured beams are still evident, which may be attributable to various sources including discretization error in the VDAS apodization routine, which was estimated to contribute less than 1.9% change in the pressure field. This effect could potentially be improved or eliminated by electronically matching each element separately; however, as a practical tradeoff we did not pursue this level of complexity.

In general, 2D scans of acoustic beams from the element-by-element method exhibit greater non-uniformity and different intensity distribution than those from holography. There are two factors causing this additional non-uniformity. First, element-by-element measurements are taken at the focus, and unlike holography, these measurements do not characterize the surface vibration profile and instead record a far-field approximation of the effective pressure amplitude on the element. Second, electrical variability was present in the VDAS driving system. In our configuration, it was measured that the VDAS will deliver when all elements are operating simultaneously 84% of the voltage compared to when a single element is driven. Furthermore, because of the power drainage behavior of the capacitors in the VDAS and transient response of the external power source used, the output response among the elements, when firing one element at a time, can vary if they are driven one after another at a high pulse frequency rate. Therefore,

in the element-by-element experiment, the elements were triggered at 1-Hz frequency to allow the power source to recover between pules and eliminate this variability when measuring and recording the relative amplitude information. Conversely, if all elements are triggered simultaneously, the total output of the array can change based on the pulse rate frequency; however, the output of the elements relative to one another is steady. Thus, the holography 2D scan in this situation was necessary to capture the actual operating conditions and eliminate this additional electrical variability.

A 2D holography scan has many advantages over element-by-element measurements, such as, characterizing the acoustic output of all elements synchronously, obtaining the surface boundary conditions, which can be used to produce any arbitrary 2D field shape and capturing other details about the array geometry, layout, and imperfections. However, there were several limitations in the 2D holography scan that were not addressed in the analysis presented. The scan lasted for several hours over which the water temperature changes, thus leading to a change in the acoustic properties of the medium, hydrophone sensitivity response and heating of electrical components. During our scan, the temperature changes in water were limited to 1-2 ^{o}C. Furthermore, even though the misalignment of coordinates was corrected for, non-orthogonality between the mechanical axes can contribute to holographic reconstruction errors. These errors are additional contributing factors to the presence of non-uniformity in the distribution after equalization. Reference [57] presents a detailed discussion of the contribution of each source of error to the reconstruction results.

Although known and required in standards [70], the hydrophone directivity had a significant effect on the power measurements. Therefore, a curve fit using the directivity of a source radiating in free space [66] was performed on the directivity results and yielded an effective element size of

510 μm, which is over twice the nominal size of 200 μm. For element-by-element measurements, accounting for directivity increased the power from 72.5W to 91.4W, a 26.1% increase; for holography measurements, consideration of directivity increased power from 245.8W to 308.9W, a 25.7% increase. Furthermore, even though we measured the directivity up to 40^{o} and the hydrophone reached a maximum angle of 50^{o} during the scan, it was shown that maximum possible power contribution with the most conservative comparison is 1%, leading to the conclusion that for such a focused array majority of the acoustic power lies within the aperture angle of the array.

2.5 CONCLUSION

A 256-element array system was characterized in this study. Element outputs were equalized and the ability to generate uniform vortex beams that potentially could be used for the acoustic manipulation of kidney stones was demonstrated. The acoustic output of the phased array was successfully characterized by performing element-by-element and holography measurements. The element-by-element method was used to find the effective pressure amplitude and relative phase delay of each array element. For the first time to our knowledge, each element's output was localized in a holographic reconstruction at the transducer's surface, with the corresponding power attributed to localized elements equal to 97.5% of the total radiated power. The output was successfully equalized to produce uniform vortex beams in the focal plane. Measurements of uniformity of the beam intensity distribution showed that equalization based on holography surpassed that based on element-by-element measurements. While some non-ideal behavior persisted, the system was sufficient to accurately produce vortex beams. This method paves the way for future synthesis of more complex two-dimensional beams for acoustic manipulation

2.6 COPYRIGHTS

"© 2018 IEEE. Reprinted, with permission, from [M. A. Ghanem, A. D. Maxwell, W. Kreider, B. W. Cunitz, V. A. Khokhlova, O. A. Sapozhnikov, and M. R. Bailey, "Field Characterization and Compensation of Vibrational Nonuniformity for a 256-Element Focused Ultrasound Phased Array," *IEEE Trans. Ultrason. Ferroelectr. Freq. Control*, vol. 65, no. 9, pp. 1618–1630, 2018.]"

"In reference to IEEE copyrighted material which is used with permission in this thesis, the IEEE does not endorse any of the University of Washington's products or services. Internal or personal use of this material is permitted. If interested in reprinting/republishing IEEE copyrighted material for advertising or promotional purposes or for creating new collective works for resale or redistribution, please go to http://www.ieee.org/publications_standards/publications/rights/rights_link.html to learn how to obtain a License from RightsLink. If applicable, University Microfilms and/or ProQuest Library, or the Archives of Canada may supply single copies of the dissertation.".

Ch 3: MEASUREMENT OF LATERAL TRAPPING FORCE OF FOCUSED ACOUSTIC BEAMS GENERATED BY 2D ARRAY

3.1 INTRODUCTION

Acoustic waves can produce radiation forces in multiple directions relative to the propagation axis[3], enabling them to push [32],[33], trap [17],[39] and even pull [27], [39], [40]. Acoustic radiation forces allow great flexibility and can be achieved in any medium, such as air [9],[35] and water [71],[11]; and have a wide variety of application, such as, cell patterning [72], manufacturing of microchips [73], and targeted drug delivery [74]. However, most of the acoustic tweezers that have been developed are for small objects with low density or for the two-dimensional stable trapping only of large objects with low-density in air. There is an absence of research on the experimental stable acoustic trapping and manipulation of large dense objects in water. And these forces have not be quantified experimentally and only recently has a numerical model been developed to calculate the forces.

Previous acoustic traps used two opposing transducers facing each other or a single transducer with a reflective surface of the acoustic waves to create standing waves and trap particles at specific pressure node locations [15]. In other configurations, four arrays surrounding and object from all four sides were used to achieve three-dimensional manipulation [16]. Furthermore, single sided trapping has been achieved with the use of complex multi-element phased array. Similar to the multi-sided trapping, single-sided trapping and manipulation is achieved only for low-density and small particles. These two-dimensional arrays can laterally trap, levitate and pull particles [10], [11]. In addition, pulling forces towards an array was achieved by making a unique target object and measured on triangular hollow prism [27]. Vortex beams are the most common in the trapping

[17], [39] and pulling [11], [40] of small particles. Acoustic radiation force from vortex beams were used to trap and translate polystyrene objects in air [55] , and in [10] a twin and a bottle beam traps to steer with the latter beam's ability to pull as well. However, the achievement of these traps has been limited to Rayleigh particles that are smaller than the acoustic wavelength.

Recent progress has been made in the stable trapping of large objects with low density in air. For instance a large polystyrene sphere was successfully trapped and levitated in air by three-element array using the standing wave created between the sphere and the array transducers [25]. Most recently, the stable trapping from traveling waves in air by vortex beams of large object with low density was demonstrated [26]. In water, a multi-element array source was used to measure the negative radiation forces on triangular hollow prism [27] without any trapping or steering capabilities. The prism was designed such that the wavefronts will reflect from its sides, since they are much larger than the wavelength, resulting in forward scattering and negative forces. Therefore, the controlled, two-dimensional stable trapping and steering of large heavy objects in water with the use of single-sided multi-element array is necessary in the development of acoustic tweezers to be a leading technology in non-invasive treatment of the removal of kidney stones. It simply is not known what these lateral forces are relative to the acoustic intensity, gravity, and the axial force. This is a first effort to quantify the forces experimentally and numerically for a range of beams and elastic spheres.

Here we used a two-dimensional 256-element array source [75] to successfully trap and measure the lateral acoustic radiation force [76] on a wide range of large heavy objects with varying material and size. And we calculate the radiation forces of different beams on large spheres with different elastic properties and sizes. Furthermore, dynamic steering of the object was achieved by superimposing the phase delay of each location to the trapping beams. Single-sided

trapping was achieved by three beams, vortex beams which carry an angular momentum component [77]–[81] and two radially-varying phase beams. All beams were synthesized by imposing phase delays on the array elements. For vortex beams array phase is merely a function of the topological charge (M) [36], [37], we demonstrated that the radially-varying phase beams can be produced by an iterative angular spectrum approach [82], [83] to achieve a desired focal amplitude by optimizing the complex pressure distribution in a plane close to the array aperture from which the average phase on each element is found though backpropagation [57].

These traps were used to trap and measure the lateral acoustic force on large heavy spherical targets. Comparison between theory and measurement was performed and various parameters were examined to quantify the most efficient lateral trapping for given target relative to the acoustic beam.

3.2 MEASUREMENT AND SIMULATION OF FORCES

3.2.1 *Methods*

We measured the trapping lateral force of three different acoustic beam shapes by trapping spherical beads of various sizes and materials in the transverse acoustic focal plane. The first trapping beam used vortex beams with varying topological charges (*M*) for different target sizes. We synthesized two additional beams similar in the focal plane to the shape of vortex beams, Figure 3.1. The second and third beams were synthesized using an iterative angular spectrum approach [82] where the desired beam shape was imposed in the transverse focal plane and the complex pressure field close to the array aperture was iteratively solved for until convergence, then the average complex vibration of each element array was found from backpropagation from that plane. Due to the division of the array surface to discrete elements, the averaged phase over the element area does not produce the exact desired field shape as would be the case for a

continuous source. Both beams have their phase changes along the radial direction rather unlike vortex beams where the phase varies circumferentially. The beam shown in the second row of Figure 3.1 has a single π shift along the radial direction and will be referred to in the text as π-radial beam. Similarly, following a line drawn along the radial direction of the source phase of the beam in the third row of Figure 3.1, the phase varies from negative to positive and back to negative phase resulting in a total of 2π shift, so the beam will be referred to as 2π-radial beam.

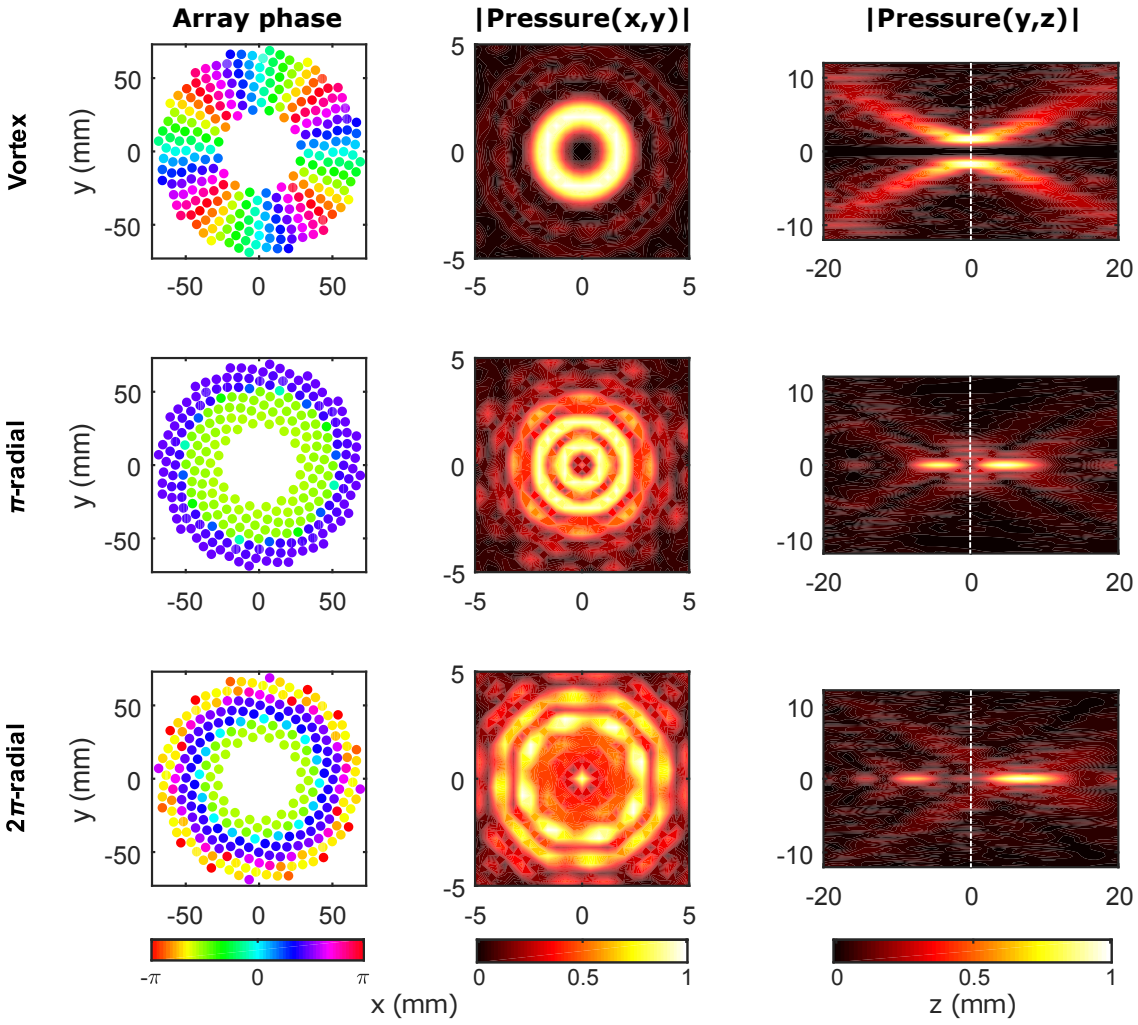

Figure 3.1: Three acoustic beam shapes used for trapping spherical beads, vortex, π-radial and 2π-radial beams from (top to bottom). A vortex beam of $M = 4$ vortex is shown here for illustration. The array phase (right column) of a vortex beam has circumferential varying phase, while for the π-radial and 3π-radial the phase varies along the radial direction. The normalized focal pressure (center column) and axial pressure (right column) distribution in the *xy*-plane and *yz*-plane, respectively, are shown for each case. Note that for the π-radial that the phase distribution on the

array is similar to that of two focused pistons with π-phase shift, thus producing the focal pressure with a null in the center, the 2π-radial has similar distribution.

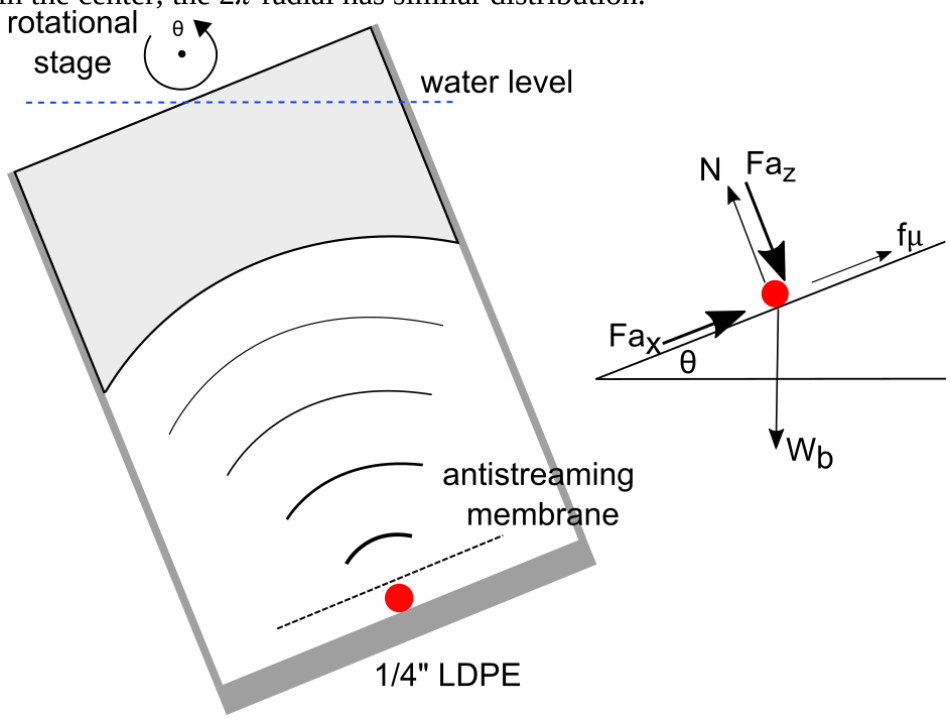

Figure 3.2: Experimental setup (right) showing the frame-array combination rotation until the spherical bead rolls off indicating the maximum trapping angle. Free body diagram (left side) showing the static equilibrium equation, in the absence of hydrodynamic forces, used to calculate the trapping force.

The strength of the lateral trapping was measured by mounting a 3D frame to the back of the 256-element array, both attached to a rotational stage and submerged under water. The frame-array combination was rotated slowly, less than 4mm/s to minimize hydrodynamic effects, until the target falls from the trap and the trapping angle (θ_{tr}) was recorded, Figure 3.2. As the rotation about the *y*-axis increases, the spherical target rolls off from the center of the acoustic trap to one side, thus changing the lateral trapping *x*-component of the radiation force, $Fa_x(x,0)$, and axial vertical *z*-component of the radiation force, $Fa_z(x,0)$, until the gravitational force overcomes the lateral trapping force. This marks the strength of the lateral trapping force and is governed by the following:

$$Fa_x = W_b \times (\sin\theta_{tr} - \mu\cos\theta_{tr}) - \mu Fa_z, \tag{3.1}$$

where W_b is the buoyant weight of the target, μ is static friction coefficient and Fa_i is the i component of the acoustic radiation force. In Figure 3.3, the left column shows the x-component trapping acoustic force, $F_x(x,y)$, for a 4-mm spherical glass bead located in the xy-plane for the different beam cases used. The right column represents the relative normalized acoustic force components (Fa_i) along the x-axis with the open dot representing stable trapping where we can increase the rotational angle and the bead will be pushed toward the origin after any perturbation in its location, while the dark dot represents unstable or the maximum trapping at which any increase in θ, the bead will fall from the trap. In Eq.(3.1), we see a contribution from the axial acoustic force, Fa_z, to the trapping force, Fa_x. As the bead rolls off to one side of the acoustic ring with an increase in θ, more of its area comes directly under the axial acoustic force component, which leads to change in friction. However, the Fa_z component was difficult to directly measure, therefore, a first order correction was applied with the assumption that the measured trapping angle along the x-axis occurred at the location of the maximum trapping lateral force, Fa_x, (dark dot of right column of Figure 3.3). At this location, Fa_z was found from simulation then scaled to match the applied acoustic power. The linearly proportional relation between acoustic force and power used in scaling the power was confirmed and tested (see Section3.3).

The theoretical model of Ref [76] was used in the simulation of the radiation acoustic forces. In Ref [76], a general expression for the calculation of the acoustic radiation forces on an elastic sphere of any size placed anywhere in an arbitrary pressure field was presented. In summary, Ref [76] calculates the acoustic radiation force using an angular spectrum approach decomposition where the force is the sum of the contribution of all plane waves at different angles of propagation. In this work, the theoretical maximum trapping angle used for comparison with the measured angle was defined as the intersection of the left side of Eq.(3.1) from theoretical predictions with the

right side of the same equation, where Fa_z was also found from theory at the location of maximum trapping.

We must note that due to the corkscrew dislocation [36], [38], [67], [84] of the wavefronts of vortex beams, an angular momentum component is associated with their propagation [38], [79], [85]–[88]. The trapping of objects much larger than the wavelength is a result of the momentum conservation from the higher order scattering terms rather than the trapping of the objects due to the convergent gradient forces [22], the resulting the angular momentum can cause rotational instabilities leading to the ejection of targets from the trap. Figure 3.4 shows the *x*-component radiation force of a vortex with M = 7 and -7 on a 4-mm glass bead located in the *xy*-plane, from which we can conclude that for instance, any perturbation from the origin location along the *x*-axis, a transverse *y*-component of force will eject the bead from the

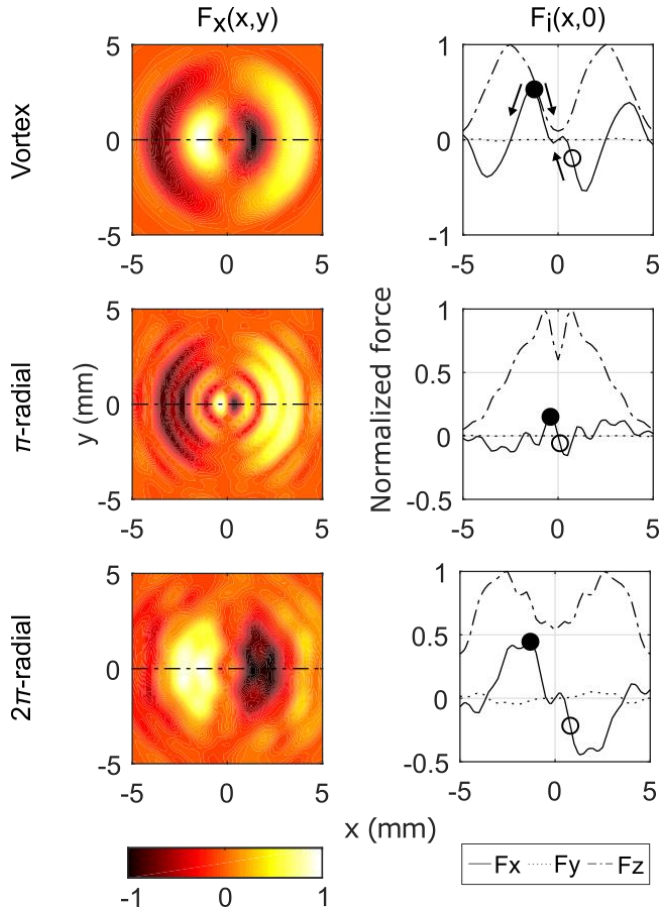

Figure 3.3: Simulation of the *x*-component of the acoustic radiation force on a 4-mm glass bead located in the *xy*-plane based on the model of Ref [76] (left column). The top right shows the average *x*-component of the acoustic radiation force for a vortex beam with M = 7 & -7. Right column displays the normalized acoustic force components along the *x*-axis (the dashed line of the left column). The open dot represents a stable tapping point where the bead will restored to the origin, while the dark dot represents the location of the maximum trapping force where the maximum trapping angle (θ_{tr}) is recorded and at which the axial acoustic force component is used to account for the frictional acoustic component ($\mu F a_z$) in Eq.(3.1).

trap. Furthermore, the different signs result on the radiation force field is seen by their opposite directionality. Since the force and torque are an average-time result of the pressure field, the angular momentum is controlled by the helicity of the vortex beams. By sending two equal consecutive pulses of M having opposite sings [89], [90], a zero net torque was achieved [26] resulting in a two-dimensional tweezer-shaped force field, Figure 3.4. The top row of Figure 3.3 is a representation of the acoustic force produced by a vortex beam of M = |7|, where the absolute value from here on denotes the average force produced from of two vortex beams with M = ±7. Conversely, the π-radial and 2π-radial beams were synthesized with goal to have trapping rings that do not carry an angular momentum component as can be seen from the radially-varying phase used for their synthesis, right column of Figure 3.1. Table 3.1 presents a summary of the different bead materials and beam shapes used for trapping each bead.

Table 3.1: Different spherical beads sizes and materials and the beam shapes used in trapping.

Material	Glass					brass & ceramic
Diameter (mm)	2	3	4	5	6	4.8
Beam shape	vortex (M = |2| & |3|) & π-radial	vortex (M = |3| & |4|)	vortex (M = |4| & |5|) & 2π-radial	vortex (M = |5| & |6|) & 2π-radial	vortex (M = |6| & |7|)	vortex (M = |4| & |5|)

In the setup, targets were held on a ¼" low density polyethylene (LDPE) material having low power reflection coefficient in water, less than 1% in order to eliminate interference with the incident acoustic beam (Appendix 3.7.1). The static friction coefficient of different bead materials

against LDPE was measured by recording the maximum angle at which the bead rolls off without any acoustic exposure, since $\mu = \tan\theta$. The static friction coefficient was measured to be 0.059, 0.030 and 0.022 for glass, ceramic and brass spheres, respectively. Furthermore, low voltage amplitude was used to eliminate any nonlinear acoustic effects and the average power was changed for different targets to ensure a large enough measurable angle was reached by changing the pulse on-time. Anti-streaming membrane was used in all measurements to verify the assumption that acoustic streaming is negligible at such low amplitudes.

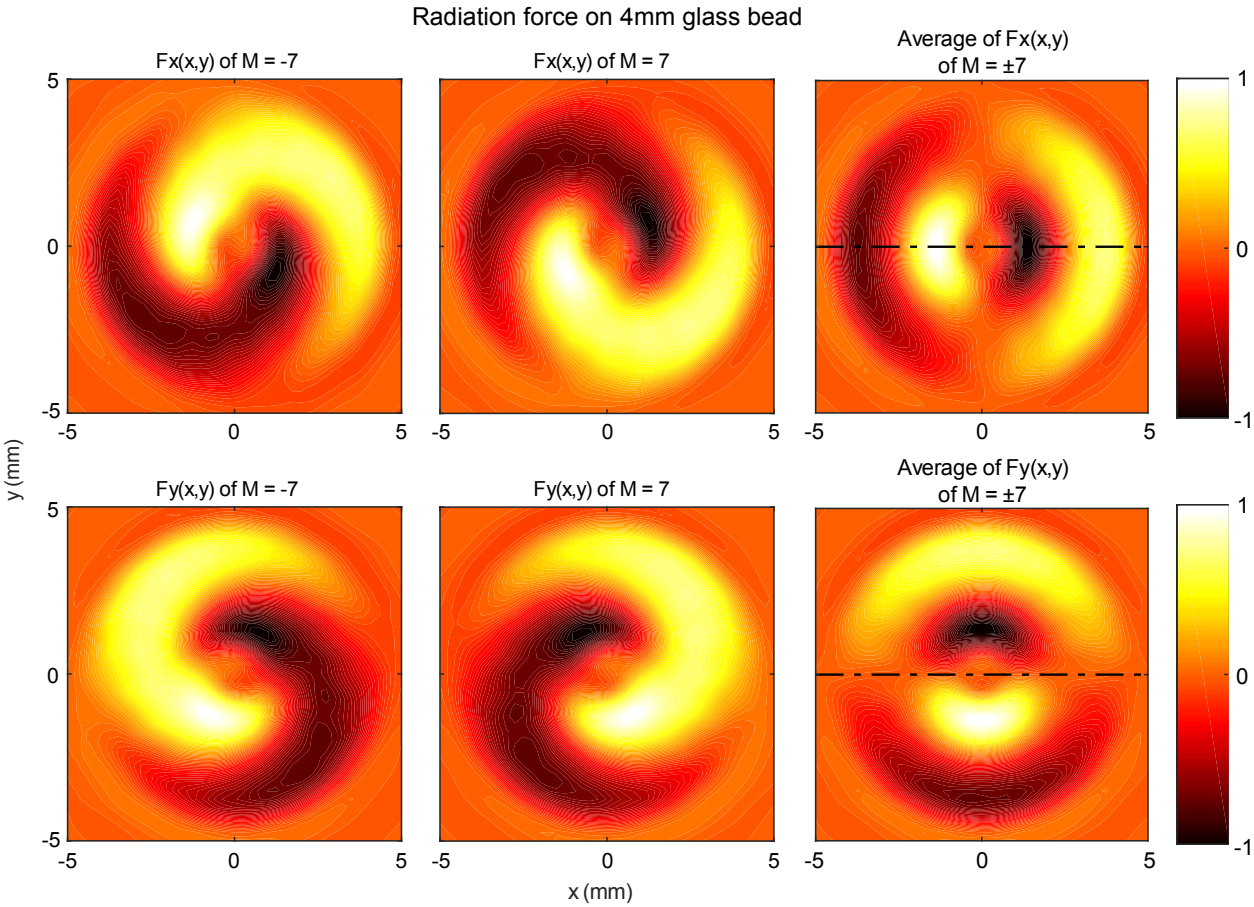

Figure 3.4: The *x*-component (top) and *y*-component (bottom) of the acoustic radiation force of an *M* = -7 (left), *M* = 7 (center) and the average of *M* = 7 and -7 or as referred to in the text as *M* = |7| (right) on a 4-mm glass bead in the *xy*-plane. Any perturbation in the bead location from the origin results in a transverse force component effectively ejecting it from the trap. The net average radiation force of sending a positive and negative *M* results in stable trapping.

3.2.2 *Results and discussion of measurement of forces*

Measurements of the maximum trapping angle (θ_{tr}) are compared against the theoretical values for the different bead materials and sizes under different acoustic beams. Good agreement between experimental and theoretical values was shown for the forces on various target sizes and elastic properties. Figure 3.5 shows comparison between measurements and theoretical predictions plotted vs the ratio of the bead diameter to the beam width (η), where the beam width was defined as the distance between the maxima of one-dimensional cut along the diameter of the two-dimensional intensity distribution of the trapping acoustic beam. We demonstrated the successful trapping of wide range of beads material and sizes. Furthermore, we successfully trapped beads that are 40% larger than the acoustic beam, η = 1.4.

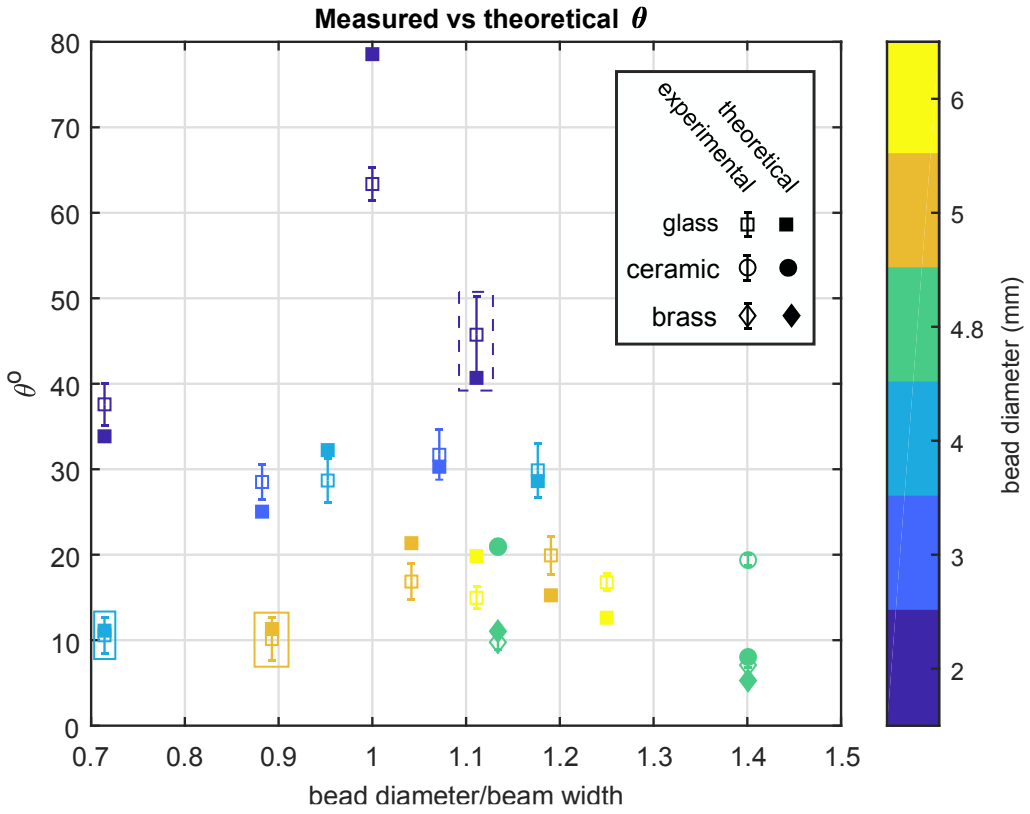

Figure 3.5: Comparison between measured and theoretical trapping angle (θ_{tr}) vs. the ratio of bead diameter to beam width (η).Close proximity of solid and open marks shows the good agreement between measurements and theory over a range of bead sizes compositions. Different materials

are denoted by different data point shapes, while dark and open data points represent theoretical and measured values, respectively. Data point pairs in dashed and solid rectangle are for π-radial and 2π-radial, respectively.

Figure 3.6 presents the absolute relative error in θ_{tr} vs η. We note that the error increases with increasing η, as an increasing η corresponds to a narrower beam with respect to the bead diameter, and such narrow beams result in a greater axial acoustic component, Fa_z. Thus, we investigated the trend between the error and the ratio of the lateral to the axial acoustic force components (Fa_x/Fa_z). It was found from measurements that a much narrower beam than the bead diameter will cause an increase to the axial acoustic force, Fa_z, relative to the trapping acoustic force, Fa_x, which will result in a larger error. Thus, it is confirmed that the error increases with smaller ratio of the lateral trapping to the axial acoustic force components, Figure 3.7.) Overall, the average absolute error of the measurements is 15%, excluding a single measurement point of the ceramic bead at η = 1.4. For that measurement, we are not certain for the specific reason for such large error. However, the large η or narrow beam resulting in a large Fa_z is a contributing factor and it also may be due to the possibility of irregularities on the LDPE sheet used, which may have contributed to the accuracy of measurement of the trapping angle.

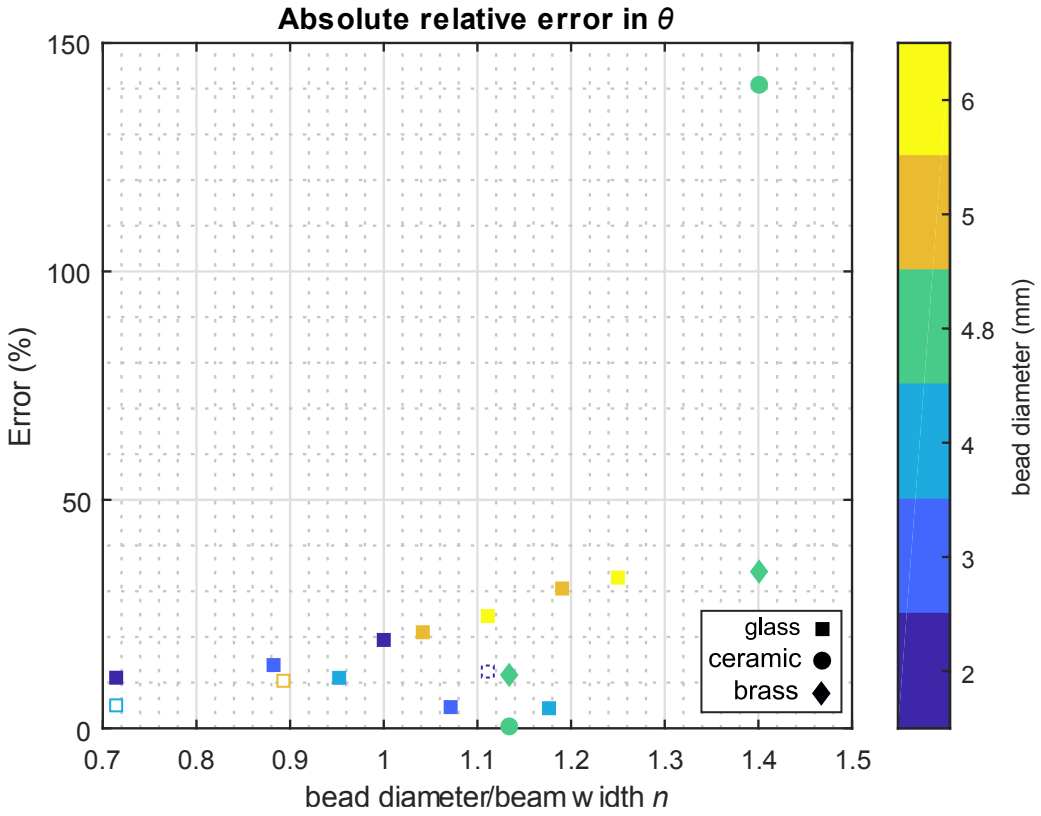

Figure 3.6: Absolute relative error in the maximum trapping angle (θtr) vs. the ratio of bead diameter to beam width (η) for different beads material and a wide range of diameters. Dotted open and solid open squares are for beads trapped by π-radial and 2π-radial acoustic beams, respectively.

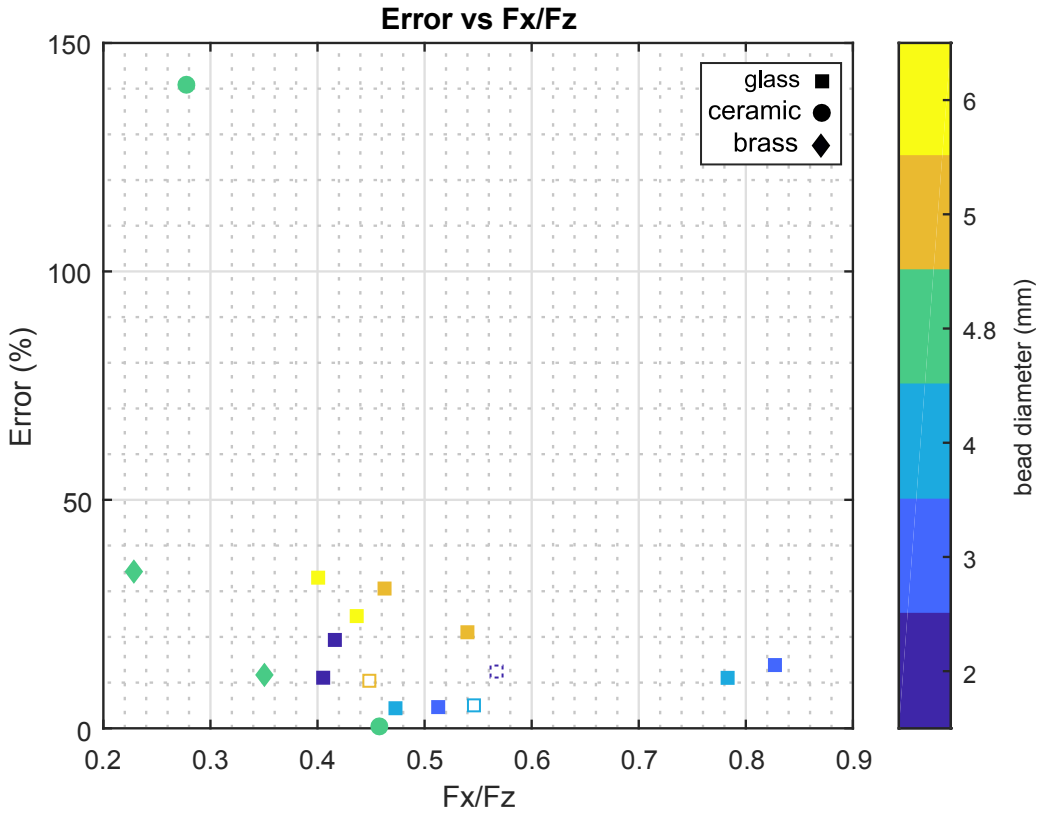

Figure 3.7: Absolute relative error in θ_{tr} vs the ratio of the trapping to axial acoustic force, Fa_x/Fa_z, which corresponds to a large bead to beam width ratio, η. A correlation between increase in the ratio of Fa_z component relative to the Fa_x component and the absolute relative error increase confirming the relationship between η and Fa_z, and the contribution of Fa_z to the introduction of errors in the measurements. Dotted open and solid open squares are for beads trapped by π-radial and 2π-radial acoustic beams, respectively.

We measured the relationship between theoretical trapping forces of various vortex beams over a specific target diameter, such that the trapping force is a function of M, $Fa_x = f(M)$. This was done by choosing a specific bead size and material, then we extracted the trapping force as M varies. The results are shown in Figure 3.8 using the non-dimensional y-axis equal to the ratio of the trapping force in a 10-watt vortex beam to the weight of each specific bead material and size vs η. The experimental trapping forces were scaled using the acoustic power ratio of the 10-watt to the power of the experimental beam. In Figure 3.8, we observe that the maximum trapping to weight ratio occurs at η values close to 1, regardless of the bead material. This can be explained by the fact that close to $\eta = 1$, the area of the bead under the acoustic pressure is equal to the active

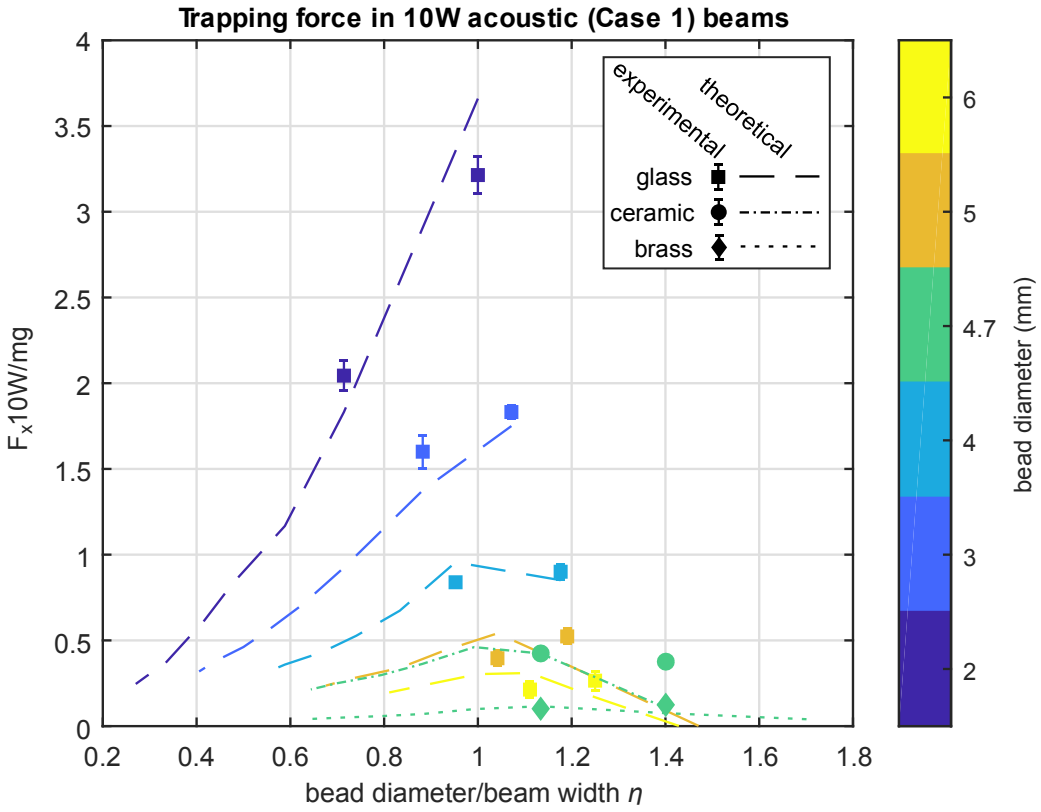

Figure 3.8: The maximum trapping lateral force in 10-watt acoustic beam normalized with respect to target's weight plotted vs the bead diameter to beam width (η). Theoretical lines are not continuous as they represent the trapping at vortex *M* for a specific bead size and material, since each M has defined beam width rather than a smooth continuous range. Regardless of the bead material, the most efficient trapping occurs at η close to 1.

area of the acoustic pressure applied by the beam leading to the most efficient trapping. For instance, in Figure 3.8, for a 2-mm glass bead at η = 1 and 0.71, the beams can trap 3.25 and 1.83 times the weight of the bead (13 mg), respectively; and for a 6-mm glass bead at η = 1.1 and 1.3, the beams can trap 0.31 and 0.17 times the weight of the bead (284 mg), respectively. The significance of Figure 3.8 is that for specific bead size, one can choose the most efficient beam for trapping regardless of the target material.

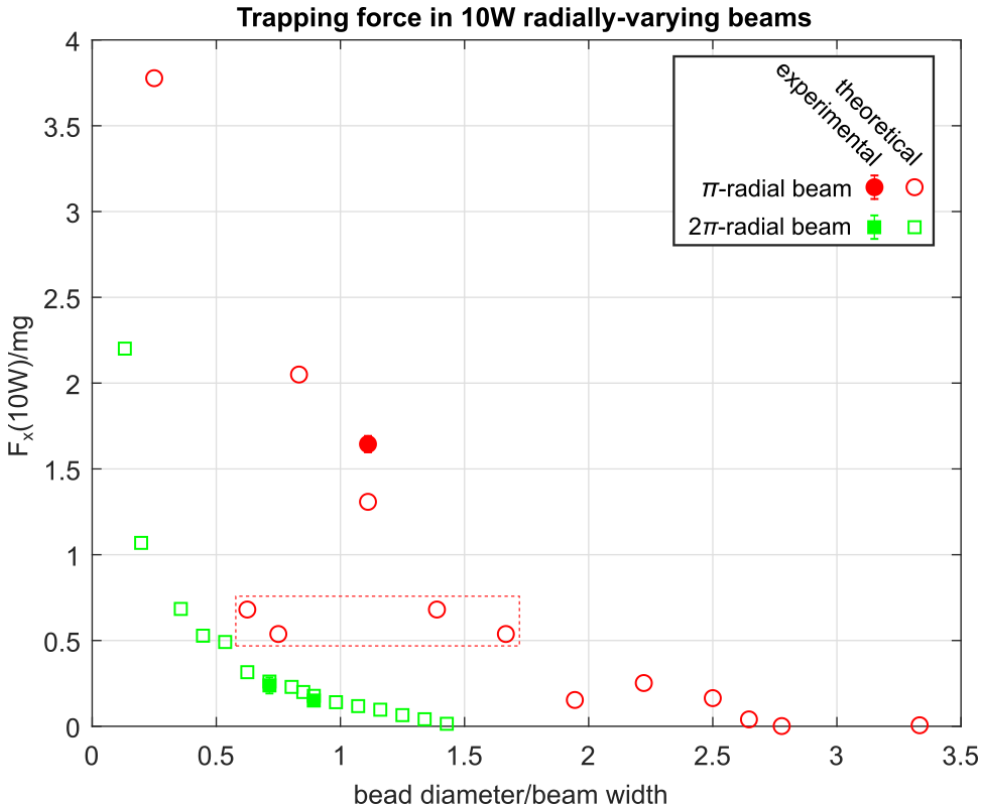

Figure 3.9: The maximum lateral trapping force in a 10-watt acoustic beam normalized to the bead's weight shown vs the ratio of the bead diameter to beam width. The normalization of the data points to the weight results in a proportional trend to the reciprocal of the bead volume, i.e. a cubic term. The dotted rectangle borders a pair of beads that are trapped due to the contribution of both acoustic rings of π-radial beam.

In a similar manner of quantifying the ratio of the trapping lateral force to the weight over various M's of vortex beams, the analysis was carried for π-radial and 2π-radial beams. However, for the analysis of these beams, the bead diameter of a specific material was varied for each radially-varying phase beam, since these beams have fixed acoustic ring diameters unlike vortex beams. Unlike the trend shown in Figure 3.8 of vortex beams, the radially-varying phase beams inhibit a cubic trend for each beam, Figure 3.9. The radiation force is large for very small spheres; however, the dominant behavior is a result of the normalization to the weight of the sphere which is inversely proportional to the bead volume (i.e. the cubic power of the radius, $1/r^3$). Another interesting aspect of Figure 3.9 is the existence of multiple trapping locations for specific targets

in the π-radial beam. The pair of points shown in dotted rectangle are for 2.5 and 3-mm glass bead that are trapped by both 1.8 and 4-mm acoustic beam rings. This behavior was confirmed by a dynamic simulation of the maximum trapping force that showed the contribution of both acoustic rings at the location of maximum trapping. Additionally, this behavior is evident for π-radial beam, since it has two acoustic rings of equal intensity, while for the 2π-radial beam, the inner ring is responsible for trapping because it has the highest acoustic intensity.

We must comment that the results shown above in Figure 3.9 for radially-varying phase beams represent the best bead size to be trapped by a specific beam, which is not a realistic scenario for acoustic tweezers applications. In an acoustic tweezers' applications, there is a target of a specific size that needs to be manipulated; however, in Figure 3.9 the target is chosen based on the synthesized beam, which is not practical. By comparing the results of vortex beams from Figure 3.8 to the those of the radially-varying phase beams in Figure 3.9 for selected tested glass beads of the same size having an η close to unity , we note that vortex beams have twice the strength of the lateral trapping to that of the π-radial beam, 3.25 and 1.65 times the weight of 2-mm glass bead, respectively; and more than double the strength of the lateral trapping to that of the 2π-radial beam, 0.40 and 0.15 times the weight of 5-mm glass bead, respectively.

3.3 EVALUATION OF ACOUSTIC POWER-FORCE LINEARITY

Acoustic radiation force is linearly proportional to the acoustic power as the well-known result of the force on a fully absorbing target, $F = W/c$ [1], where F is the acoustic force, c is the speed of sound and W is the acoustic power. To verify this linear relationship and the scaling of theoretical simulation to experimental results based on the power ratio, a 5-mm glass bead was trapped by a vortex beam having $M = |6|$, and the trapping maximum angle (θ_{tr}) was recorded as a power level sweep was performed. Then by reordering of Eq.(3.1) and defining a non-dimensional

coefficient γ_i where $\gamma i = \frac{c}{W} F_i$ is proportional to the acoustic force component F_i, Eq.(3.1) can be written as a function of the acoustic power, W and γ as follow:

$$\sin\theta - \mu\cos\theta = (\gamma_x + \mu\gamma_z) \times \frac{W}{cW_b}. \tag{3.2}$$

We note that in the setup when the acoustic power is zero, there is still a measurable angle due to friction. However, the re-arrangement of Eq.(3.1) shown will have a *y*-intercept of zero at an acoustic power of zero because of the subtraction of $\mu\cos\theta$ from the left-hand side of Eq.(3.2). Another interesting behavior of Eq.(3.2) is friction enters on both sides of the equation, in the slope of the line given by $(\gamma_x + \mu\gamma_z)$, which is the component of fiction due to the axial acoustic force, Fa_z, and in the left side of the equation which is the friction due to the buoyant weight (W_b) of the bead. The theoretical line and measured experimental points of Eq.(3.2) are plotted in Figure 3.10 along with the linear best-fit to the measured data. A closer look at the best-fi line, we note a slightly higher slope and lower y-intercept than the theoretical line, both characteristics can be contributed to a larger measured value of μ, thus proving the previous comment regarding the importance of friction on the measurements as it affects both sides of the equations. A careful examination of the experimental data points shows that the drift from theoretical line occurs at two locations low and higher power values. This can be contributed to a lack of precision of the driving electronics to transmit at the exact specified voltage, while at higher power, which is accomplished in the setup by increasing the duty cycle, there is drooping in the capacitors.

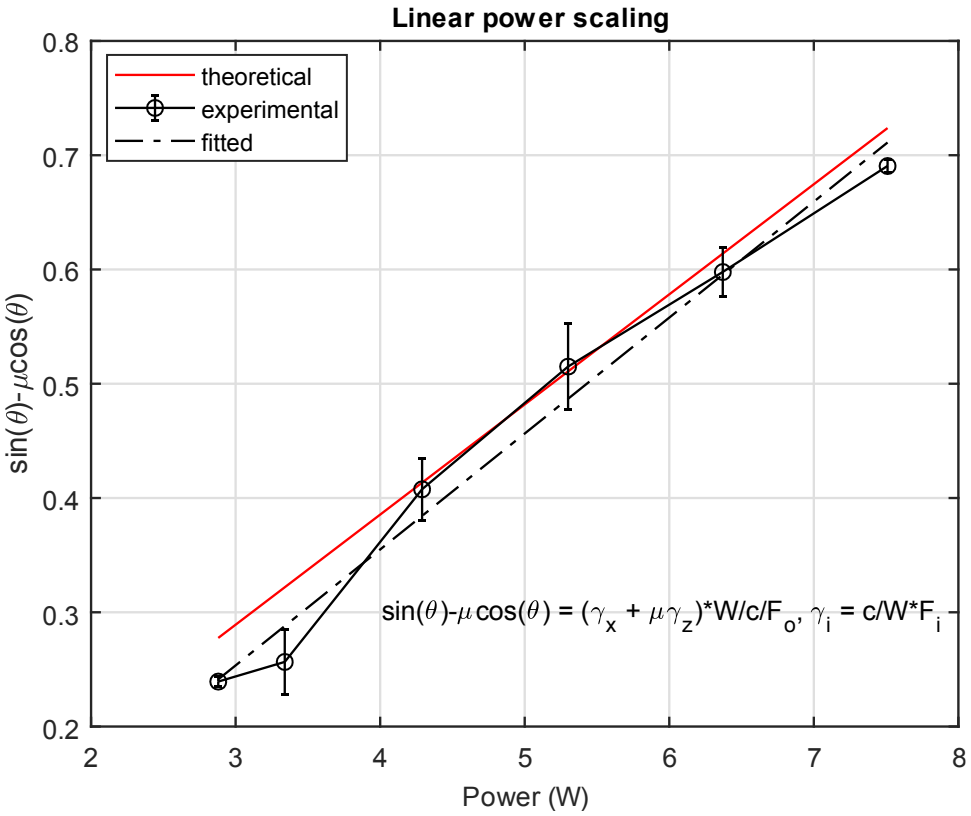

Figure 3.10: Linear relationship between the acoustic power and the acoustic radiation force. The drift between the experimental data points (open dots) and theoretical line at the beginning and the end can be a result of noise from the driving electronics at low power and drooping of the capacitors at high power, respectively. Friction affects both sides of the equation, as shown above, a larger friction coefficient results in higher slope from friction due to the axial acoustic force and smaller *y*-intercept due to friction from the buoyant weight of the bead.

3.4 EVALUATION OF STREAMING

Streaming is absorption of the wave momentum by the surrounding fluid [1]. This fluid motion can affect the stability of the target and affect the measured force. Therefore, the effect of streaming of the fluid was measured to ensure the accuracy of the force measurements. The effect of acoustic streaming was measured at low and high-power levels, as mentioned previously, the time-average power was changed by increasing the pulse on-time. A 5-mm glass bead was trapped by a vortex of $M = |6|$, then the maximum trapping angle was measured for three different configurations, no anti-streaming membrane, elevated anti-streaming membrane that lies 2 cm

above the bead and a lowered ant-streaming membrane that laid less than 1 cm above the bead. The three configurations were tested at low and high-power levels of 3.3 and 8.7 watts, respectively; however, for all measurements the voltage amplitude used was kept at 5 volts and the length of the on-time pulse is increased to reach higher power levels. Figure 3.11 shows the change in angle for each power level vs the three anti-streaming membrane configurations. It is observable that acoustic streaming at such low amplitude is of no effect on the setup.

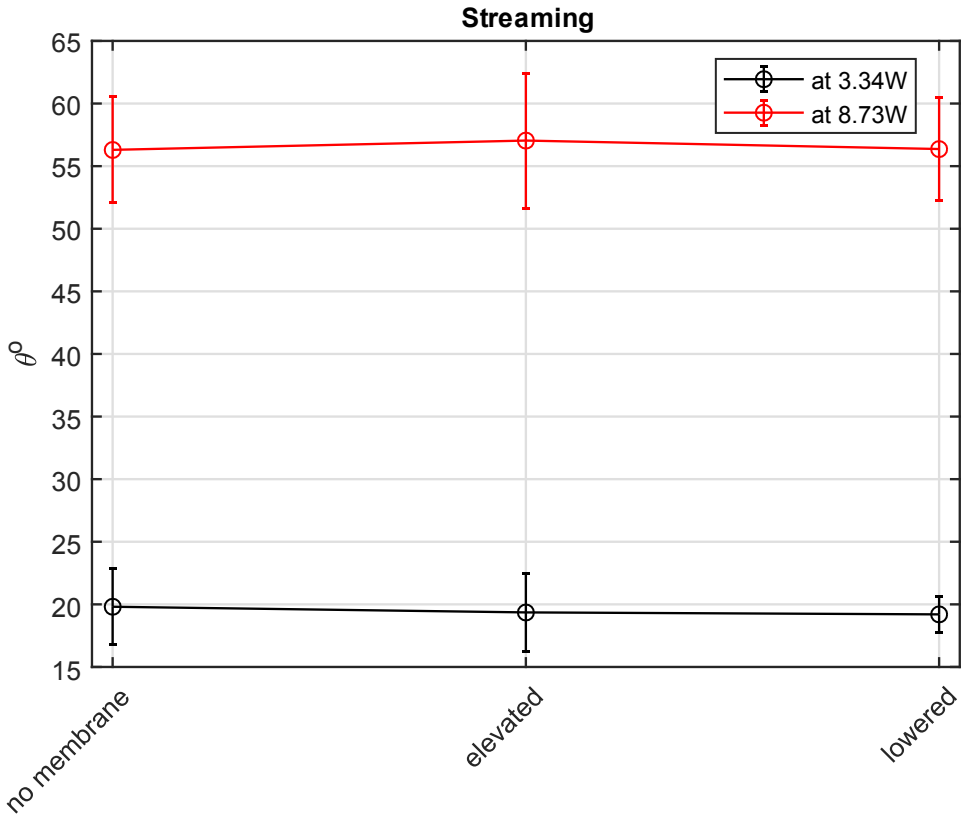

Figure 3.11: Effect of acoustic streaming on the lateral trapping force measurement at two different power levels of 3.3 and 8.7 watts vs. three different anti-streaming membrane configurations. The maximum trapping angle for a 5-mm glass bead does not vary along the x-axis for each power level demonstrating the absence of acoustic streaming effects on the measurements.

3.5 DEMONSTRATION OF MANIPULATION OF OBJECT

Stable trapping and electronic steering were demonstrated. Electronic steering of large objects is achievable as long as the lateral trapping force is larger than the other forces. Therefore, slow almost quasi-static steering of large objects will minimize the inertial and hydrodynamic force

allowing for stable steering of acoustic traps. To dynamically steer the focus along a desired path, the phase delay on element *i* is found by calculating the difference between the distance from element *i* on the array's surface and the desired location; as referenced to the geometrical focus of the array, shown by the following equation:

$$\emptyset_i = \left[R - \sum_{j=1}^{3} \sqrt{\left(x_{ij} - p_j\right)^2}\right] \times k, \tag{3.3}$$

where $\emptyset_i$ is the phase delay on element *i*, R is the radius of curvature of the array equal to 120 mm, x_{ij} is the x_j-coordinate of element *i*, p_j is the *j*-coordinate of point *p* along the desired steering path and *k* is the wave number. By superimposing the phase delay of each element used to produce a vortex *M*, calculated from Eq.(2.10), and the phase delay in Eq.(3.3) to steer the focus to a specific location, we are able to find each element's phase ($\emptyset_i$) to synthesize a specific *M* vortex beam and steer it in along a preprogrammed path as follow:

$$\emptyset_i = M \times \arctan\left({}^{x_{i2}}/_{x_{i1}}\right) + \left[R - \sum_{j=1}^{3} \sqrt{\left(x_{ij} - p_j\right)^2}\right] \times k \tag{3.4}$$

In Figure 3.12, we tested the efficacy of the dynamic steering of vortex trap on a 5-mm glass bead trapped by a beam with $M = |6|$ over a 3-leaf polar path represented by the following equation:

$$r(\varphi) = r_o \cos(3\varphi), \tag{3.5}$$

where r_o = 13 mm, r is the radial dependent variable in millimeters and φ is the angular independent variable in radians. Multiple frames of the target location are shown with tracking of the centroidal measured location with the actual theoretical path of Eq.(3.5). Precise agreement between both paths with the exception of minute deviance in the upper left leaf, most likely associated with the tilt of the camera angle.

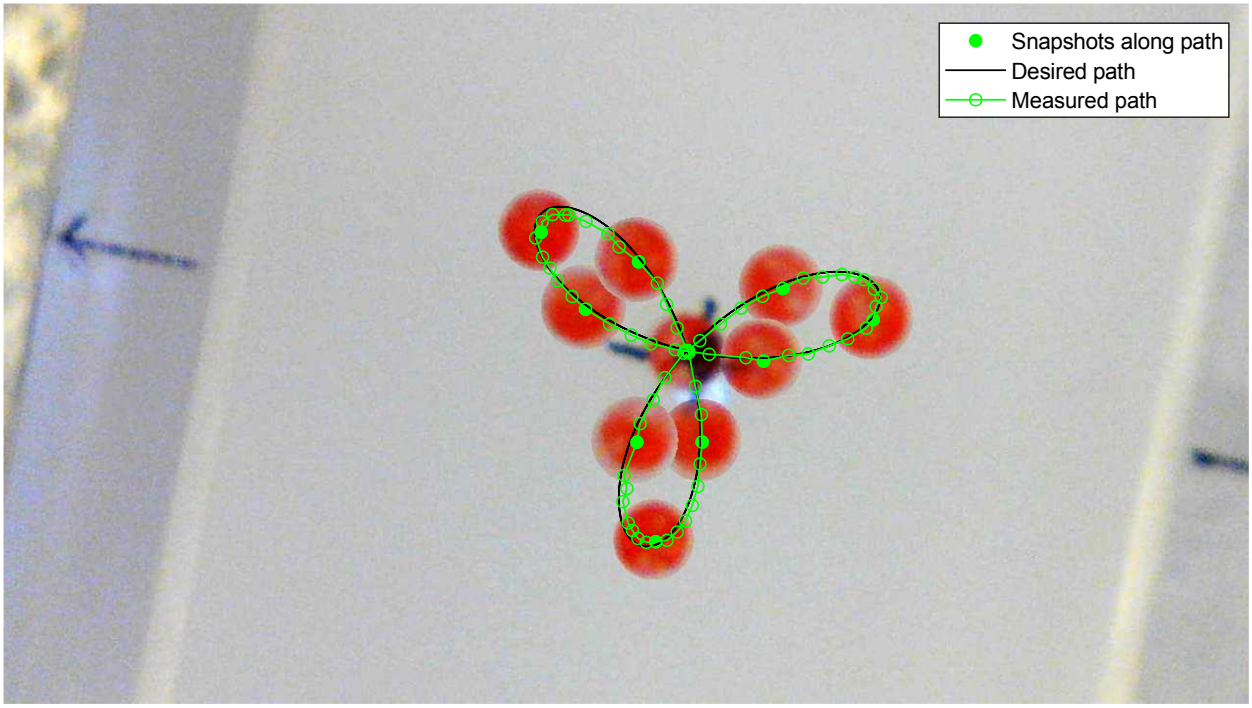

Figure 3.12: The trapping by an M = |6| and dynamic steering of a 5-mm glass bead in a path defined by Eq.(3.5). The solid green dots are the centroidal locations where snapshots of the bead were taken on the measured path of the centroid (open green dots). Good agreement is shown between the theoretical path (black line) and measured path (green dots).

3.6 CONCLUSION

A single sided 256-element array is used to trap large heavy objects varying in sizes and material. Three different beam shapes are utilized in the trapping of different spherical beads. The first was vortex beams that have zero average net torque by reversing of the sign of the topological charge enabling the stable trapping of bead diameters up to 1.4 times the beam width. Agreement between the theoretical model and measurements of the trapping lateral forces over a wide range of bead sizes and materials lies within 15% error. To our knowledge, this is the first time the lateral trapping forces are quantified and compared against the theoretical model. Furthermore, an important ratio (η) of the bead diameter to the beam width is defined, such that when η is close to 1, a vortex beam of specific topological charge (M) is chosen for efficient trapping of specific bead

size regardless of its material. The stable trapping based on the choice of (η) and two-dimensional dynamic steering of a large bead (5 times larger than the wavelength) is accomplished along a pre-specified desired path. This work lays the groundwork toward the development of acoustic tweezers for large heavy objects, one can decide the size of the beam to achieve the highest stable lateral trapping of a specific target size along any need trajectory.

3.7 APPENDIX

3.7.1 *Acoustic properties of low density polyethylene (LDPE) backing*

The acoustic properties such as impedance and speed of sound in LDPE material were measured to ensure that the reflection power coefficient was small and would have negligible effect on the acoustic incident beam in order not to affect the measurement of the trapping acoustic force. We used a 1.5-MHz 1.5-cm diameter flat source and in the far field LDPE sheet was placed with a hydrophone directly behind the sheet to eliminate any edge scattering from the sheet. Different thicknesses were tested, and the transmission coefficient was calculated from the amplitude of the transmitted wave. The transmitted wave propagates through the medium described and governed by three-medium configuration of Ref [91] and attenuated as well, as described by the following equation:

$$T = \frac{P_{transmitted}}{P_{incident}} = T_m e^{-\alpha l}, \tag{3.6}$$

where $T_m = \frac{4Z_{ldpe}\, Z_{water}}{(Z_{ldpe}+Z_{water})^2}$, Z_i is the impedance of medium i, l is the thickness of the sheet in meters (m), α is the attenuation coefficient in 1/m, and P is the pressure amplitude of transmitted or incident wave. The natural logarithm of the transmission coefficient is plotted against the

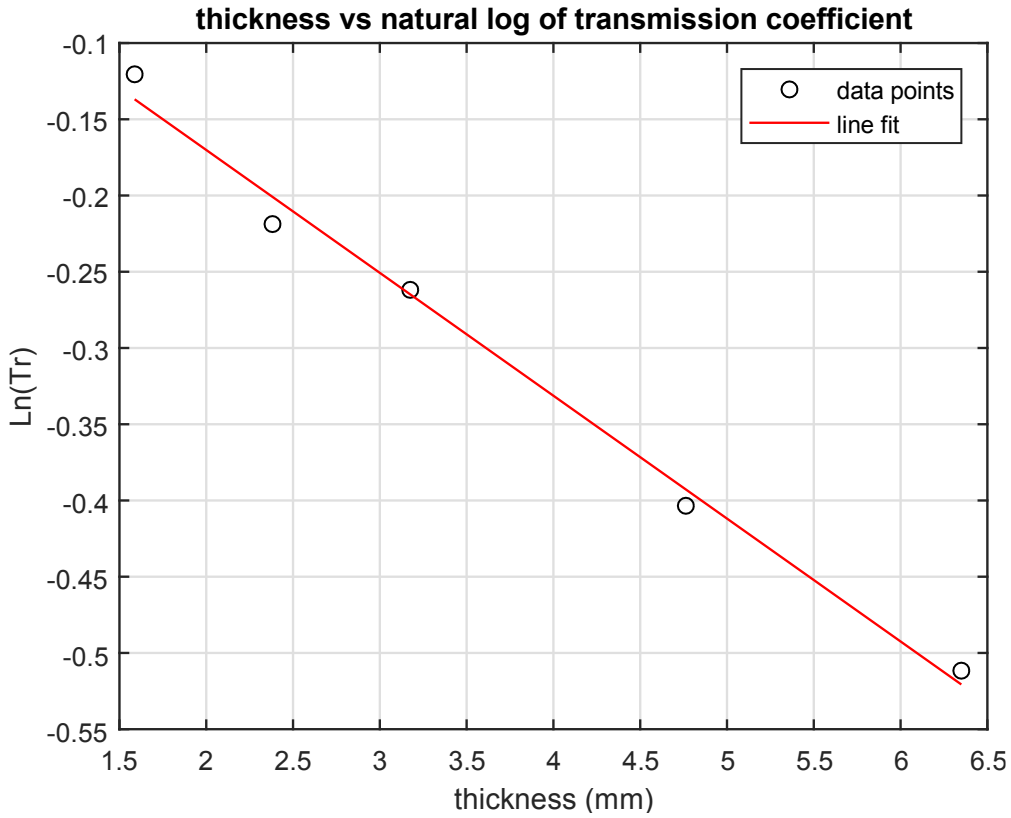

Figure 3.13: Experimental measurement of the transmitted pressure amplitude through different LDPE sheet thicknesses generated from a 1.5-MHz 1.5-cm flat source. The *y*-axis is the natural logarithm of the measured transmission coefficient and the *x*-axis is the different thicknesses tested. The *y*-intercept of the line-fit represents the attenuation coefficient (α) of the material, while the slope is equal to the natural logarithmic of *Tm* from Eq.(3.6).

thickness of the material in order to find the acoustic impedance and attenuation (α) of the LDPE material. From the *y*-intercept of Figure 3.13, α = 80.8 1/m, while the slope of the experimental line-fit is equal to Ln (T_m) from which we calculate the impedance of the LDPE to be equal to:

$$Z_{ldpe} = \frac{-\left(2-\frac{4}{T_m}\right) Z_{water} \pm \sqrt{\left(\left(2-\frac{4}{T_m}\right) Z_{water}\right)^2 - 4 * Z_{water}^2}}{2}. \quad (3.7)$$

Using the result of Eq.(3.7), the reflection power coefficient of the incident wave from the two faces of the LDPE sheet is the amplitude of the reflection coefficient calculated in a manner similar to that of Ref [91] as the following:

$$R = \frac{z_{water} - z_{ldpe}}{z_{water} + z_{ldpe}} * \left[1 - \frac{4Z_{ldpe}\, Z_{water}}{(Z_{ldpe} + Z_{water})^2} e^{2ikl}\right]. \quad (3.8)$$

From Eq.(3.8) the power reflected is calculated to 0.8% for a ¼" LDPE sheet, which results in minimal interference with the incident acoustic beam use in the lateral force measurements.

Ch 4: THREE-DIMENSIONAL MANIPULATION *IN VITRO* AND *IN VIVO*

4.1 INTRODUCTION

The manipulation of kidney stones in urinary tract or foreign objects in the body requires the development of three-dimensional acoustic manipulation. For instance, there are situations where there is a need to move an object along a complex path, both transverse and along the acoustic axis of the array. Additionally, the electronic steering is also needed because in certain cases there is a limited acoustic window for treatment because of bone structure. Therefore, beam steering is required to access and trap a target inside the body for manipulation. For such cases, the two-dimensional manipulation presented previously is ineffective. Previous three-dimensional manipulation was achieved using bottle beams that surrounded a small polystyrene particle much smaller than the wavelength in air [10]. In water, acoustic traps on polystyrene particles that were less than one tenth of the wavelength were manipulated and the forces were measured [11]. It was recently shown that success of ultrasound propulsion of kidney stones in humans [30]. However, there is a lack of the ability to manipulate large dense particles in three-dimensions. The work presented in this chapter is toward this end.

Previously, we demonstrated the successful trapping and manipulation of large heavy objects in two-dimensional space. Furthermore, we substantiated the characterization of our array and the theoretical acoustic radiation force model by yielding good agreement between theoretical and measurements of the strength of the lateral trapping force. Additionally, we introduced a geometrical ratio of the target diameter to the beam width and found that for the most efficient trapping results that ratio should be close to unity.

In this chapter, we achieve three-dimensional manipulation with the aid of gravity to dynamically steer and control large heavy spherical targets *in vitro* and *in vivo*. In the first part of this chapter, the *in vitro* experiments along with simulations were performed to choose the optimal parameters needed for the dynamic steering of three-dimensional trap *in vivo*, such as the steering range capabilities, the stability of each trap, the ability to go through tissue-mimicking aberrating layers and the power range required. First, we investigated the evolution and stability of different acoustic traps in different three-dimensional spaces to optimize the beam shape used in trapping. Second, we performed preliminary experiments to test the success of the traps in levitating, trapping and manipulating targets along three-dimensional paths. Third, phantom-mimicking gels with aberrative and attenuative properties were used to test the three-dimensional dynamic steering to estimate the power and voltage amplitudes required. In the second part of this chapter, the *in vivo* experiment on a live pig under anesthesia to manipulate a large heavy object inside the bladder is presented. First, few experimental setups were tested to find the optimal position of the pig for good coupling with the array while having a viable acoustic window. Second, imaging scripts were developed for targeting and to simultaneously observe the manipulation non-invasively. Furthermore, a borescope was used to visually observe the successful trapping and three-dimensional manipulation of a large target for the first time *in vivo*.

The three-dimensional manipulation capabilities presented here will make acoustic tweezers a reality and viable option that can be used in many applications. For our purposes, the development of acoustic tweezers will present an alternate non-invasive option for the removal of small passable kidney stones. Other medical applications include the manipulation of blood clots, removal of foreign objects and targeted drug delivery. Other potential uses include containerless transport, laboratory applications and manufacturing endowments.

4.2 THREE-DIMENSIONAL MANIPULATION *IN VITRO*

Vortex beams were used for three-dimensional manipulation of targets *in vitro* with the aid of gravity. As shown in the previous chapter, vortex beams have high lateral trapping strength in addition to an axial force component. The three-dimensional manipulation was accomplished by placing the target above the array in the focal region, while the array was facing upward, Figure 4.1. The target is trapped in the lateral directions by the acoustic ring and levitated in the axial direction while gravitational pull counters this force.

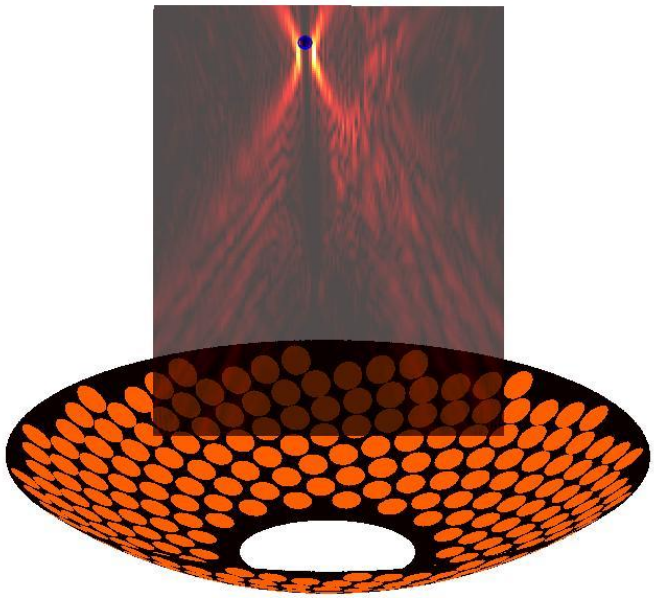

Figure 4.1: Arrangement showing the three-dimensional trapping of a spherical target (blue circle) by a vortex beam and with the aid of gravitational pull. The vortex beam stabilizes the target laterally and applies axial radiation force while gravity stabilizes the target from above. The vortex beam shown is for $M = |4|$ and the beam is steered to (3,5) mm in the *zx*-plane.

For the setup shown in Figure 4.1, we investigate the variable space to find the optimal parameters for three-dimensional manipulation. We examine and present the results of how the radiation acoustic force changes with the axial steering range of the beam and the axial steering method, and the stability of different beam shapes (topological charges) for the off-axis beam

steering. Then the results are followed by a brief a discussion leading to the demonstration of three-dimensional manipulation *in vitro* with phantom mimicking gels. Simulations of the acoustic fields in following sections were performed using Rayleigh integral method described in chapter two and simulations of the radiation acoustic force are based on Ref [76].

4.2.1 *Acoustic radiation force and axial steering of targets*

When a target is placed in the focal region of a vortex beam, the target is axially pushed or levitated until it reaches equilibrium along the *z*-axis at a location where the axial acoustic radiation force is equal to the buoyant weight of the target, following:

$$Fa_z(z) - W_b = 0. \tag{4.1}$$

As the beam is steered along the *z*-axis using Eq.(3.5), its intensity drops, thus lowering the acoustic radiation force experienced by the object. Thus, the relation of steering and the location of equilibrium is not linear, since the beam would lose its ability to maintain the same acoustic radiation force farther away from the focus. Simulation of 7.5-watt acoustic vortex beams of M = |3| and |4| were performed to demonstrate the location of desired beam steering vs the actual location of a 3-mm spherical glass bead (Figure 4.2). As previously hypothesized, steering further from the geometric focal point results in weaker forces and the actual target does not reach the desired location. Both beams M = |3| and |4| yield similar steering behavior up to steering 10 mm along the acoustic axis where the target will move to about 9.5 mm or 0.5 mm short of the desired location. However, for wider steering range along the *z*-axis, the narrower vortex of M = |3| is more efficient at axial pushing than M = |4|. This result agrees with our findings from the previous chapter, as narrower beams with larger ratio of bead diameter to beam width (η) have higher axial acoustic radiation force component. Furthermore, we can conclude that for two consecutive

topological charges with the same acoustic power, the axial steering up to a specific range has similar behavior and this range depends on the acoustic power used.

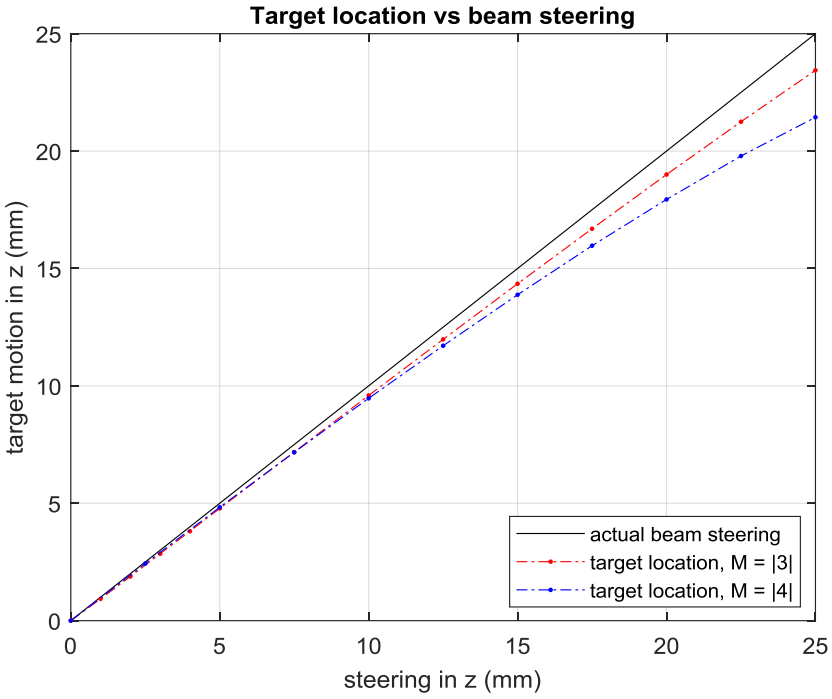

Figure 4.2: The experimental target locations when steered are shown for $M = |3|$ (dashed red line) and |4| (blue dashed line), as the beam is steered along the acoustic axis (black solid line). Both beams yield the same result to move a 3-mm target up to 10 mm along the z-axis with negligible difference. For larger steering range along the z-axis, the $M = |3|$ is more efficient, since it has larger bead diameter to beam width ratio (η).

There are two methods for moving an object along the *z*-axis relative to the array's location: the first method is through electronic steering using Eq.(3.5) and the second method is by increasing the voltage or the acoustic power, as the increased radiation force will push the target up resulting in a higher equilibrium position. We examine the lateral stability of the targets and the steering efficiency using both methods. First, from Figure 4.2, a 7.5-watt (5 volts) $M = |4|$ beam was used to steer the target 3 mm along the *z*-axis away from the array, then the *x*-component of the acoustic radiation force was plotted at the equilibrium position. Second, the acoustic power was increased to 10.8 watt (6 volts) for $M = |4|$ without steering, resulting in a new equilibrium

position 0.5 mm higher, i.e. the target moved 0.5 mm away from the array, and the *x*-component of the acoustic radiation force was plotted at the new equilibrium position. Figure 4.3 shows the *x*-component of the radiation force of a 3-mm glass bead for both methods. The target is at a stable trapping position as any perturbation from its position in the *xy*-plane origin will result in restoring forces placing it back in the center. However, the restoring lateral force of the steered beam are larger than those of the beam with higher acoustic power. At first, such observations may seem counter intuitive; however, for the first case the target was steered along with the beam keeping its location relative to the trapping well of the beam. Conversely, the higher voltage in the second case resulted in a higher equilibrium position along the acoustic axis moving the target relative to the beam where the resulting lateral force were lower, i.e. kicking the target out to a position of a weaker trapping well. We must note the desirability of the first case to steer targets axially, since we are able to move the target 3 mm along the *z*-axis with larger restoring trapping forces rather than using higher power to lift the target a

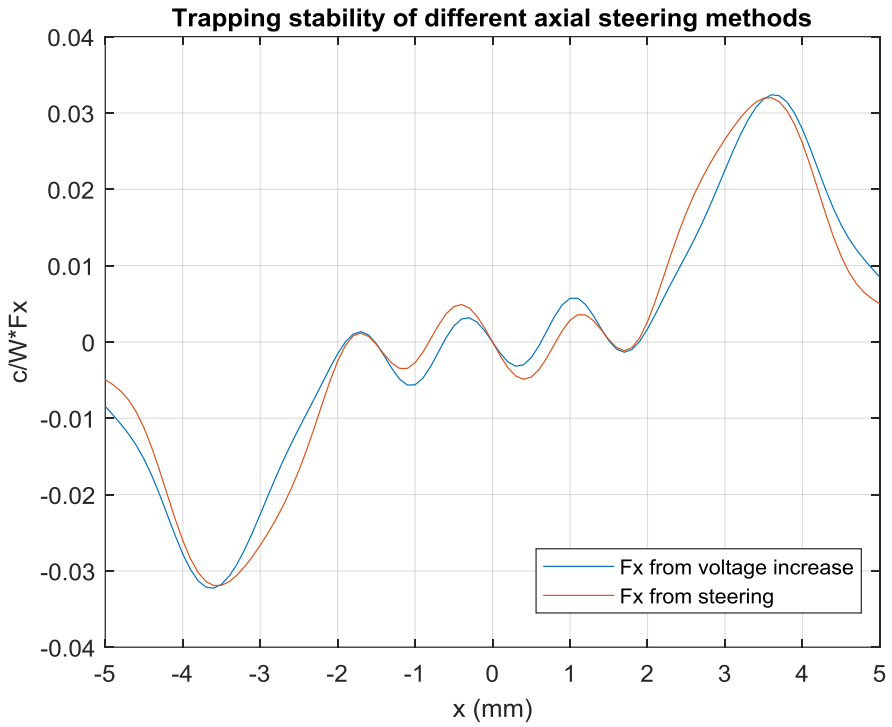

Figure 4.3: The lateral *x*-component of the acoustic force of an $M = |4|$ vortex beam for two different axial steering methods: dynamic steering and increasing voltage. The *y*-axis is a non-dimensional coefficient of the acoustic radiation force. Steering achieved by increasing the voltage results in weaker trapping forces (orange line) than the trapping forces of dynamic steering of targets (blue line).

fraction of the distance (0.5 mm) with weaker trapping forces. In conclusion, the electronic axial dynamic steering of targets has higher trapping lateral forces than increasing the voltage, since the target is sitting deep in the trapping potential well. Additionally, as seen from above, axial steering achieved by increasing the voltage for vortex beams having the same *M* is inefficient as it results in much smaller range requiring higher power levels, which can result in heating and damage of the array or intervening tissues *in vivo*.

4.2.2 *Stability of beam shapes for off-axis steering*

In the previous section, we demonstrated the axial steering range and the most efficient axial steering method. From chapter three, the strength of the lateral trapping force measured is

maximized when the bead diameter to beam width ratio (η) is close to unity. Here, we investigate the optimal beam shape or η to trap and steer a target of a given diameter off-axis. We simulated the electronic steering of a 3-mm spherical glass bead axially and off the acoustic axis by two beams, M = |3| and |4|, with η = 1.07 and 0.88, respectively. The beams were steered 3 mm along the *z*-axis away from the array, and the equilibrium position was found from Eq.(4.1) for each beam. Then the beams were steered 3 mm off-axis (along the *x*-direction) in addition to the previous axial steering, and the *x*-component of the lateral trapping force was found along the *x*-axis, Figure 4.4. From Figure 4.4, The M = |3| beam steered to (3,3) mm in the *xz*-plane resulted in an unstable trap where any perturbation in the bead location will result in its ejection from the center of the beam. For the M = |3| trap, the bead was stably trapped as the beam was steered 3 mm upward in the axial direction; however, at a specific location as the off-axis steering started the trap loses its stability. Conversely, the M = |4| steered to the same location remains a stable trapping beam as the lateral force will restore the bead to the center if any perturbation occurs. Thus, the results of the simulation show that even though when η is close to unity and maximum efficient lateral trapping is achieved, for levitation and off-axis steering, $\eta < 1$ is needed to stabilize the target in the trapping well, i.e. the beam needs be wider than the bead diameter to achieve three-dimensional manipulation.

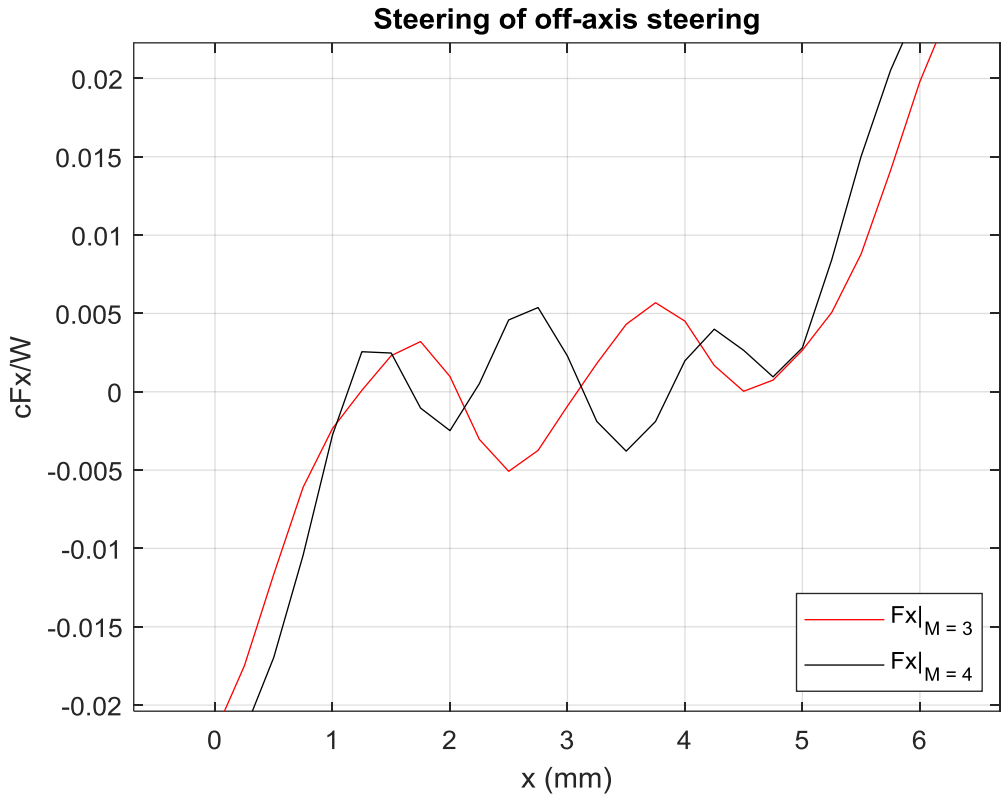

Figure 4.4: The off-axis stability of M = |3| and |4| beams steered to (3,3) mm in the *xz*-plane for a 3-mm glass bead steered. The bead is in an unstable trapping position when $M = |3|$ (red line) as any perturbation from the center it will be ejected. The bead sits in a stable position when $M = |4|$ as with any perturbation in its location, the lateral forces will restore it to the center of the beam. Therefore, for stable off-axis steering, the bead needs to be smaller than the beam width ($\eta < 1$).

4.2.3 *Demonstration of three-dimensional manipulation through tissue-mimicking gel in vitro*

The investigation of the variable space to find the optimal parameters for trapping and manipulating a target in three-dimensions led to multiple findings. These findings include the steering range for two consecutive topological charges, the steering method and the stability of off-axis steering. Thus, the optimal beam shape is chosen based on desired motion range, direction and the stability of targets over that motion.

Using the previous results, we whether we could achieve successful manipulation of an object using three-dimensional electronic steering with an $M = |4|$ of 3-mm spherical glass resting beyond

tissue-mimicking gels. First, the appropriate voltage level was found to levitate the sphere (10.8 watts for this setup). The array was placed facing upward and 3 layers of tissue-mimicking gels were placed above it with the 3-mm glass bead sitting in a confined space mimicking the bladder at the very top. The first layer was a 4-cm thick ballistic gel layer. The second layer was made of Polyvinyl Alcohol (PVA) and has a variable thickness across the surface with an average of 1-cm thickness. The 3-mm glass bead was sitting inside a cylindrical-shaped ballistic gel confinement with a 1.5-cm thick bottom above the PVC layer to mimic the bladder, Figure 4.5. The 3-mm bead

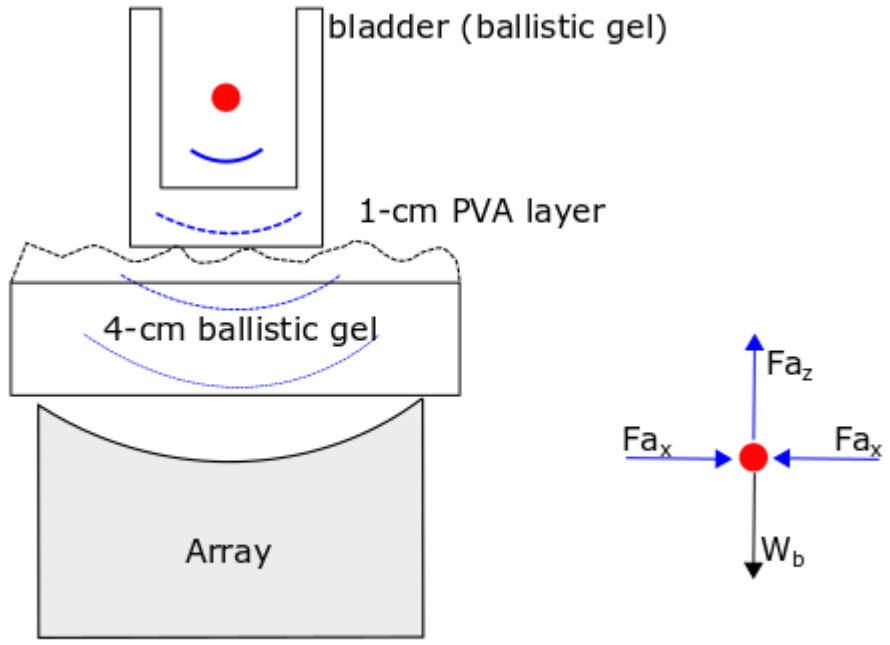

Figure 4.5: Experimental setup of three-dimensional steering using an M = |4| beam of a 3-mm glass bead resting beyond three tissue-mimicking gel layers with the power source voltage set to 6 volts. The wavefronts are dashed in the tissue-mimicking layer and solid in water. The free body diagram to the left shows the acoustic trapping and axial forces (blue arrows) and gravitational pull (black arrow) that achieve the three-dimensional trap. Note that steering is performed at low speed to eliminate hydrodynamic effects.

was steered 5-mm away from the array along the acoustic axis, then it was moved in a circular shape in the *xy*-plane with a radius of 5 mm. Figure 4.6 demonstrates a snapshot of the multiple

locations of the bead as it was manipulated in the previously mentioned path. In the beginning of the axial steering, multiple oscillations in the axial direction occur due to the delayed response of the driving electronics (Verasonics Data Acquisition System, VDAS, chapter two) to transmit the steering beam.

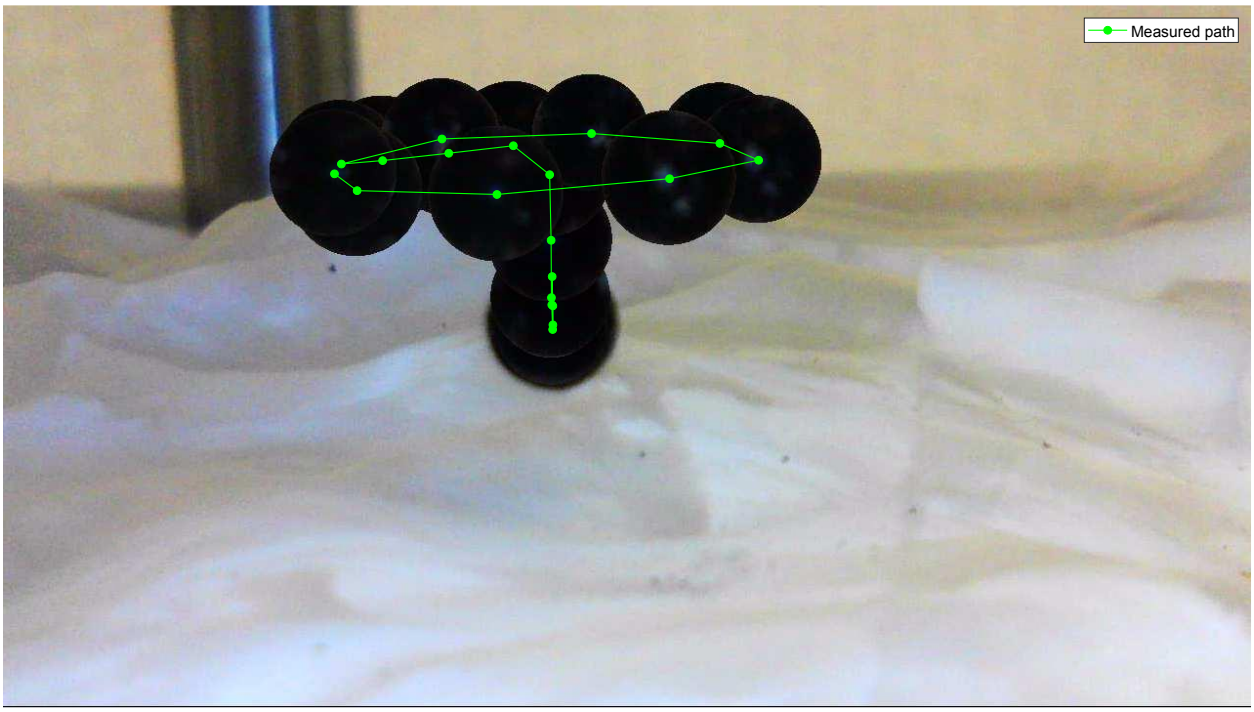

Figure 4.6: Three-dimensional steering *in vitro* of 3-mm glass bead using an $M = |6|$ beam. The object is axially steered 5 mm away from the array, then manipulated in a 5-mm radius circular path. In the initial transition from the levitation place to the start of the axial motion, the bead oscillates up and down few times due to the small delay of the VDAS in transmitting the axial beam.

4.3 THREE-DIMENSIONAL MANIPULATION *IN VIVO*

In this section, we use the optimal parameters found in the previous section to demonstrate the successful trapping and three-dimensional steering of a 3-mm spherical glass bead inside the bladder of a live pig under anesthesia. The operation presented several challenges including, the experimental setup and positioning of the pig to achieve coupling in a viable acoustic window, targeting of the stone and observation of the trapping and manipulation to measure success. The

manipulating of the stone is recorded using ultrasound imaging and visually through the insertion of a cystoscope inside the bladder of the pig. The operation performed here was the first *in vivo* successful trial of non-invasively monitoring and ultrasonically manipulating a solid object inside a living body, paving the way for a multitude of medical applications, such as, removal of kidney stones, blood clots, foreign objects, and targeted drug delivery. Such technology could, for instance, be used to treat emergency blockages in ureters by kidney stones in astronauts and cosmonauts in long space flights.

4.3.1 *Methods*

A 3-mm spherical glass stone was used to mimic a kidney stone. Objects such as kidney stones can be easily visualized in the bladder on ultrasound imaging due to their high reflective quality resulting in a bright ultrasound image. The bead was painted blue in order to have a strong contrast with the surrounding biological tissue for ease of visual imaging with the cystoscope. The bead was inserted endoscopically into a small 80-lbs female pig under anesthesia through the urethra with a cystoscopy-guided wire basket. An ultrasound imager was mounted in the center hole of the multi-element array (Figure 2.1) that is placed under the pig to levitate and manipulate the target in three-dimensional space.

4.3.1.1 Experimental setup

The pig was laid on its side on a surgical table with its lower abdominal section above a 29-gallon acrylic tank and its rear legs resting on a table and secured by a sling. The array was placed in the tank below the pig and was attached to a three-dimensional positioning system mounted to a metal frame. A Philips P6-3 sector probe was mounted through the center hole of the array for ultrasound imaging of the three-dimensional manipulation. The acoustic window for targeting of

the bead was from the side of the lower abdominal section with water coupling between the array surface and the pig (Figure 4.7).

4.3.1.2 Ultrasound targeting

For the successful manipulation of the stone inside the bladder, the location of the target with respect to array's elements needs to be known. A Philips P6-3 probe was used in the ultrasound targeting of the stone and imaging of the manipulation. The probe operated at a center frequency of 4.5 MHz and was connected to a VDAS system running a rayline script that images to a depth of 14 cm. The probe was mounted in the center hole with the probe elements located in the apex of the array to avoid interference with the acoustic waves emitted from the array's elements. Then a capsule hydrophone was placed in the acoustic focus of the array and the location of the acoustic focus defined by the hydrophone tip location, where the maximum pressure amplitude was recorded and coded in the imaging script window to display red crosshair at the location of the acoustic focus that was used to target the stone *in vivo* for the three-dimensional manipulation (Figure 4.8).

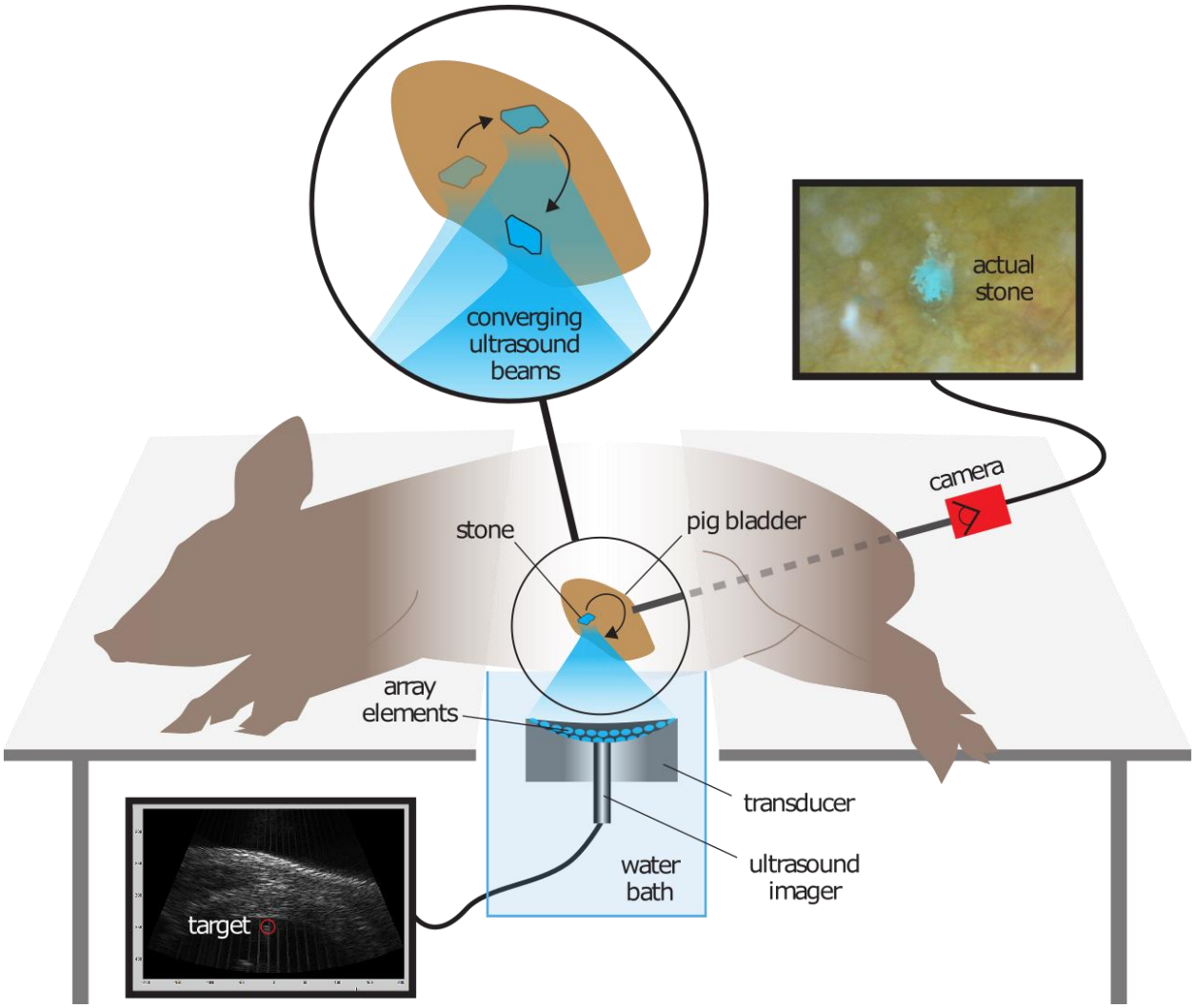

Figure 4.7: Experimental setup of three-dimensional manipulation of stone (3-mm glass bead) inside the bladder of a pig under anesthesia. The array is placed below the pig with water coupling to the lower side abdominal area which is the acoustic window to access the bladder. A Philips P6-3 sector probe is mounted in the center hole of the array for ultrasound imaging and guiding. A borescope is inserted through the urethra into the bladder to visually record and observe the surgery.

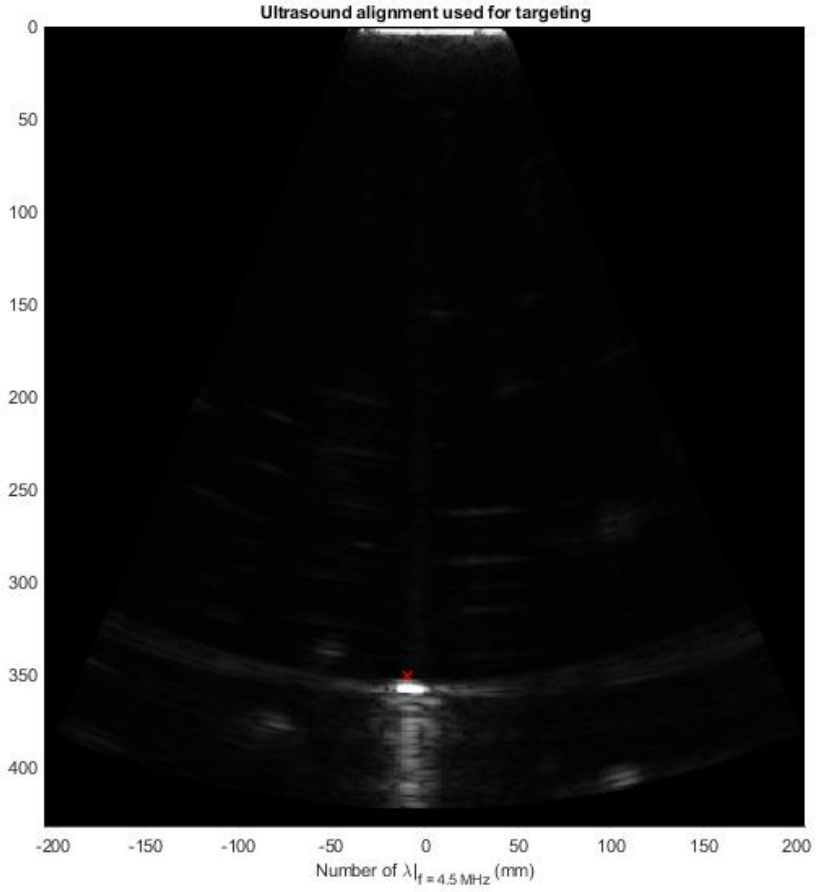

Figure 4.8: The alignment method used to mark the location of the focus (red crosshair) to be used for ultrasound targeting of the stone *in vivo*. A capsule hydrophone scans the field until the acoustic focus is found by recording the maximum pressure amplitude where the red crosshair is coded into the imaging script.

4.3.1.3 Three-dimensional manipulation path, signal properties and voltage level

After targeting the stone using ultrasound, the array transmitted the signal to control the stone in a predefined path. The initial pulses aligned the stone with the focal axis of the array by initially transmitting a large vortex beam of $M = |35|$ and lowered sequentially to an $M = |4|$ to squeeze and align the stone to the center. Based on previous simulation in section 4.2, an $M = |4|$ vortex beam was chosen, since η has a value of 0.88, which provided stable trapping for steering in three dimensions. Two steering paths were preprogrammed in the VDAS system used for driving the array. The first path (path 1) axially steered the bead 3 mm upward in the *z*-axis, then 3 mm in the

positive *y*-axis of the imaging prove, and 3 mm back down in the *z*-axis. The second path (path 2) axially steered the bead 3 mm upward in the *z*-axis, then 3 mm in the positive *y*-axis followed by a tracing a 3-mm radius circular path. The delays for each element for both paths were calculated from Eq.(3.5) with each transmitted signal at a specific location consists of a positive followed by a negative *M* for a total pulse length of 1.32 milliseconds with an equal off-time resulting in a 50% duty cycle. For both paths, the stone was targeted using the red crosshair of Figure 4.8 using the targeting script. Then the multi-element array was triggered to trap and mechanically levitate the stone by moving toward the pig, in order to get the stone of the bladder wall. The VDAS was triggered again to transmit the preprogrammed steering path. The first path was transmitted at 5 volts and the second path at 5.9 volts having a time-averaged power of 7.5 and 10.5 watts, respectively.

4.3.1.4 Ultrasound imaging

The P6-3 probe imaged and recorded the manipulation in the pig using a rayline script. The driving VDAS sent two consecutive pulses at a specific location to control the stone, then triggered the imaging VDAS, which sent a number of raylines in the off-time to eliminate interference and construct the image. The P6-3 probe imaged to a depth of 14 cm allowing for 5 raylines in each imaging pulse to be sent and received by the probe elements during the off-time of manipulation pulse. Therefore, a total of 26 imaging pulses (each transmitting 5 raylines) were required to construct one ultrasound image resulting in a 14 frames per second refresh rate for the ultrasound imaging. Since the target motion was very slow (1 and 1.7 μm per pulse for path 1 and 2, respectively), the maximum distance covered after 26 pulses (one frame) was less than 45 μm, thus, maintaining a well-updated motion tracking of the stone.

4.3.2 *Results and discussion*

Manipulation of the 3-mm glass bead was attempted in two pigs. In the first pig, the bladder contained biological matter that was floating around and made ultrasound targeting difficult. At one trial, the bead was trapped and manipulated; however, low ultrasound and cystoscope image quality were inconclusive. The ultrasound imaging and manipulation pulses were not in sync leading to interference lines on the ultrasound image. While the cystoscope used in the first pig was inflexible and had low lighting and resolution. Most importantly, the manipulation path was transmitted while the glass bead was still in contact with the bladder wall, which increased the complexity of the steering, since the breathing motion of the pig was on the same order of the steering distance.

The issues faced in the first pig were resolved in the second pig as was explained in the methods sections. The 3-mm glass bead was successfully manipulated in three-dimensional space with electronic Steering. The manipulation was observed using a cystoscope and ultrasound imaging. The results of each path are presented separately.

4.3.2.1 Acoustic manipulation along path 1

The manipulation along path 1 was attempted five different times that were all successful. Figure 4.9 shows the blue-painted glass bead along 7 different locations with its centroid colored and labeled in a chronological order of motion. The white dashed line superimposed on the image is to show the general path of the steering. It is evident that the bead moves up (point 1 to 5), then

across (point 5 to 6) and back down (point 6 to 7). The difficulty in interpreting the

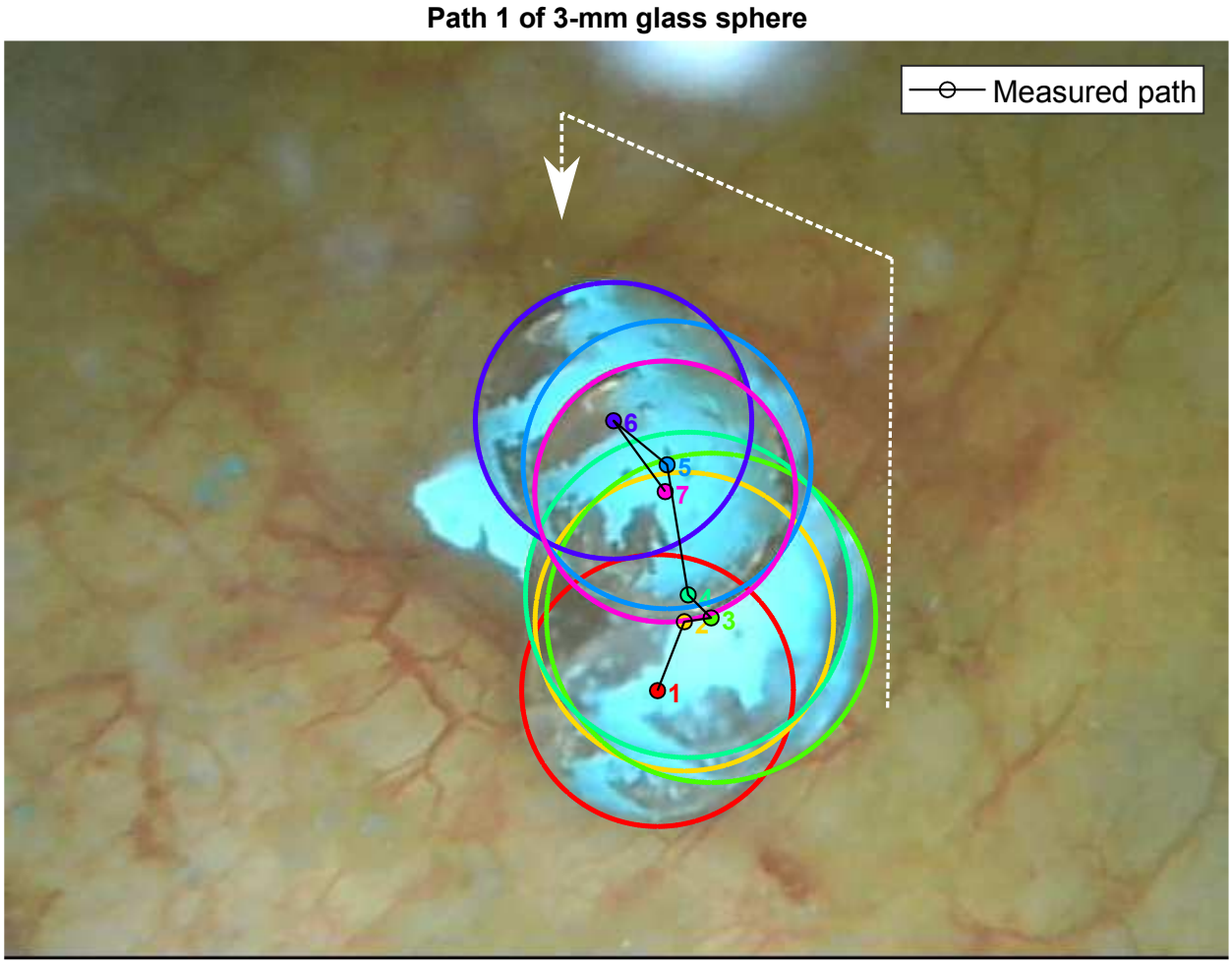

Figure 4.9: Still shot series of images of the locations of the 3-mm glass bead along path 1 inside the pig bladder filmed by a borescope inserted into the bladder through the urethra. The centroid of each location is marked and has the same color as the border of the bead when at that location. The white dashed line shows the general direction of desired motion due to difficulty in interpreting the motion path because of breathing motion of the pig and the cystoscope operator.

actual motion of the bead is due to, motion of the pig, and alignment and operation of the cystoscope. The bead was programmed to move axially and in the plane of the ultrasound imager (*y*-axis), which was also chosen to coincide with the in-plane direction of the cystoscope; however, the physiology of the urethra and bladder of the pig resulted in visually observing the experiment from an angle as shown in Figure 4.7, rather than a perpendicular alignment between viewing axis and motion path. In addition to the motion of the bead, there was the breathing motion of the pig

and the operator of the cystoscope, making it difficult to maintain a stable reference point. Therefore, the background in Figure 4.9 belongs to the location of the bead in the first frame with the following locations superimposed to eliminate the breathing motion of the pig.

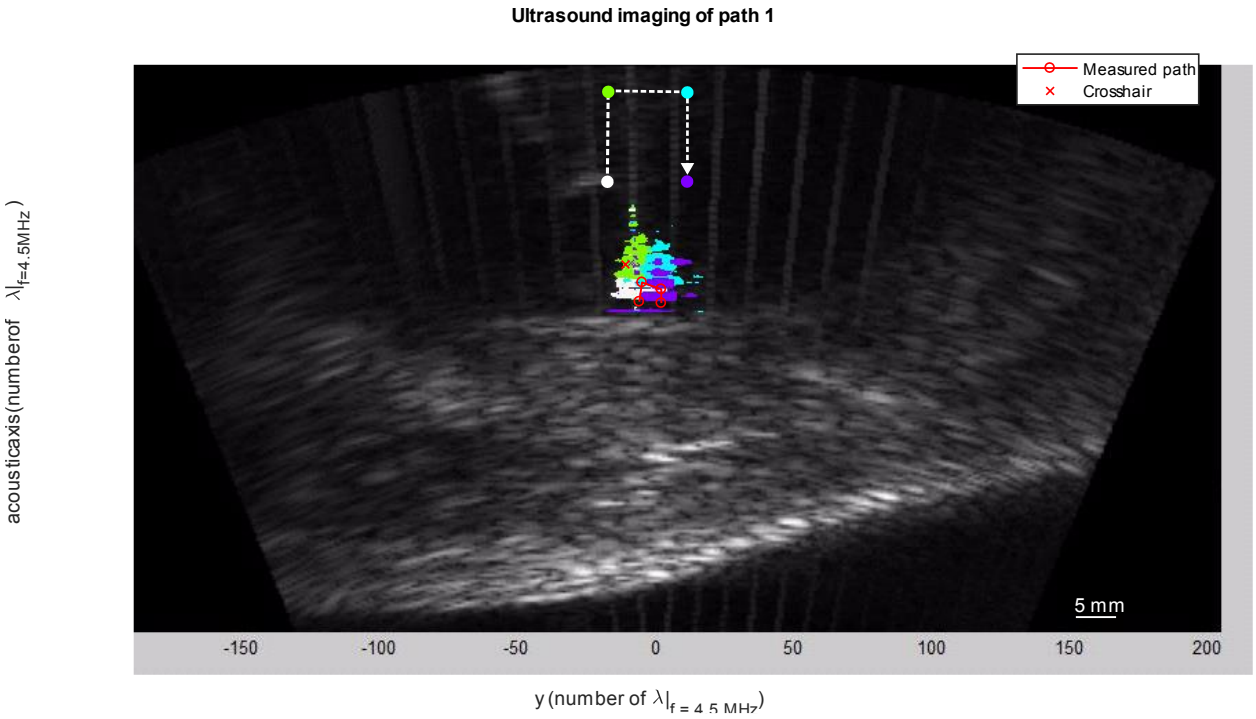

Figure 4.10: Still shot series of images of the locations of the 3-mm glass bead along path 1 inside the pig bladder from ultrasound imaging taken by a P6-3 probe. The colored locations indicate the major four points along the desired path in the *yz*-plane, after trapping at the origin (white), at (0,3) mm (green), at (3,3) mm (cyan), and back down at (3,0) mm (purple). Red line indicates the estimated centroidal location of the glass bead. The dashed white arrow (not drawn to scale) presents the sequence and direction of the intended motion path.

The ultrasound imaging solves the challenges faced by the cystoscope view. The P6-3 imaging probe was aligned so that the motion of the bead was in the imaging plane. The probe location was fixed with respect to the array and the array was fixed with respect to the bladder wall during the three-dimensional steering allowing definitive visualization of the motion path. Figure 4.10 is a still shot series of images of the different locations of the bead superimposed onto the first frame of the trapping. Four locations are shown in the *yz*-plane, the start of the trapping, levitation along the acoustic axis to (0,3) mm, off-axis steering across the y-axis to (3,3) mm, and finally back

down to (0,3) mm. The ultrasound imaging is more decisive in understanding the motion path since it is fixed in three-dimensional space and always has a fixed reference point on display (red crosshair) unlike the borescope recording in which everything is in motion relative to each other.

To quantify the motion of the bead using the ultrasound image, the spacing between two points on the x-axis in Figure 4.10, the nominal sound speed in tissue (1540 m/s) and the center frequency of the imaging probe (4.5 MHz) were used to find the relation between the millimeters per pixel on the image. Figure 4.11 shows the intended motion and measured motion based in millimeters. It is notable that the intensity of beam inside the bladder was weaker as the bead did not reach the intended levitation height and dropped even farther during the off-axis steering to (3,3) mm, since the distance between the length of the vertical line going down is shorter than that going up. The decrease of intensity or attenuation inside the pig was not quantified, but it was due to the thick layer of the body wall consisting of muscle and fat tissue layers. Also, the last point for the measured path is shown to be below the starting location, indicating the existence of a tilt angle between the imaging probe and the array. This tilt angle was visually noticeable as the probe was placed inside an aluminum tube to fit in the center hole of the array.

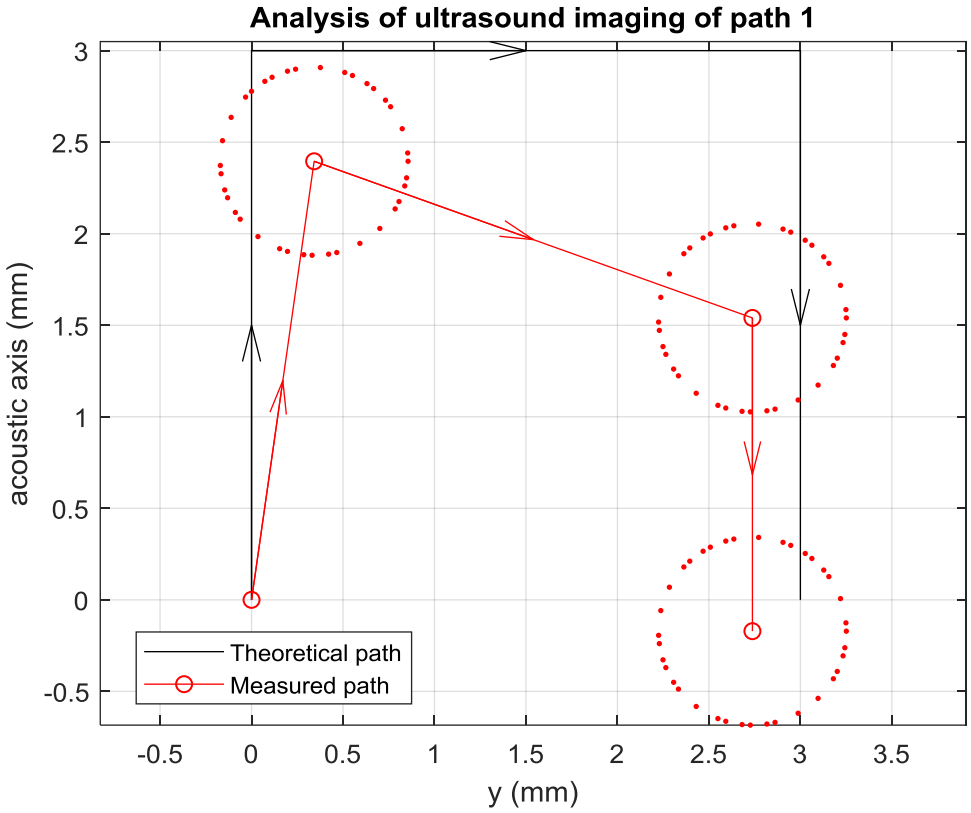

Figure 4.11: Analysis of ultrasound imaging of motion of 3-mm glass bead along path 1. The intended motion in (black) is compared to the measured motion (red) with the associated error circle around each centroidal location (dotted red). The measured motion was scaled using the *x*-axis of Figure 4.10 The difference in motion is mainly due to attenuation. A slight angle exists between the array and the imaging probe based on the tilt of the path.

The absolute distance between the intended and measured centroidal location was calculated and for each point and presented in Table 4.1. In addition to attenuation of the acoustic beam intensity, the difference between the measured and intended path was due to, first, the different sound speed in different mediums affecting the scaling factor and the second, the method of selecting the centroidal location. Sound speed propagates differently in water (1480 m/s) than in tissue (1540 m/s) and the scale shown in wavelength in Figure 4.11 was based on the sound speed in tissue; however, the distance over which the wave traveled through consisted of three mediums as it propagated through water in the tank, then through body wall of the pig and finally in urine inside the bladder. It was estimated that maximum difference in sound speed in the mediums

accounted for maximum error of 0.087 mm in the measured centroidal location. Also, the centroids' locations were chosen manually on the ultrasound image to be at center of the brightest front face of the scatterer. On average the error associated with manually picking the locations was estimated to be within 3 pixels, which when combined with the error from the sound speed calculation was approximately 0.52 mm. The absolute difference in distances presented are within the expected error, except at the first and third locations, which as mentioned before could be due to attenuation of the beam over a specific region in the body wall.

Table 4.1: Absolute difference between intended and measured centroidal locations of the bead along path 1.

Point along path 1	1	2	3	4
Absolute difference (mm)	0	0.69	1.5	0.31

4.3.2.2 Acoustic manipulation along path 2

In a similar fashion to path 1, path 2 was recorded by a cystoscope and ultrasound imaging using the P6-3 probe. The manipulation along path 2 was attempted four times, two times the bead fell off the trap three quarters of the way along the circular section of the path. The voltage was increased by less than one volt resulting in an increase from 7.5 to 10.8 watt. After the power increase the motion was successful for the two remaining trials that followed. Figure 4.12 shows the axial steering of the bead to (0,3) mm, then off-axis steering to (3,3) mm in the *yz*-plane (point 1 to 7), then moving the bead in a circular path (point 7 to 13). Despite the challenges in interpreting the motion for path 1, the circular motion can be clearly interpreted from the still shot series images from the cystoscope of Figure 4.12. The centroidal locations are marked chronologically and colored along with bead border to demonstrate the path taken by the bead during the three-dimensional steering process. All locations are superimposed on the first frame for clear display of the path.

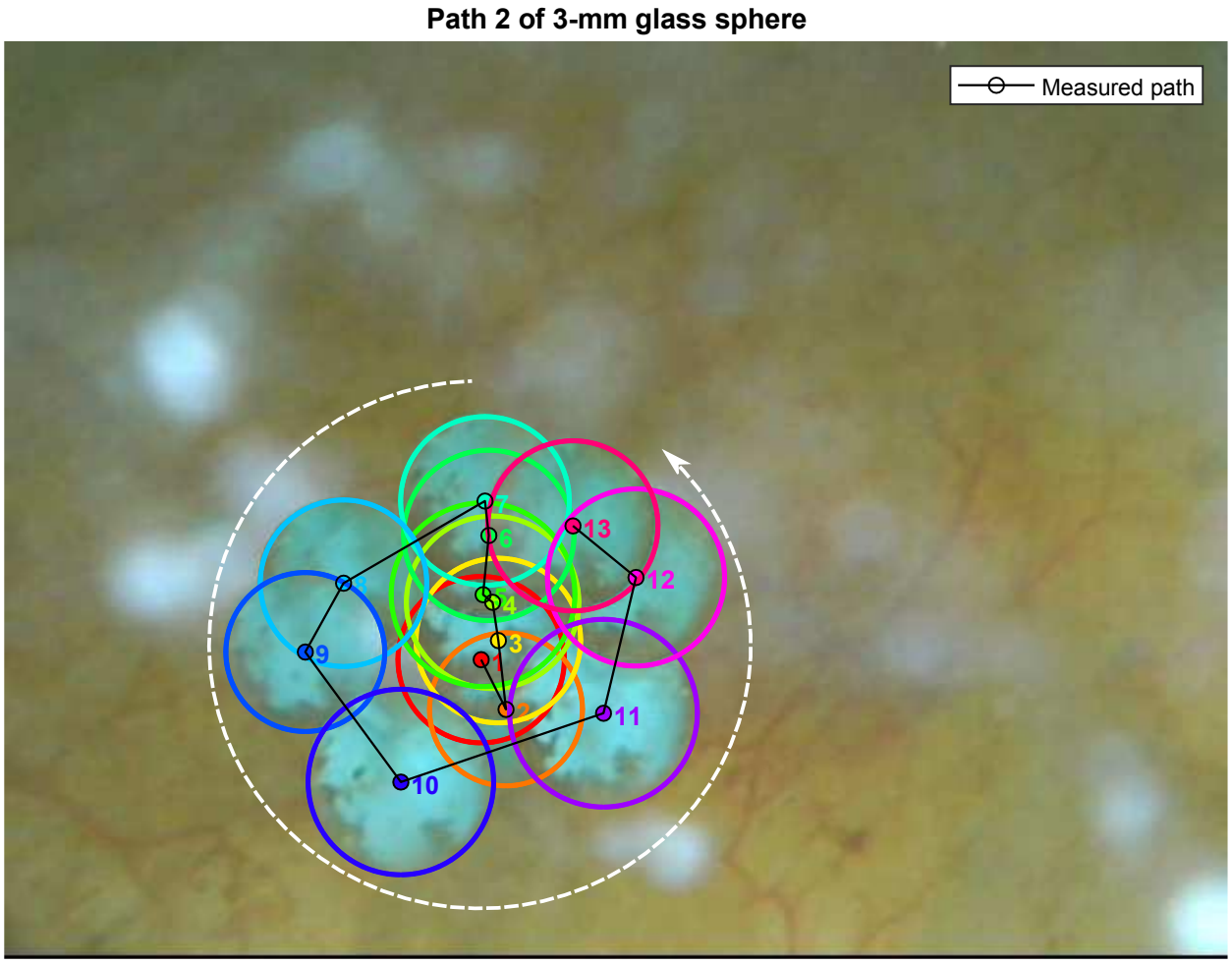

Figure 4.12: Still shot series of images of the locations of the 3-mm glass bead inside the pig bladder filmed by a borescope inserted into the bladder through the urethra. The centroid of each location is marked and has the same color as the border of the bead when at that location. The white dashed line shows the general direction of the desired circular motion only.

The ultrasound images are also displayed in the same manner of path 1 by superimposing multiple locations of the bead ringing onto the first trapping frame (Figure 4.13). Five locations of the bead are shown in *yz*-plane, the initial trapping in white at the origin, the vertical axial steering, the off-axis steering followed by two locations at half and the full the length of the circular path. In this setup, we note that the major drawback of the ultrasound imaging was its limitation in capturing the out-of-plane dimension as it was only captured by the brightness level of the target in the image, it dimed as it moved out-of-plane and vice versa.

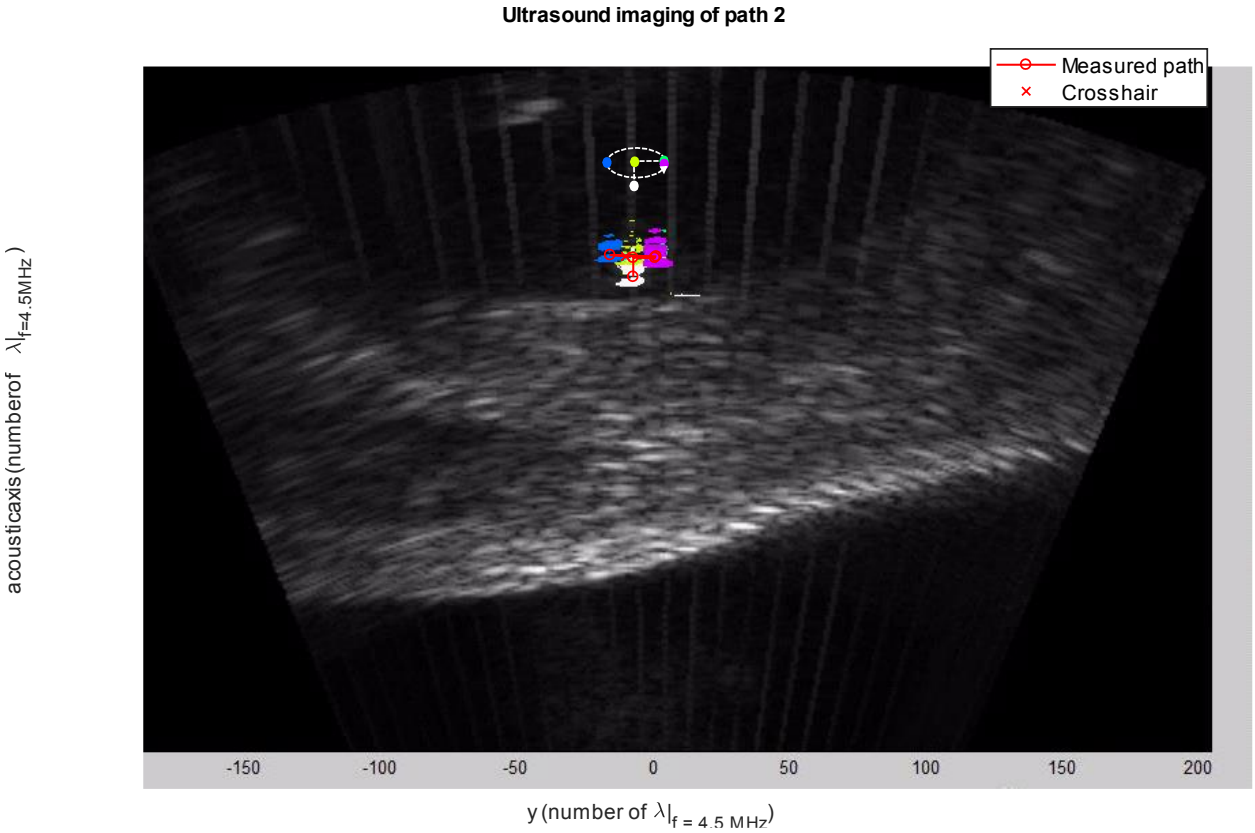

Figure 4.13: Still shot series of images of the locations of the 3-mm glass bead inside the pig bladder from ultrasound imaging taken by a P6-3 probe. The colored locations indicate the major five points along the desired path in the *yz*-plane, after trapping at the origin (white), at (0,3) mm (lime-green), at (3,3) mm (green), at (-3,3) mm (blue) and back across at (3,3) mm (purple). The red line indicates the estimated centroidal location of the glass bead. The dashed white arrow (not drawn to scale) presents the sequence and direction of the intended motion path.

The ultrasound imaging of path 2 was quantified in a similar manner presented in the section above and the comparison between the measured and intended paths is presented in Figure 4.14. The errors of the different sound speed in different mediums and selecting the centroid associated with the measurements are the same as those mentioned for path 1. The tilt angle can also be seen from that tilt between both sides of the one-dimensional projection of the circular path. We note that in Table 4.2, the absolute difference in distance between the measured and intended path seem to be with in the associated error with this analysis, 0.52 mm.

Table 4.2: Absolute difference between intended and measured centroidal locations of the bead along path 2.

Point along path 2	1	2	3	4	5

Absolute difference (mm)	0	0.31	0.44	0.28	0.44

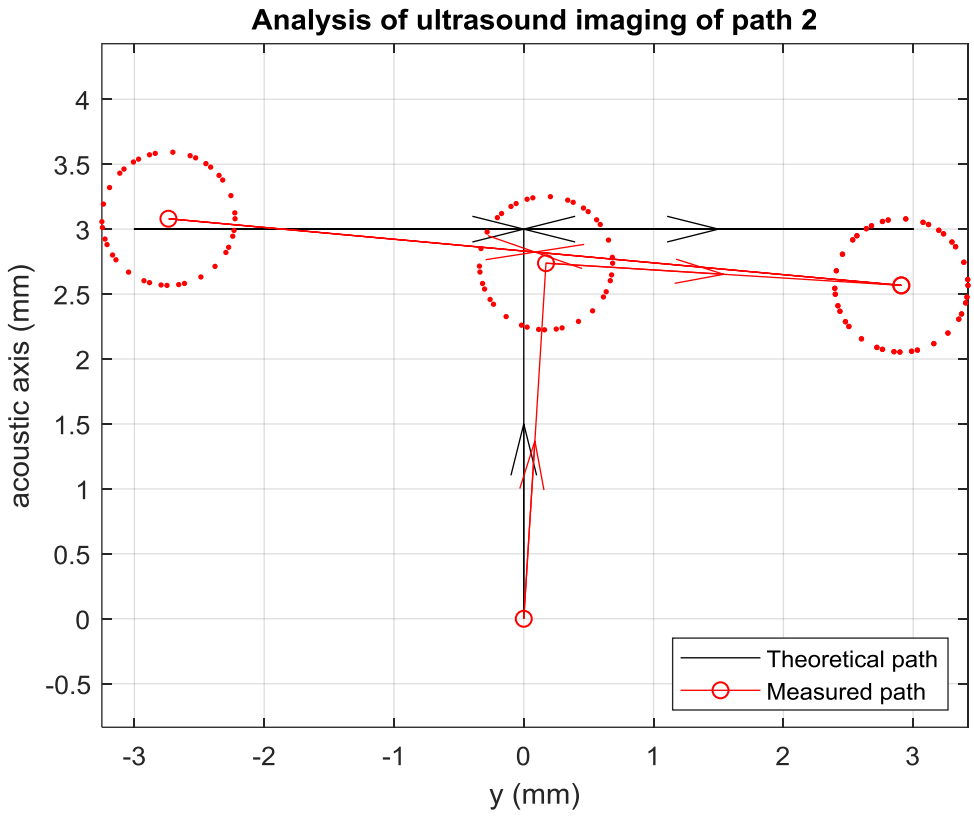

Figure 4.14: Analysis of ultrasound imaging of motion of 3-mm glass bead along path 2. The intended motion in (black) is compared to the measured motion (red) with the associated error circle around each centroidal location (dotted red). The measured motion was scaled using the *x*-axis of Figure 4.13The difference in motion is mainly due to attenuation. A slight angle exists between the array and the imaging probe based on the tilt of the path.

Manipulation of a 3-mm glass bead inside the pig bladder was achieved along with the use of ultrasound imaging to monitor the procedure. There are differences between the intended motion and the measured path. The presence of a tilt angle between the imaging probe and array axes was a factor for such differences. It was shown that some of these differences were within the measured error from the scaling method and manual selection of centroids. However, for specific points especially for path 1, the difference in path location was larger than the measured error. This can be contributed to the effect of attenuation as it can vary over different regions of the body wall of the pig. Attenuation was not accounted for in this study; however, a plan is presented for future research of how to account for the attenuation in the next chapter.

The study presented above has strong implications on the non-invasive treatment of kidney stones. Other medical applications include manipulation of blood clots and foreign objects or fragments in the body. Even though attenuation can affect the path of the steering inside the body, it was shown that the motion within an accuracy of a fraction of a millimeter. The work here has future implications on human space flights. For instance, this technology can be used in the non-invasive treatment of astronauts who are at a higher risk of developing kidney stones. Other applications include containerless transport, performing experiments in laboratory setting, and manufacturing.

4.4 CONCLUSION

The development of acoustic tweezers for the manipulation of large heavy objects for the first time in three-dimensional space was demonstrated in this chapter. Simulation of the acoustic radiation force field of vortex beams is performed to realize the optimal relation between object size and beam shape to form stable traps and stable steering mechanisms. The results were used to demonstrate for the first time the successful realization of acoustic tweezers by manipulating a real kidney stone mimicking target (glass bead) inside a live pig under anesthesia. The operation was observed endoscopically through a cystoscope, and non-invasively by an ultrasound imaging probe.

Ch 5:CONCLUSION AND FUTURE WORK

A summary of the work in the development of the acoustic tweezers is presented in the first section followed by the future plans to overcome and solve the challenges faced and to improve the technology.

5.1 CONCLUSION

Toward the goal of developing acoustic tweezers for the manipulation of large objects three major steps were considered: the characterization of the array to enable the synthesis of any desired beam shape, comparison between the theoretical model and measurements of the acoustic radiation forces, and understanding of the variable space to achieve the three-dimensional manipulation of objects. In chapter two, a 256-element array was characterized using holography scan with applied directivity corrections. The directivity-corrected holography scan was used to obtain and localize the complex vibrational output to each element. Localization of the complex vibrational element output was used to equalize their amplitude output and control the phase in order to synthesize uniform vortex beams in the focal plane paving the way for future synthesis of complex beams for manipulation.

In the chapter three, using the equalized output found previously to produce uniform and complex beam shapes, the acoustic radiation force of multiple beam shapes was measured and compared to theory. Vortex beams of equal intensity distribution and radially-varying phase beams were synthesized to measure their lateral trapping strength. Measurements show good agreement with theory and that vortex beams were more efficient at lateral trapping than other beams tested with the most efficient trapping occurring at a target diameter to beam width close to unity. Thus, an important non-dimensional geometrical ratio was defined, η, tying the relationship between an

object size and the needed beam width for efficient trapping. Furthermore, the electronic steering with the array of large laterally trapped targets in two dimensions was achieved preparing the way for three-dimensional manipulation.

In chapter four, the development of acoustic tweezers for macroscopic objects was achieved. Optimal parameters for trapping and methods for steering and off-axis steering were found through simulations. The most optimal value of the previously found ratio η was found to be less than one, in order to achieve a stable well for three-dimensional trapping and steering of targets. Furthermore, the steering range for vortex beams was found along with the fact that electronically steering the beam at lower power is more stable in the axial direction. Consequently, the results were used to demonstrate for the first time the successful trapping and three-dimensional controlling of a 3-mm glass bead, similar to kidney stone, in a live pig with non-invasive ultrasound imaging. Thus, future applications of this technology are numerous ranging from medical application, such as, removal of foreign objects, blood clots, kidney stones, targeted drug delivery; biological applications, such as, cell sorting or arrangements; to manufacturing application, such as in silicon microchips.

5.2 FUTURE WORK

The work accomplished presents the initial development of acoustic tweezers for macroscopic objects or as commonly referred to tractor beam. However, there are multitudes of discoveries and challenges remaining to tractor beams such as, pulling or negative axial radiation force, torque, nonlinear acoustics, steering and aberration correction, imaging feedback, and optimization of array design. For instance, vortex beams are shown to have negative radiation forces or the ability to pull objects in a direction opposite to the wave propagation direction [19], [39], [40], [92]. Negative axial radiation force on very small objects compared to the wavelength are demonstrated

in [11], [26], using vortex beams and using bottle beams in [10], [21]. However, I synthesize a three-dimensional bottle beam with the ability to induce negative radiation forces by using a higher-order vortex beams explained in [20], [69], [93]. A holography scan of the beam axial pressure amplitude is demonstrated in Figure 5.1. Experimental plans are in development to demonstrate the pulling of a 2-mm spherical glass bead which is two times larger than the wavelength. If successful, it will be the first time large objects are pulled toward a single-sided acoustic source, since the only work [27] done in this aspect was the measurement of the pulling forces on a specifically shaped object (triangular prism) to result in forward scattering of the wave, rather than the creation of a bottle beam to surround an spherical object and pull it. The spherical shape offers a great step toward the ability of pulling any shaped objects, especially if on average the deviations from a spherical profile are smaller than the wavelength. Thus, enabling the development the full entrapment and manipulation of objects including pulling.

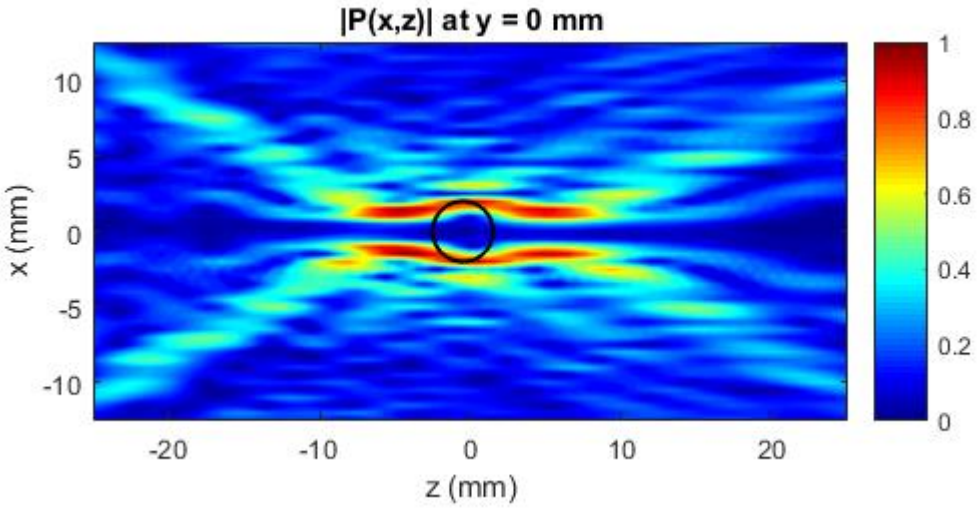

Figure 5.1: Normalized axial pressure amplitude from a holographic scan of a synthesized bottle beam that can induce pulling on large spherical objects up to twice larger than the wavelength (~1 mm) at 1.5 MHz. The black outline shows the typical location of a 2-mm spherical glass bead to induce pulling.

Vortex beams are discussed in details above and shown to produce a radiation torque due to their angular momentum component [36], [77], [78], [85], [87], [88] that can spin objects. For the time being, the torque is suppressed through sending alternative vortex beams. However, preliminary experiments show that non-perfectly spherical targets, oblong shaped objects or distortion of the fields resulting in asymmetry due to some aberrations can cause targets to spin and effectively get ejected out of the trap. This presents a valuable opportunity in medical applications, for instance, in case foreign objects or kidney stones in the body get attached to tissue, they can be twisted off and detached. However, it may make 3D manipulation of such objects more challenging. Numerical modeling along with experiments are needed to understand and study the variable space and optimize it in a fashion similar to that of chapter three so that the torque of these beams can be controlled.

In this work, pulses rather than a continuous wave are used, since the acoustic radiation force is a time average quantity [1]–[3]. Pulses allow for the ultrasound imaging during the off-time eliminating interference between the imaging and tweezers pulses. However, to deliver the same time average power of a continuous wave or higher power in general, higher amplitude pulses must be transmitted leading to nonlinear acoustic propagation which is well known. However, the radiation force from nonlinear acoustic propagation is not well studied or investigated. For instance, it is valuable to investigate the effect of higher harmonics on the resulting radiation forces, as the inclusion of these frequencies may cause unpredictable behavior. Therefore, the effects of acoustic nonlinearity on trapping radiation forces need to be studied by accounting for nonlinear scattering in the numerical model of Ref [76] and performing experimental measurements for verifications.

The off-axis steering of the acoustic beam weakens the field in a predictable way. Mathematical models need to be completed and implemented to correct for such behaviors, so targets are always held with same force. As the acoustic trapping beam passes through inhomogeneous material, such as tissue, the waves are attenuated and refracted disrupting the desired beam shape at the trapping location. Time reversal acoustics can be used to correct for such aberrations. In time reversal acoustics [8], [49]–[52] a focused beam is reflected from a point scatterer and received by all elements, then the time-reversed received excitation is applied to the transducer elements. An iterative method can be performed to correct for the different paths of the different rays. The manipulation of large objects presents the ideal situation as each object in the field exemplify a single scatterer. The future development and implementation of dynamically compensating for the changing paths through real-time time reversal will enable the ability to move objects behind any aberrative non-uniform media accurately and with confidence. Also, for the manipulation experiments *in vivo*, an ultrasound imaging positioned in the center of the multi-element array is used to target the stone in the bladder. However, the array itself can send and receive pulses and triangulate to the target. Future plans to incorporate this triangulation and use it to automatically target and track the stone movement with the development of the automatic compensation techniques will mark the completion of a comprehensive acoustic tweezers to be used to target, track and manipulate any objects with a stable acoustic trap in three-dimensional space in a given medium.

Lastly, even though the work presented is concerned with acoustic tweezers for large objects, the array operates at a high frequency resulting in a smaller wavelength, which introduces a set of challenges. For instance, at such small wavelength (1 mm), pulling objects becomes a challenging as it only relies on the acoustic scattering [3], [24], [76] rather than on the gradient forces [22].

Thus, using a longer wavelength or lower frequency source, the pulling can increase as the contribution from the gradient forces will increase. Furthermore, in preliminary experiments of trapping non-spherical objects with vortex beams, the objects start spinning due to the asymmetry introduced. I hypothesize that when the asymmetry is on the order of the wavelength, wavefronts lead to uneven radiation pressure inducing a net average torque even with the transmission of pulses with opposite topological charge. Thus, at lower frequency or larger wavelength, the asymmetry will not be seen by the wavefront eliminating the net torque and allowing the trapping of non-symmetrical objects in general. Designing and fabricating a new multi-element array will enable the testing of the previous hypotheses. The new design will operate at a lower frequency and will have a much larger unfocused aperture allowing the generation of moderate pressures over a much larger region to steer objects over a greater range. Such large array can be divided to sectors where specific section is used for imaging and tracking targets while another section for manipulation of targets simultaneously. Ultimately leading to an acoustic tweezers able to target and dynamically manipulate large heavy objects in real-time, track and image their path in three dimensions with real-time compensations for aberrative obstacles in a given medium. This system can be used for medical non-invasive treatments of large foreign objects in the body, blood clots or targeted drug delivery, performing experiments with low or no contamination in laboratories or space flights, and manufacturing applications.

BIBLIOGRAPHY

[1] P. J. Westervelt, “Acoustic Radiation Pressure,” *J. Acoust. Soc. Am.*, vol. 26, no. 1957, pp. 1–5, 1957.

[2] P. J. Westervelt, “The Theory of Steady Forces Caused by Sound Waves,” *J. Acoust. Soc. Am.*, vol. 23, no. 3, pp. 312–315, 1951.

[3] L. V King, “On the Acoustic Radiation Pressure on Spheres,” *Proc. R. Soc. London. Ser. A - Math. Phys. Sci.*, vol. 147, no. 861, p. 212 LP-240, 1934.

[4] T. Hasegawa and K. Yosioka, “Acoustic-Radiation Force on a Solid Elastic Sphere,” *J. Acoust. Soc. Am.*, vol. 46, no. 5B, pp. 1139–1143, 1969.

[5] T. F. W. Embleton, “Mean Force on a Sphere in a Spherical Sound Field. I. (Theoretical),” *J. Acoust. Soc. Am.*, vol. 26, pp. 40–45, 1954.

[6] A. A. Doinikov, “Radiation force due to a spherical sound field on a rigid sphere in a viscous fluid,” *J. Acoust. Soc. Am.*, vol. 96, no. 5, pp. 3100–3105, 1994.

[7] T. Hasegawa, M. Ochi, and K. Matsuzawa, “Acoustic radiation force on a solid elastic sphere in a spherical wave field,” *J. Acoust. Soc. Am.*, vol. 69, no. 4, pp. 937–942, Apr. 1981.

[8] C. Prada, S. Manneville, D. Spoliansky, and M. Fink, “Decomposition of the time reversal operator: Detection and selective focusing on two scatterers,” *J. Acoust. Soc. Am.*, vol. 99, no. 4, pp. 2067–2076, 1996.

[9] D. Foresti, M. Nabavi, M. Klingauf, A. Ferrari, and D. Poulikakos, “Acoustophoretic contactless transport and handling of matter in air,” *Proc. Natl. Acad. Sci.*, vol. 110, no. 31, pp. 12549–12554, 2013.

[10] A. Marzo, S. A. Seah, B. W. Drinkwater, D. R. Sahoo, B. Long, and S. Subramanian,

"Holographic acoustic elements for manipulation of levitated objects," *Nat. Commun.*, vol. 6, no. May, p. 8661, 2015.

[11] D. Baresch and J. Thomas, "Observation of a Single-Beam Gradient Force Acoustical Trap for Elastic Particles : Acoustical Tweezers," vol. 024301, no. January, pp. 1–6, 2016.

[12] M. A. B. Andrade, N. Pérez, and J. C. Adamowski, "Particle manipulation by a non-resonant acoustic levitator," *Appl. Phys. Lett.*, 2015.

[13] R. R. Whymark, "Acoustic field positioning for containerless processing," *Ultrasonics*, vol. 13, no. 6, pp. 251–261, 1975.

[14] E. H. Brandt, "Acoustic physics. Suspended by sound.," *Nature*, vol. 413, no. 6855, pp. 474–475, 2001.

[15] P. Glynne-Jones, C. E. M. Démoré, C. Ye, Y. Qiu, S. Cochran, and M. Hill, "Array-controlled ultrasonic manipulation of particles in planar acoustic resonator," *IEEE Trans. Ultrason. Ferroelectr. Freq. Control*, vol. 59, no. 6, pp. 1258–1266, 2012.

[16] Y. Ochiai, T. Hoshi, and J. Rekimoto, "Pixie Dust : Graphics Generated by Levitated and Animated Objects in," *ACM Trans. Graph.*, vol. 33, no. 4, p. Article 85, 2014.

[17] J. Lee, S. Y. Teh, A. Lee, H. H. Kim, C. Lee, and K. K. Shung, "Single beam acoustic trapping," *Appl. Phys. Lett.*, vol. 95, no. 7, 2009.

[18] K. H. Lam *et al.*, "Ultrahigh frequency lensless ultrasonic transducers for acoustic tweezers application," *Biotechnol. Bioeng.*, vol. 110, no. 3, pp. 881–886, 2013.

[19] P. L. Marston, "Radiation force of a helicoidal Bessel beam on a sphere," *J. Acoust. Soc. Am.*, vol. 125, no. 6, pp. 3539–3547, 2009.

[20] D. Baresch, J. L. Thomas, and R. Marchiano, "Spherical vortex beams of high radial degree for enhanced single-beam tweezers," *J. Appl. Phys.*, vol. 113, no. 18, pp. 0–9,

2013.

[21] P. Zhang *et al.*, “Generation of acoustic self-bending and bottle beams by phase engineering,” *Nat. Commun.*, vol. 5, pp. 1–9, 2014.

[22] L. P. Gor’kov, “On the forces acting on a small particle in an acoustical field in an ideal fluid,” *Sov. Phys.*, vol. 6, no. 9, pp. 315–317, 1962.

[23] R. Hickling, “Analysis of Echoes from a Solid Elastic Sphere in Water,” *J. Acoust. Soc. Am.*, vol. 34, no. 10, pp. 1582–1592, 1962.

[24] J. J. Faran, “Sound Scattering by Solid Cylinders and Spheres,” *J. Acoust. Soc. Am.*, vol. 23, no. 4, pp. 405–418, 1951.

[25] M. A. B. Andrade, A. L. Bernassau, J. C. Adamowski, M. A. B. Andrade, A. L. Bernassau, and J. C. Adamowski, “Acoustic levitation of a large solid sphere,” vol. 044101, no. November 2018, pp. 1–5, 2017.

[26] A. Marzo, M. Caleap, and B. W. Drinkwater, “Acoustic Virtual Vortices with Tunable Orbital Angular Momentum for Trapping of Mie Particles,” *Phys. Rev. Lett.*, vol. 120, no. 4, p. 44301, 2018.

[27] C. E. M. Démoré *et al.*, “Acoustic tractor beam,” *Phys. Rev. Lett.*, vol. 112, no. 17, 2014.

[28] C. Chaussy, E. Schmiedt, D. Jocham, W. Brendel, B. Forssmann, and V. Walther, “First Clinical Experience with Extracorporeally Induced Destruction of Kidney Stones by Shock Waves,” *J. Urol.*, vol. 197, no. 2, pp. S160–S163, 2017.

[29] V. G. Bird, B. Fallon, and H. N. Winfield, “Practice Patterns in the Treatment of Large Renal Stones,” *J. Endourol.*, vol. 17, no. 6, pp. 355–363, 2003.

[30] A. D. Maxwell *et al.*, “Fragmentation of Urinary Calculi In Vitro by Burst Wave Lithotripsy,” *J. Urol.*, vol. 193, no. 1, pp. 338–344, 2015.

[31] P. C. May, M. R. Bailey, and J. D. Harper, “Ultrasonic propulsion of kidney stones.,” *Curr. Opin. Urol.*, vol. 26, no. 3, pp. 264–70, 2016.

[32] J. D. Harper *et al.*, “First in Human Clinical Trial of Ultrasonic Propulsion of Kidney Stones,” *J. Urol.*, vol. 195, no. 4, pp. 956–964, 2016.

[33] A. Shah *et al.*, “Novel ultrasound method to reposition kidney stones,” in *Urological Research*, 2010, vol. 38, no. 6, pp. 491–495.

[34] O. A. Sapozhnikov and M. R. Bailey, “Radiation force of an arbitrary acoustic beam on an elastic sphere in a fluid,” *The Journal of the Acoustical Society of America*, vol. 133, no. 2. pp. 661–676, 2013.

[35] Y. Ochiai, T. Hoshi, and J. Rekimoto, “Pixie Dust : Graphics Generated by Levitated and Animated Objects in,” *ACM Trans. Graph.*, vol. 33, no. 4, p. Article 85, 2014.

[36] B. Hefner and P. Marston, “An acoustical helicoidal wave transducer with applications for the alignment of ultrasonic and underwater systems,” *... J. Acoust. Soc. Am.*, vol. 106, no. August 1999, pp. 3313–3316, 1999.

[37] J. Arlt and K. Dholakia, “Generation of high-order Bessel beams by use of an axicon,” *Opt. Commun.*, vol. 177, no. 1, pp. 297–301, 2000.

[38] R. Marchiano and J.-L. Thomas, “Synthesis and analysis of linear and nonlinear acoustical vortices,” *Phys. Rev. E*, vol. 71, no. 6, p. 066616, 2005.

[39] P. L. Marston, “Axial radiation force of a Bessel beam on a sphere and direction reversal of the force,” *J. Acoust. Soc. Am.*, vol. 120, no. 6, pp. 3518–3524, 2006.

[40] F. G. Mitri, “Negative axial radiation force on a fluid and elastic spheres illuminated by a high-order Bessel beam of progressive waves,” *J. Phys. A Math. Theor.*, vol. 42, no. 24, p. 245202, 2009.

[41] L. Zhang and P. L. Marston, “Axial radiation force exerted by general non-diffracting beams,” *J. Acoust. Soc. Am.*, vol. 131, no. 4, pp. EL329-EL335, 2012.

[42] F. C. Ngo, E. S. Ebbini, and C. a. Cain, “An experimental analysis of a sector-vortex phased array prototype,” *Proceedings., IEEE Ultrason. Symp.*, vol. 281, no. 86, pp. 999–1002, 1989.

[43] G. T. Clement and K. Hynynen, “Micro-receiver guided transcranial beam steering,” *IEEE Trans. Ultrason. Ferroelectr. Freq. Control*, vol. 49, no. 4, pp. 447–453, 2002.

[44] H. Wang, E. S. Ebbini, M. O’Donnell, and C. A. Cain, “Phase Aberration Correction and Motion Compensation for Ultrasonic Hyperthermia Phased Arrays: Experimental Results,” *IEEE Trans. Ultrason. Ferroelectr. Freq. Control*, vol. 41, no. 1, pp. 34–43, 1994.

[45] D. R. Daum, M. T. Buchanan, T. Fjield, and K. Hynynen, “Design and evaluation of a feedback based phased array system for ultrasound surgery,” *IEEE Trans. Ultrason. Ferroelectr. Freq. Control*, vol. 45, no. 2, pp. 431–438, 1998.

[46] K. Hynynen and F. A. Jolesz, “Demonstration of potential noninvasive ultrasound brain therapy through an intact skull,” *Ultrasound Med. Biol.*, vol. 24, no. 2, pp. 275–283, 1998.

[47] G. T. Clement, J. Sun, T. Giesecke, and K. Hynynen, “A hemisphere array for non-invasive ultrasound brain therapy and surgery.,” *Phys. Med. Biol.*, vol. 45, no. 12, pp. 3707–19, 2000.

[48] K. Hynynen *et al.*, “500-Element ultrasound phased array system for noninvasive focal surgery of the brain: A preliminary rabbit study with ex vivo human skulls,” *Magn. Reson. Med.*, vol. 52, no. 1, pp. 100–107, 2004.

[49] F. Wu, J. L. Thomas, and M. Fink, “Time reversal of ultrasonic fields. II. Experimental

results.," *IEEE Trans. Ultrason. Ferroelectr. Freq. Control*, vol. 39, no. 5, pp. 567–78, 1992.

[50] M. Fink and C. Prada, "Acoustic time-reversal mirrors," *Inverse Probl.*, vol. 17, no. 1, p. R1, 2001.

[51] J. L. Thomas and M. A. Fink, "Ultrasonic beam focusing through tissue inhomogeneities with a time reversal mirror: application to transskull therapy," *IEEE Trans. Ultrason. Ferroelectr. Freq. Control*, vol. 43, no. 6, pp. 1122–1129, 1996.

[52] M. Pernot, J.-F. Aubry, M. Tanter, J.-L. Thomas, and M. Fink, "High power transcranial beam steering for ultrasonic brain therapy," *Phys. Med. Biol.*, vol. 48, no. 16, pp. 2577–2589, 2003.

[53] E. S. Ebbini and C. A. Cain, "Multiple-Focus Ultrasound Phased-Array Pattern Synthesis: Optimal Driving-Signal Distributions for Hyperthermia," *IEEE Trans. Ultrason. Ferroelectr. Freq. Control*, vol. 36, no. 5, pp. 540–548, 1989.

[54] M. Lu, M. Wan, F. Xu, X. Wang, and X. Chang, "Design and experiment of 256-element ultrasound phased array for noninvasive focused ultrasound surgery," *Ultrasonics*, vol. 44, no. SUPPL., pp. 325–330, 2006.

[55] M. Lu, M. Wan, F. Xu, X. Wang, and H. Zhong, "Focused beam control for ultrasound surgery with spherical-section phased array: Sound field calculation and genetic optimization algorithm," *IEEE Trans. Ultrason. Ferroelectr. Freq. Control*, vol. 52, no. 8, pp. 1270–1290, 2005.

[56] G. T. Clement and K. Hynynen, "Field characterization of therapeutic ultrasound phased arrays through forward and backward planar projection," *J. Acoust. Soc. Am.*, vol. 108, no. 1, pp. 441–446, 2000.

[57] O. A. Sapozhnikov, S. A. Tsysar, V. A. Khokhlova, and W. Kreider, “Acoustic holography as a metrological tool for characterizing medical ultrasound sources and fields,” *J. Acoust. Soc. Am.*, vol. 138, no. 3, pp. 1515–1532, 2015.

[58] V. A. Khokhlova *et al.*, “Design of HIFU Transducers to Generate Specific Nonlinear Ultrasound Fields,” in *Physics Procedia*, 2016, vol. 87, pp. 132–138.

[59] R. T. Hekkenberg, K. Beissner, B. Zeqiri, R. A. Bezemer, and M. Hodnett, “Validated ultrasonic power measurements up to 20 W,” *Ultrasound Med. Biol.*, vol. 27, no. 3, pp. 427–438, 2001.

[60] IEC/TS61949, *Ultrasonics - Field characterization - In situ exposure estimation in finite-amlitude ultrasonic beams*. 2007.

[61] J. D. Maynard, E. G. Williams, and Y. Lee, “Nearfield acoustic holography: I. Theory of generalized holography and the development of NAH,” *J. Acoust. Soc. Am.*, vol. 78, no. 4, pp. 1395–1413, 1985.

[62] P. a Lewin, N. Barrie-Smith, M. Ide, K. Hynynen, and M. Macdonald, “Interlaboratory acoustic power measurement.,” *J. Ultrasound Med.*, vol. 22, no. 2, pp. 207–13, 2003.

[63] B. Zeqiri and M. Hodnett, “Measurements, phantoms, and standardization,” *Proc. Inst. Mech. Eng. Part H J. Eng. Med.*, vol. 224, no. 2, pp. 375–391, 2010.

[64] S. Maruvada, G. R. Harris, B. A. Herman, and R. L. King, “Acoustic power calibration of high-intensity focused ultrasound transducers using a radiation force technique,” *J. Acoust. Soc. Am.*, vol. 121, no. 3, pp. 1434–1439, 2007.

[65] W. Shou *et al.*, “Acoustic power measurement of high intensity focused ultrasound in medicine based on radiation force,” *Ultrasonics*, vol. 44, no. SUPPL., pp. 17–20, 2006.

[66] B. Delannoy, H. Lasota, C. Bruneel, R. Torguet, and E. Bridoux, “The infinite planar

baffles problem in acoustic radiation and its experimental verification," *J. Appl. Phys.*, vol. 50, no. 8, pp. 5189–5195, 1979.

[67] I. Freund, "Critical point explosions in two-dimensional wave fields," *Opt. Commun.*, vol. 159, no. 1, pp. 99–117, 1999.

[68] M. R. Dennis and J. B. Götte, "Instability of higher-order otpical vortices analyzed with multi-pinhole interferometer," *Phys. Rev. Lett.*, vol. 109, no. 18, pp. 1018–1020, 2012.

[69] A. Kumar, P. Vaity, J. Bhatt, and R. P. Singh, "Stability of higher order optical vortices produced by spatial light modulators," *J. Mod. Opt.*, vol. 60, no. 20, pp. 1696–1700, 2013.

[70] IEC/TS62556, *Ultrasonics-field characterization-specification and measurement of field parameters for high intensity therapeutic ultrasound (HITU) transducers and systems*. 2014.

[71] C. R. P. Courtney, B. W. Drinkwater, C. E. M. Demore, S. Cochran, A. Grinenko, and P. D. Wilcox, "Dexterous manipulation of microparticles using Bessel-function acoustic pressure fields," *Appl. Phys. Lett.*, vol. 102, no. 12, 2013.

[72] T. Laurell, F. Petersson, and A. Nilsson, "Chip integrated strategies for acoustic separation and manipulation of cells and particles.," *Chem. Soc. Rev.*, vol. 36, pp. 492–506, 2007.

[73] X. Ding *et al.*, "On-chip manipulation of single microparticles, cells, and organisms using surface acoustic waves," *Proc. Natl. Acad. Sci.*, vol. 109, no. 28, pp. 11105–11109, 2012.

[74] M. J. Shortencarier *et al.*, "A Method for Radiation-Force Localized Drug Delivery Using Gas-Filled Lipospheres," vol. 51, no. 7, pp. 822–831, 2004.

[75] M. A. Ghanem *et al.*, "Field Characterization and Compensation of Vibrational Nonuniformity for a 256-Element Focused Ultrasound Phased Array," *IEEE Trans. Ultrason. Ferroelectr. Freq. Control*, vol. 65, no. 9, pp. 1618–1630, 2018.

[76] O. A. Sapozhnikov and M. R. Bailey, “Radiation force of an arbitrary acoustic beam on an elastic sphere in a fluid,” *J. Acoust. Soc. Am.*, vol. 133, no. 2, pp. 661–676, 2013.

[77] A. Anhäuser, R. Wunenburger, and E. Brasselet, “Acoustic rotational manipulation using orbital angular momentum transfer,” *Phys. Rev. Lett.*, vol. 109, no. 3, pp. 1–5, 2012.

[78] C. E. M. Demore, Z. Yang, A. Volovick, S. Cochran, M. P. MacDonald, and G. C. Spalding, “Mechanical evidence of the orbital angular momentum to energy ratio of vortex beams,” *Phys. Rev. Lett.*, vol. 108, no. 19, pp. 1–5, 2012.

[79] P. Z. Dashti, F. Alhassen, and H. P. Lee, “Observation of Orbital Angular Momentum Transfer between Acoustic and Optical Vortices in Optical Fiber,” vol. 043604, no. February, pp. 1–4, 2006.

[80] G. T. Silva, “Acoustic radiation force and torque on an absorbing compressible particle in an inviscid fluid,” vol. 2405, 2014.

[81] P. L. Marston, “Acoustic beam scattering and excitation of sphere resonance : Bessel beam example,” *J. Acoust. Soc. Am.*, vol. 122, no. 247, 2007.

[82] K. Melde, A. G. Mark, T. Qiu, and P. Fischer, “Holograms for acoustics,” *Nature*, vol. 537, no. 7621, pp. 518–522, 2016.

[83] S. D. Mellin and G. P. Nordin, “Limits of scalar diffraction theory and an iterative angular spectrum algorithm for finite aperture diffractive optical element design,” vol. 8, no. 13, pp. 1058–1065, 2001.

[84] I. V. Basistiy, V. Y. Bazhenov, M. S. Soskin, and M. V. Vasnetsov, “Optics of light beams with screw dislocations,” *Opt. Commun.*, vol. 103, no. 5–6, pp. 422–428, 1993.

[85] J. Lekner, “Acoustic beams with angular momentum Acoustic beams with angular momentum,” vol. 3475, no. 2006, 2009.

[86] L. Zhang and P. L. Marston, “viscous dissipation Acoustic radiation torque on small objects in viscous fluids and connection with viscous dissipation (L),” vol. 2917, 2014.

[87] K. D. Skeldon, C. Wilson, M. Edgar, and J. Padgett, “An acoustic spanner and its associated rotational Doppler shift,” *New J. Phsyics*, vol. 10, 2008.

[88] Z. Hong, J. Zhang, and B. W. Drinkwater, “Observation of Orbital Angular Momentum Transfer from Bessel-Shaped Acoustic Vortices to Diphasic Liquid-Microparticle Mixtures,” vol. 214301, no. May, pp. 1–5, 2015.

[89] C. Shi, M. Dubois, Y. Wang, and X. Zhang, “High-speed acoustic communication by multiplexing orbital angular momentum,” vol. 114, no. 28, pp. 11–14, 2017.

[90] V. Bollen, D. J. Zartman, T. M. Marston, and P. L. Marston, “Proceedings of Meetings on Acoustics,” vol. 070075, no. 2013, 2014.

[91] D. T. Blackstock, *Fundamentals of Physical Acoustics*. John Wiley & Sons Inc., 2004.

[92] F. G. Mitri, “Acoustic radiation force of high-order Bessel beam standing wave tweezers on a rigid sphere,” *Ultrasonics*, vol. 49, no. 8, pp. 794–798, 2009.

[93] Y. Yang, M. Chen, M. Mazilu, A. Mourka, Y. D. Liu, and K. Dholakia, “Effect of the radial and azimuthal mode indices of a partially coherent vortex field upon a spatial correlation singularity,” *New J. Phys.*, vol. 15, 2013.

VITA

The author received a B.S. in civil engineering in 2009, an M.S. degree in aeronautics and astronautics engineering in 2012 from the University of Washington. He received the Engineer in Training Certificate from the State of Washington in 2009. He worked as a structural engineer at SIE, Mukilteo, WA from 2012 to 2014. Most of his work focused on linear and nonlinear finite element analysis. His research involves the development of three-dimensional acoustical traps for the manipulation macroscopic objects and the development of advanced holographic lenses. Other research interests include vibroacoustics, stress wave propagation, optimization techniques and finite-element modeling.